



**Igor Brandão Cavalcanti Moreira**

**Harnessing optomechanical interactions: From  
trapping organisms to entangling nanospheres**

**Dissertação de Mestrado**

Dissertation presented to the Programa de Pós-graduação em Física of PUC-Rio in partial fulfillment of the requirements for the degree of Mestre em Ciências - Física.

Advisor: Prof. Thiago Barbosa dos Santos Guerreiro

Rio de Janeiro  
April 2021



**Igor Brandão Cavalcanti Moreira**

**Harnessing optomechanical interactions: From  
trapping organisms to entangling nanospheres**

Dissertation presented to the Programa de Pós-graduação em Física of PUC-Rio in partial fulfillment of the requirements for the degree of Mestre em Ciências - Física. Approved by the Examination Committee:

**Prof. Thiago Barbosa dos Santos Guerreiro**

Advisor

Departamento de Física – PUC-Rio

**Prof. Welles Antônio Martinez Morgado**

Departamento de Física – PUC-Rio

**Prof. Gabriel Teixeira Landi**

USP

**Prof. Mauro Paternostro**

QUB

Rio de Janeiro, April 13th, 2021

All rights reserved.

### **Igor Brandão Cavalcanti Moreira**

The author graduated in Physics from Pontifícia Universidade Católica do Rio de Janeiro in 2019 with a Complementary Studies diploma in Mathematics.

#### Bibliographic data

Brandão Cavalcanti Moreira, Igor

Harnessing optomechanical interactions: From trapping organisms to entangling nanospheres / Igor Brandão Cavalcanti Moreira; advisor: Thiago Barbosa dos Santos Guerreiro. – 2021.

155 f: il. color. ; 30 cm

Dissertação (mestrado) - Pontifícia Universidade Católica do Rio de Janeiro, Departamento de Física, 2021.

Inclui bibliografia

1. Física - Teses. 2. Optomecânica Quântica. 3. Pinças Ópticas. 4. Interferometria. 5. Emaranhamento. 6. Informação Quântica Gaussiana. I. Barbosa dos Santos Guerreiro, Thiago. II. Pontifícia Universidade Católica do Rio de Janeiro. Departamento de Física. III. Título.

CDD: 530

To my mother, for her endless love and support.  
Her unmatched willpower inspires me each day.

## Acknowledgments

First, I would like to thank Professor Thiago Guerreiro for having introduced me to the field of Quantum Optomechanics, which deeply captivated me over the last two years. When I completed my Bachelor degree I had no idea which line of research I wanted to pursue, but I recalled really enjoying his Quantum Mechanics classes and being fascinated by the nonchalant way at which he tackled and easily solved the problems that I had just spent countless hours on. So it is no surprise that when he started talking about optical levitation, searching for possible unknown forces, entanglement generation, ... I found my Master's subject. Over the past two years, I have renewed my passion for Physics and found a knack for Quantum Optomechanics. I am very thankful for him and the group he founded on PUC-Rio, specially Bruno Melo, Bruno Suassuna and Daniel Tandeitnik without whom this Dissertation would not have been possible.

I also need to thank my Professors from PUC-Rio who have taught me everything I know of Mathematics and Physics, from undergraduate studies up to this point. Specially, I would like to thank Professor Carlos Tomei, for helping me decide years ago if I should stay in Physics or move to the Mathematics Department, and Professor Antonio Zelaquett, from UFF; I am proud to have worked and written articles with both of them. On the administrative side, I am grateful for all the patience and care that Giza and Carla have had for me.

I would also like to make a special thank to my first advisor and great friend Professor Dan Marchesin. We first met about a month before I started my studies at PUC-Rio and a couple of months latter I was already starting my undergraduate research at IMPA's Laboratory of Fluid Dynamics. There I took my first steps into the academic world and learned every ounce of my knowledge of Programming, without which developing the numerical toolbox used throughout this dissertation would not have been possible. Dan taught me a portion of his endless insights on how to optimize a code and advised me on the most difficult moments of my life. I am forever grateful for his support and friendship.

I am privileged for having grown up in such a loving family. I am extremely grateful for the love and support from my grandfather Nilson, my uncle Nilson Jr., my aunt Lucia, my greatest friend Isabella Saraiva and my cousins Amanda, Danilo, Carol and Lucas, which have their names properly displayed this time! They were there for me when my mother passed away and I can not thank them enough.

Finally, I want to thank the person responsible for me being where I am. My mother. She raised me all by herself, putting my needs above her own. She made innumerable compromises to make sure that I had the best available education, everything that I needed and much more in order for me to be the best possible version of what I could be. She was the most loving, caring and determined person I have ever know. When she died was the most difficult day of my life. I lost my mother, my best friend, the person who was always by my side, “ombro a ombro”, no matter what. I hope to live up to her unwavering willpower and make sure that all the sacrifices she made for me were worthwhile.

This work was financed in part by Conselho Nacional de Desenvolvimento Científico e Tecnológico (CNPq) and Fundação de Amparo à Pesquisa do Estado do Rio de Janeiro (FAPERJ). This study was financed in part by the Coordenação de Aperfeiçoamento de Pessoal de Nível Superior - Brasil (CAPES) - Finance Code 001. I would like to thank the support received by CNPq Scholarship No. 131945/2019-0 and FAPERJ Scholarship No. E-26/200.270/2020.

## Abstract

Brandão Cavalcanti Moreira, Igor; Barbosa dos Santos Guerreiro, Thiago (Advisor). **Harnessing optomechanical interactions: From trapping organisms to entangling nanospheres.** Rio de Janeiro, 2021. 155p. Dissertação de Mestrado – Departamento de Física, Pontifícia Universidade Católica do Rio de Janeiro.

Over the last decades, light-matter interactions have proven to be a versatile tool to measure and control mechanical systems, finding application from force sensing to ground state cooling of nanospheres. In this dissertation, we present some of the theoretical tools that describe interferometers, optical tweezers and optical cavities, fundamental constituents of the optomechanical toolbox.

In the classical regime, we study the circulating electromagnetic field within linear interferometers and show how one can find the resulting transmitted field, presenting examples of optical cavities with an arbitrary number of dispersive elements. Moreover, we also study the radiation-pressure forces that optical beams can imprint on dielectric particles and show how 3D optical trapping is possible in both bright and dark focuses. Potential application to trapping of living organisms is studied.

In the quantum regime, we study how the resonant field of optical cavities can dispersively interact with different mechanical systems, giving rise to an entangling closed quantum dynamics. When considering an ultracold cloud of atoms interacting with two optical modes, we show the emergence of optical entanglement which evidences the nonclassical nature of the macroscopic atomic ensemble. The experimental feasibility of this experiment with current technology is studied.

Furthermore, we investigate the scenario where a finely tuned optical tweezer places a trapped particle inside an optical cavity such that the tweezer's scattered photons can survive inside the cavity. This so-called coherent scattering interaction has been shown to cool nanoparticles to phonon numbers lower than one deep into the quantum regime. We show that it also can generate mechanical entanglement between many levitated particles even in a room temperature environment. An overview on continuous variable systems and the custom numerical toolbox used throughout this work are presented.

## Keywords

Quantum Optomechanics; Optical Tweezers; Interferometry; Entanglement; Gaussian Quantum Information.

## Resumo

Brandão Cavalcanti Moreira, Igor; Barbosa dos Santos Guerreiro, Thiago. **Colocando interações optomecânicas em uso: do aprisionamento de organismos ao emaranhamento de nanoesferas**. Rio de Janeiro, 2021. 155p. Dissertação de Mestrado – Departamento de Física, Pontifícia Universidade Católica do Rio de Janeiro.

Nas últimas décadas, interações entre luz e matéria provaram ser uma ferramenta versátil para medir e controlar sistemas mecânicos, encontrando aplicações desde detecção de forças até resfriamento ao estado fundamental de nanoesferas. Nesta dissertação, nós apresentamos algumas das ferramentas teóricas necessárias para descrever interferômetros, pinças ópticas e cavidades ópticas, constituintes fundamentais da caixa de ferramentas optomecânica.

No regime clássico, estudamos o campo eletromagnético circulante em interferômetros lineares e mostramos como encontrar o campo resultante transmitido, apresentando exemplos de cavidades ópticas com um número arbitrário de elementos dispersivos. Nós também estudamos as forças de pressão de radiação que feixes ópticos podem imprimir em partículas dielétricas e mostramos como o aprisionamento óptico 3D é possível em focos claros e escuros. A potencial aplicação para captura de organismos vivos é estudada.

No regime quântico, nós estudamos como o campo ressonante de cavidades ópticas pode interagir de forma dispersiva com diferentes sistemas mecânicos, dando origem a uma dinâmica quântica fechada emaranhante. Ao considerar uma nuvem ultra resfriada de átomos interagindo com dois modos ópticos, mostramos o surgimento de emaranhamento óptico que evidencia a natureza não-clássica do conjunto atômico macroscópico. A viabilidade experimental deste experimento com tecnologia atual é estudada.

Além disso, nós investigamos o cenário em que uma pinça óptica posiciona uma partícula levitada dentro de uma cavidade óptica de forma que os fótons da pinça espalhados pela partícula possam sobreviver dentro da cavidade. Já foi demonstrado que esta interação, chamada de espalhamento coerente, pode resfriar nanopartículas até números de fônons menores do que um, atingindo profundamente o regime quântico. Nós mostramos que esta interação também pode gerar emaranhamento mecânico entre muitas partículas levitadas, mesmo em um ambiente a temperatura de 300 K. Um resumo sobre sistemas de variáveis contínuas e a caixa de ferramentas numérica customizada usada ao longo deste trabalho são apresentados.

## Palavras-chave



Optomecânica Quântica; Pinças Ópticas; Interferometria; Emaranhamento; Informação Quântica Gaussiana.

# Table of contents

<b>1</b>	<b>Introduction</b>	<b>20</b>
<b>2</b>	<b>Interferometry</b>	<b>23</b>
2.1	From an optics schematic to a weighted directed graph	23
2.2	Rules for graph simplification	25
2.3	Optical cavities	29
2.4	Multiple inputs and outputs	33
2.5	Quantum interferometry	35
2.6	Conclusions	36
<b>3</b>	<b>Optical Tweezers</b>	<b>37</b>
3.1	Optical Beams	38
3.2	Optical Forces	42
3.3	Optical Trapping in a Bright Focus	46
3.4	Optical Trapping in a Dark Focus	47
3.5	Conclusions	63
<b>4</b>	<b>Dispersive Optomechanics</b>	<b>66</b>
4.1	Dispersive Hamiltonian	66
4.2	Unitary quantum dynamic	70
4.3	Entanglement dynamics in dispersive optomechanics	72
4.4	Conclusions	85
<b>5</b>	<b>Coherent Scattering</b>	<b>86</b>
5.1	Levitated nanoparticle Hamiltonian	87
5.2	Quantum Langevin equations	94
5.3	Decoherence mechanisms	103
5.4	Coherent Scattering-mediated correlations between levitated nanospheres	103
5.5	Conclusion	113
<b>6</b>	<b>Outlook</b>	<b>115</b>
	<b>Bibliography</b>	<b>119</b>
<b>A</b>	<b>List of publications</b>	<b>143</b>
<b>B</b>	<b>Overview on continuous variable systems</b>	<b>144</b>
B.1	Continuous Variable systems	144
B.2	Gaussian states	145
B.3	Symplectic geometry and informational measures for gaussian states	147
B.4	Entanglement Criterias	150
<b>C</b>	<b>Numerical Toolbox</b>	<b>152</b>

## List of figures

- Figure 2.1 (a) Optical schematics of a Michelson interferometer. Dots and arrows define the position and direction, respectively, of states A, B, C and D. The red lines represent light passing by the interferometer. (b) Directed graph  $G$  corresponding to the Michelson interferometers. Green and the red circles indicate, respectively, the input and the output vertices. 24
- Figure 2.2 Graphs  $G$  and  $\hat{G}$  for two different rules in which multiple edges are replaced by a single edge with equivalent weight equal to (a) the product of the weights of each individual edge, if they are consecutive edges, or (b) the sum of the weights of each individual edge, if they are in parallel. 26
- Figure 2.3 (a) A loop in vertex C, connected only to vertices B and D, is contracted by joining B and D with an equivalent edge. (b) Multiple loops at a vertex C can be replaced by a single loop with weight equal to the sum of the weights of each individual loop. 27
- Figure 2.4 Vertex detaching:  $\hat{G}$  is obtained by creating copies of the vertex D so that walks are conserved; each copy of D has a single incoming and outgoing edge, which allows for the application of previous rules. 28
- Figure 2.5 (a) Optical schematics of a Fabry-Pérot cavity. Since in this example the cavity's reflection is not of interest, only the output state C is defined. (b) Graph  $G$  corresponding to the Fabry-Pérot cavity. The loop in vertex B corresponds to the situation in which the wave-front undergoes one round-trip inside the cavity, going from state B back to state B. 30
- Figure 2.6 Schematics for  $N$  membranes inside a cavity. Since one state is defined before the input mirror and one state is defined after each optical element, there is a total of  $N + 3$  states. 30
- Figure 2.7 Walks arising from the detachment of the state  $A_{N+2}$ : (a) Walk from vertex  $A_{N+1}$  to vertex  $A_k$ , for  $k$  such that  $2 \leq k \leq N+1$ . This walk and the edge  $\alpha_{N+1,k}$  are in parallel. (b) Walk from vertex  $A_{N+1}$  to the output vertex  $A_{N+3}$ . 31
- Figure 2.8 Graph associated to the transmission of a cavity with a membrane in the middle. Applying the simplification described in the present Section to this graph yields the graph associated to a cavity with no membranes inside of it. Conversely, applying the substitutions prescribed in equation (2-10) to the response factor of a Fabry-Perót cavity gives the response factor for the displayed graph. 33

- Figure 2.9 (a) Optical schematics corresponding to a Mach-Zehnder interferometer. Differences between the two paths inside the interferometer are summarized by a phase  $\theta$ . (b) Graph corresponding to the Mach-Zehnder interferometer, with two input states, indicated by the green circles, and two output states, indicated by the red circles. 34
- Figure 2.10 Simplification of the graph corresponding to a Mach-Zehnder interferometer. The graph is simplified until all that remains are the input and output vertices. 34
- Figure 3.1 Intensities for profiles for Laguerre-Gauss beams at their focal plane,  $z = 0$ . For this simulation, we used:  $n_m = 1.33$ ,  $NA = 0.5$ ,  $\lambda = 780$  nm,  $P_0 = 50$  mW. 39
- Figure 3.2 Intensity in the (a) radial and (b) axial directions for bottle beams with  $p = 1$  and  $p = 2$ . Intensity landscape in the  $xz$  plane for bottle beams with (c)  $p = 1$  and (d)  $p = 2$ . Due to the normalization of  $x$ ,  $z$  and  $I$ , these plots depend only on  $p$ , and are independent from the remaining beam parameters. 41
- Figure 3.3 Forces generated by a Gaussian optical trap: (a) in the radial direction  $x$ ; (b) in the longitudinal direction  $z$ . 46
- Figure 3.4 Forces acting on a trapped sphere in the (a)  $x$  direction and (b)  $z$  direction for  $p = 1$  and  $p = 2$ . Solid lines are gradient forces, while dashed lines are scattering forces. Potential landscape in the  $xz$  plane for a sphere trapped by a bottle beam with (c)  $p = 1$  and (d)  $p = 2$ . The parameters used for these plots are:  $NA = 0.5$ ,  $R = 70$  nm,  $\lambda_0 = 780$  nm,  $n_m = 1.46$ ,  $n_p = 1.33$ ,  $P_0 = 200$  mW,  $T = 300$  K. 49
- Figure 3.5 Comparison between the values of  $\sqrt[4]{\langle \rho^4 \rangle}$  in (a),(c) and of  $\sqrt{\langle z^2 \rangle}$  in (b),(d) obtained from the approximated potential in Eq.(3-37) and from simulation of the particle's motion subject to the exact potential in Eq.(3-24) for different laser powers. The motion was simulated during 10s with time steps of  $0.5\mu\text{s}$  using  $NA = 0.5$ ,  $R = 70$  nm,  $\lambda_0 = 780$  nm,  $n_m = 1.46$ ,  $n_p = 1.33$ ,  $T = 295$  K,  $p = 1$ . 51
- Figure 3.6 Ratios  $r_1 = \langle T_{\rho^2 z^2} \rangle / \langle T_{\rho^4} \rangle$  and  $r_2 = \langle T_{\rho^2 z^2} \rangle / \langle T_{z^2} \rangle$  obtained by simulating the motion of a particle subject to the exact potential in Eq.(3-24) for different laser powers. The motion was simulated during 10s with time steps of  $0.5\mu\text{s}$  using  $NA=0.5$ ,  $R = 70\text{nm}$ ,  $\lambda_0 = 780\text{nm}$ ,  $n_m = 1.46$ ,  $n_p = 1.33$ ,  $T = 295\text{K}$ . 53
- Figure 3.7 Positions of the particle obtained by simulating the motion of a particle trapped by the exact potential in Eq.(3-24) for (a)  $P_0 = 100$  mW and (b)  $P_0 = 5$  W. The motion was simulated during 10s with time steps of  $0.5\mu\text{s}$  using  $NA = 0.5$ ,  $R = 70$  nm,  $\lambda_0 = 780$  nm,  $n_m = 1.46$ ,  $n_p = 1.33$ ,  $T = 295$  K,  $p = 1$ . To allow better visualization, the  $20 \times 10^6$  positions generated by the simulation were divided in 1000 sets, and only the first value of each set is displayed in the figure. 53

Figure 3.8 Optical forces acting on a particle trapped by a bottle beam in the intermediate regime ( $R \approx \lambda$ ). The force in the axial direction ( $F_z(z)$ ) is calculated for  $x = y = 0$ , while the force in the radial direction ( $F_x(x)$ ) is calculated for  $y = 0$  and  $z = z_{eq}$ . If no axial equilibrium position is found,  $F_x(x)$  is evaluated at  $z = 0$ . The particle's radius is constant within each column, while the numerical aperture is constant within each line. The forces are normalized by the particle's mass, other parameters used in simulation are:  $n_p = 1.33$ ,  $n_m = 1.46$ ,  $\lambda_0 = 780$  nm,  $P = 500$  mW, density of the particle =  $10^3$  kg/m<sup>3</sup>,  $p = 1$ . 59

Figure 3.9 Intermediate regime simulations for different values of NA and  $R$ : (a) Axial equilibrium coordinate and (b) first derivative of the force in the radial direction. Medium gray: no equilibrium position was found in the inspected range ( $-6\lambda_0 < z < 6\lambda_0$ ). Light (dark) gray: an equilibrium position was found outside the bottle, at  $z_{eq} < -H/2$  ( $z_{eq} > H/2$ ) and the force is non-restorative (restorative) along the radial direction. The regions in different colors are the ones in which trapping inside the bottle is possible. The parameters used in the simulation were  $\lambda_0 = 780$  nm,  $P = 500$  mW,  $n_m = 1.46$ ,  $n_p = 1.33$ ,  $p = 1$ . 60

Figure 3.10 Intermediate regime simulations for different values  $n_m$ : (a) Axial equilibrium coordinate and (b) first derivative of the force in the radial direction as a function of particle's radius. Points for which  $z_{eq} > H/2$  are not displayed. The parameters used in the simulation were  $\lambda_0 = 780$  nm,  $P = 500$  mW,  $n_m = 1.46$ ,  $n_p = 1.33$ ,  $p = 1$ . 61

Figure 3.11 Forces acting on a trapped Mycoplasma cell, shown here centered at the origin for size comparison, (a) along the  $x$  direction as a function of radial displacement and (b) along the  $z$  direction as a function of axial displacement. The solid and the dashed curves correspond to a medium's refractive index of 1.36 and 1.39, respectively, while the yellow area correspond to  $1.36 \leq n_m \leq 1.39$ . The other parameters used in the simulation are displayed in Table 3.1. 63

Figure 4.1 Schematic representation of an optical cavity with a movable extremity following harmonic motion. 67

Figure 4.2 A nanoparticle, trapped by an optical tweezer, is placed along the axis of a cavity populated by a single optical mode of frequency  $\omega_a$ . If the position  $x_0$  of the center of the optical trap is properly chosen, the coupling between particle and light becomes linear on the particle's displacement. 69

- Figure 4.3 (a) Schematics of coupled optical cavities sharing a “mirror-in-the-middle” under a harmonic potential. No photon transfer from one cavity to the other is allowed. (b) Schematics of a particle trapped by an optical tweezer coupled to two modes of a cavity. The particle can be considered as a Silica nanosphere or a cloud of ultracold atoms. When the levitated object is properly positioned, the Hamiltonian describing both systems acquires the same form. 73
- Figure 4.4 Concurrence (blue) and von Neumann entropy (yellow) for  $\rho_{AB}(t)$  as a function of time. For this plot  $k = 0.5$ . 78
- Figure 4.5 Time-dependent EPR variances  $D_{ij}(t)$  (yellow) for the various bipartitions of the system, with its envelope (blue) and threshold for the Duan Criteria (black dashed line). We use  $\omega_a = \omega_b \simeq 2\pi \cdot 1.59 \times 10^{14}$  Hz and the remaining parameters as in Table 4.3. 80
- Figure 4.6 (a) Minimum value of  $D_{AB}(t)$  within the photon lifetime inside the cavity,  $\tau = \kappa^{-1} \sim 15.6\mu s$ , as a function of (a) dimensionless coupling  $k$  and mechanical oscillator’s temperature  $T$ , and (b) coherent state amplitudes of  $\alpha$  and  $\beta$ . The optimal coherent amplitudes that globally minimizes the Duan criteria are found to be  $\alpha \sim \beta \sim 0.91$ . We use  $\omega_a = \omega_b \simeq 2\pi \cdot 1.59 \times 10^{14}$  Hz and every other parameter as in in Table 4.3. 82
- Figure 5.1 Schematics of N optically levitated nanoparticles, each by its own optical tweezer inside the same optical cavity. Every tweezer has the same frequency which is tuned with the cavity resonance frequency such that the scattered photons can survive inside the cavity. It is assumed that the tweezers are sufficiently spaced such that any overlap between them are negligible. A single external laser serves as the light source for the experiment which passes through a beam splitter (BS) that allows for part of it to tweezer a nanoparticle and part of it to follow to an amplifier and go on to the next BS. Information about the system is retrieved through the leaking field from the rightmost end mirror of the cavity. 88
- Figure 5.2 Fabry-Pérot cavity with an imperfect rightmost end mirror. 94
- Figure 5.3 Schematics of an optical cavity being actively driven by an external laser. 97
- Figure 5.4 Levitated nanoparticle and the surrounding gas imprinting random kicks and damping on its motion. 99

- Figure 5.5 Simulation with  $N = 2$  identical levitated NPs initially in the vacuum state following a closed unitary dynamics. Time evolution of logarithmic negativity (blue) and von Neumann entropy (red) for each bipartition of the system. In this simulation, we considered  $\Delta = 10 \times \omega_j$ , ensuring the formal limit  $\omega_j \ll \Delta$  while  $\kappa = 0$  and  $\gamma_j = 0 \forall j$ , making the system closed. Due to instabilities in the numerical simulation of the von Neumann entropy in the mechanical bipartition, we show both the calculated values (dark red points) and smoothed trace (light red line). 107
- Figure 5.6 Time evolving LN between a pair of particles for an increasing number of particles sharing the same cavity. Every NP is considered to be in the ground state and in contact with a cryogenic environment at temperature  $T_{\text{env},j} = 130$  K, resulting in  $\gamma_j = 0.957$  mHz. 108
- Figure 5.7 Simulation with  $N = 2$  identical levitated NPs with initial temperature  $T_j = 4.6 \mu\text{K}$  in contact with a cryogenic environment at  $T_{\text{env},j} = 130$  K,  $\gamma_j = 0.957$  mHz. (a) Time evolution of logarithmic negativity (blue) and von Neumann entropy (red) for each bipartition of the system. (b) Mutual information for the total system (yellow) and subsystem with only the levitated NPs (blue) evolving in time. 109
- Figure 5.8 Maximum of the logarithmic negativity within the system's coherence time for two particles as a function of their initial temperatures. Notice that we need highly cooled particles to generate mechanical entanglement. 110
- Figure 5.9 Time evolving logarithmic negativity for different coupling strengths,  $g_j = g$  for all  $j$ . Here we considered every NP starting in a thermal state at  $T_j \sim 4.6 \mu\text{K}$  (occupation number  $\bar{n}_{0,j} = 0.0430$ ). Observe that in the high coupling regime,  $g \sim \omega$ , entanglement birth, death and revivals are present. 111
- Figure 5.10 Time evolution of Wigner function for  $N = 2$  identical levitated NPs. As the particles are identical, they possess identical functions. Black dashed lines indicate the Wigner function semi-axes. Solid black lines denote contours at half of its maximum initial value. As the particles are initially in a thermal state the squeezing degree starts at  $\eta(0) = 1$  and becomes increasingly smaller as time progresses. The squeezing degree for each time stamp is respectively  $\eta = (1, 0.840, 0.609, 0.454, 0.440)$ ; see Appendix B. 111

Figure 6.1 (a) Two optical cavities are placed orthogonal to each other, each possessing one fixed and one movable end-mirror. The fixed ones are connected in such way that they do not move in respect to one another. In this configuration, when a gravitational wave passes through this setup, one cavity would contract whilst the other one expands, generating an interaction between the gravitational field and the cavities' field [232, 233] analogous to the one studied in Section 4.3. Image courtesy of Prof. Thiago Guerreiro, private communication.

117



## List of tables

Table 3.1	Proposed values for trapping a Mycoplasma cell using a bottle beam.	62
Table 4.1	Values reported in [162].	83
Table 4.2	Optimal parameters for different cavity mirror's radii.	84
Table 4.3	Proposed values for the experimental implementation with ultracold atoms.	84
Table 5.1	Experimental parameters reported in Ref. [15]	112
Table 5.2	Parameter values used in this Chapter	112

## List of Abbreviations

BS – beam splitter

LG – Laguerre-Gauss

VSWF – vector spherical wave-function

SLM – Spatial Light Modulator

RHS – right hand side

EPR – Einstein-Podolski-Rosen

NP – nanoparticle

OT – Optical Tweezer

EM – electromagnetic

RWA – rotating-wave approximation

CS – Coherent Scattering

QLE – Quantum Langevin Equation

CM – covariance matrix

LN – Logarithmic Negativity

CV – Continuous Variable

*The most important step a man can take.  
It's not the first one, is it?  
It's the next one. Always the next step.*

**Brandon Sanderson, *Oathbringer*.**

# 1

## Introduction

In 1900, Max Planck postulated that electromagnetic radiation could only be emitted or absorbed in discrete packets of energy. These discrete quanta, called photons, result in a finite blackbody spectrum, solving the so-called ultraviolet catastrophe that haunted 19th century classical mechanics and electromagnetism. Although at the time Planck regarded the quanta assumption as a mere mathematical device, it set out to be one of the cornerstones of the first quantum revolution that followed, sparking profound changes in our understanding of nature and the laws that govern it.

More than one hundred years after Planck's seminal work, we are entering a new revolution. At this point in time, quantum theory is mature and has already been formulated, put to test and survived every experimental scrutiny it has been subject to so far [1]. Our understanding of this theory has advanced to the point that we can use it to engineer new quantum-enabled technologies. The most prominent example of such technology is perhaps given by the quantum computer. These devices hold the promise of efficiently simulating complex quantum systems and solving mathematical problems intractable using their classical counterparts [2–4]. Beyond quantum computation, the range of applications for these new technologies is far-reaching. Interesting possibilities are quantum sensing [5–10], quantum cryptography [11] and the quantum internet [12].

The field of quantum optomechanics presents itself as a resourceful platform for quantum science and technology. This field studies the interaction between light and mesoscopic mechanical quantum systems, relying on the fact that light carries momentum and, thus, can exert radiation-pressure force on mechanical objects upon momentum transfer. Typically, the momentum transfer from a single photon is imperceptible when compared to the everyday-life scale. However, when considering highly focused optical beams and/or particles with masses on the orders of femtogram to nanogram, optomechanical interactions can influence the mechanical motion.

One possibility to concentrate a high amount of photons, in order to enhance light-matter couplings, are optical cavities. In this work, we will mainly deal with Fabry-Pérot cavities, devices made of parallel high-reflective

mirrors capable of storing resonant electromagnetic fields for long periods of time compared to the resonant frequency. In Chapter 2, we will study how to mathematically describe the circulating optical field within homodyne linear interferometers, giving special attention to optical cavities containing multiple dispersive elements.

We can also amplify light-matter interaction by employing tightly focused laser beams, which can concentrate a high laser power in micron-sized regions. In 1986, Arthur Ashkin first showed that such beams can exert forces upon dielectric particles [13]. If the particle's refractive index is larger/smaller than that of its surroundings, the laser pulls from/repels to regions of higher intensity of light. These optical tweezers allow one to hold and control translational [14–16] and rotational [17–19] degrees-of-freedom of nanometer to micronmeter-sized objects. These optical traps also allow exceptional environmental isolation [1, 14, 20, 21], as the trapped particle is not clamped to external mechanical environments that can introduce unwanted vibrations [22]. Thus, albeit these optical beams can be described classically, they can serve as building blocks for quantum sensing [10] and quantum control [16]. The theory behind optical tweezers and its application in optical trapping are studied in Chapter 3.

When considering quantum cavity optomechanical experiments, the resonating electromagnetic field inside an optical cavity can dispersively interact with nano- and micromechanical degrees-of-freedom. The presence of the mechanical object induces a shift on the cavity resonance frequency dependent on the object's position [23] and, thus, couples light and matter. This interaction has been shown to give rise to squeezing in both optical [24–26] and mechanical [27–29] modes; entanglement in optical [30], mechanical [31] and opto-mechanical [32, 33] bipartitions; and multipartite macroscopic entanglement [34]. We observe that nonclassical correlations and squeezing pose fundamental resources to quantum technologies, from precision force measurements [10, 35, 36] to quantum networks [31, 37]. Moreover, a plethora of cavity-based cooling mechanisms have been theoretically proposed [38–41] and experimentally implemented to cool the motion of mirrors [42, 43], membranes [44, 45], levitated particles [46], and silicon microchips [47]. The dispersive optomechanical interaction and the entanglement dynamics it entails will be studied in Chapter 4.

Coherent scattering of photons from a trapping tweezer into an optical cavity is a novel mechanism for creating strong optomechanical coupling [48], mechanical squeezing [49] and entanglement [50–52]. However, the most prominent feature that first sparked interest on this form of interaction [53]

is the ability to cool the levitated particle. By red detuning the tweezer's frequency relative to the cavity, the trapped particle scatters photons into the cavity that carries away some of its energy. This setup was first proposed theoretically in 2001 [53] and has already been demonstrated experimentally to give rise to 3D cooling [54–56] and achieve motional ground state cooling along one direction [15]. Moreover, simultaneous 2D cooling to lower than one phonon occupancy has been theorized [57]. In Chapter 5, we will study the mechanism behind this coherent scattering interaction, the open quantum dynamics the levitated particle follows and the generation of mechanical entanglement in setups with many levitated nanospheres.

This dissertation is concluded in Chapter 6, with a brief overview of the theory studied in the previous Chapters and a discussion on possible future research directions. The list of publications carried out throughout this Masters, a review on Gaussian Quantum Information, and a description of the developed numerical toolbox can be found in the Appendices.

## 2 Interferometry

In this chapter, we present the theoretical framework developed in our work [58] to calculate the transmission coefficient of linear homodyne interferometric devices through a graphical method closely related to the one proposed in [59], aimed at analysing complex optical interferometers.

Calculating the transmission and reflection coefficients as well as the electric field of interferometric devices may not be a straightforward task, usually involving long matrix computations which obscure physical intuition. As an alternative, these calculations can be performed by associating a weighted directed graph to an optical setup. All possible optical paths leading to a desired position in the interferometer are represented as walks in the graph and must be taken into account, much in the spirit of the Feynman integral. We present simplification rules by which the graph associated to the interferometer can be reduced, and the resulting weighted directed graph contains the information on any transmission and reflection coefficients one wishes to obtain for the given interferometer. Similar ideas can be used both for classical and quantum fields.

This Chapter is divided as follows. In Section 2.1, it is shown, with the aid of examples, how to construct a weighted directed graph from a linear optical setup. It is then defined, in Section 2.2, the general simplification rules to transform a graph, which makes the graphical-based method suitable for a wide range of applications. To demonstrate the power of the defined rules, a number of examples on how to calculate the transmitted field through optical cavities with multiple dispersive elements [60, 61] are provided in Section 2.3. The extension of the method to setups containing multiple inputs and outputs is presented in Section 2.4. Section 2.5 deals with the application of the method to arbitrary quantum states of the electromagnetic field. The Chapter is concluded in Section 2.6 with final considerations.

### 2.1 From an optics schematic to a weighted directed graph

We describe, with the aid of an example, how to obtain a weighted directed graph from a standard optical schematics. Consider the Michelson

interferometer in Figure 2.1(a).

Each arrow, labeled by a capital letter, represents a *state*, defined by a position and a direction in space. A state can be defined at any boundary of an optical element. For instance, state B in Figure 2.1(a) represents a plane wave-front at position B moving to the right.

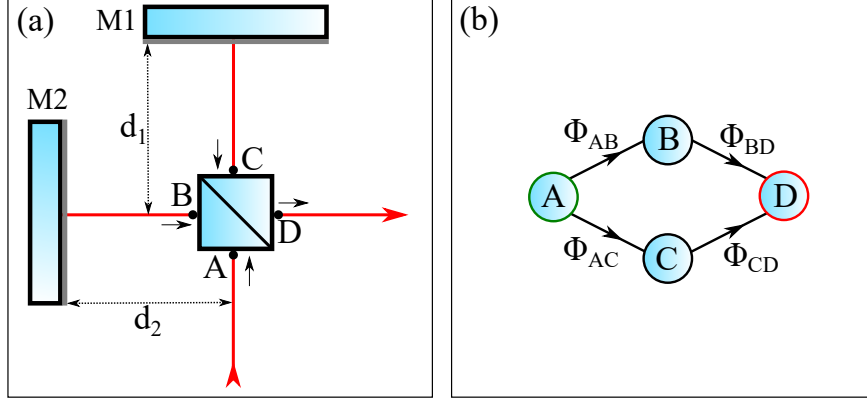


Figure 2.1: (a) Optical schematics of a Michelson interferometer. Dots and arrows define the position and direction, respectively, of states A, B, C and D. The red lines represent light passing by the interferometer. (b) Directed graph  $G$  corresponding to the Michelson interferometers. Green and the red circles indicate, respectively, the input and the output vertices.

Each state is represented by a vertex in a directed graph, as seen in Figure 2.1(b). States should be defined such that: (i) every optical path leading from the input to the output can be represented by a sequence of states and (ii) different optical paths are represented by different sequences of states.

An edge  $\alpha_{ij}$  joins vertex  $i$  to vertex  $j$  if, and only if, the wave-front can go from state  $i$  to state  $j$  without passing by any other state along the way. To each edge  $\alpha_{ij}$  a weight  $\Phi_{ij}$  - the transition amplitude from state  $i$  to state  $j$  - is assigned.

In Figure 2.1(a), for a wave-front with wave number  $k$  in state A, two things can happen. First, it might get transmitted by the beam splitter (BS), with transmittance  $t$  (and reflectance  $r$ ), and then reflected back by the perfect mirror M1, ending up in state C. The transition amplitude for this process is the weight  $\Phi_{AC} = ite^{2ikd_1}$ , and an edge connects the vertices A and C in the graph of Figure 2.1(b). Second, the wave-front might be reflected by the BS and the perfect mirror M2, resulting in state B; the edge connecting A and B has weight  $\Phi_{AB} = re^{2ikd_2}$ .

Light in state C can also be reflected by the BS, resulting in a state D with transition amplitude  $\Phi_{CD} = r$ . Similarly, light in B can be transmitted to D, with associated amplitude  $\Phi_{BD} = it$ .



Since only the amplitude of the field in state D is of interest, there is no need to define a counter propagating state at A. The resulting graph is shown in Figure 2.1(b).

Each optical path from the input to the output of the interferometer corresponds in Figure 2.1(b) to a walk from the source vertex, marked with a green outline, to the sink vertex, marked with a red outline. The *weight* of the walk, which is the product  $\Gamma_\alpha$  of the weights of all the edges along it, relates input and output electric fields  $\mathbf{E}_{\text{in}}$  and  $\mathbf{E}_{\text{out},\alpha}$  after the wave has traveled through the path

$$\mathbf{E}_{\text{out},\alpha} = \Gamma_\alpha \mathbf{E}_{\text{in}}. \quad (2-1)$$

The resultant electric field at the output is then given by

$$\mathbf{E}_{\text{out}} = \Gamma \mathbf{E}_{\text{in}}, \quad (2-2)$$

where the response factor  $\Gamma$  is the sum of the weights  $\Gamma_\alpha$  of all walks from A to D.

In the example of Figure 2.1(b), there are only two possible walks:  $\alpha_{AB}, \alpha_{BD}$  and  $\alpha_{AC}, \alpha_{CD}$ , of respective weights  $\Phi_{AB}\Phi_{BD}$  and  $\Phi_{AC}\Phi_{CD}$ . The response factor is

$$\Gamma = \Phi_{AB}\Phi_{BD} + \Phi_{AC}\Phi_{CD}, \quad (2-3)$$

yielding the known result for the electric field at the output of a Michelson interferometer

$$\mathbf{E}_{\text{out}} = i\tau t(e^{2ikd_1} + e^{2ikd_2}) \mathbf{E}_{\text{in}}. \quad (2-4)$$

Throughout this chapter the convention in [44,62] for the phase gained by reflected and transmitted waves is used. Moreover, only the case of monochromatic electric field with wave number  $k$  is considered.

## 2.2

### Rules for graph simplification

The task of summing the weights of all walks in progressively more complex interferometers can easily become too convoluted. In order to apply the graphical method to a wider range of interferometers, some local simplification rules are now presented. As for electrical circuits, elements in series and/or in parallel are amenable to equivalent substitutions. This is the content of the first two rules. Two graphs  $G$  and  $\hat{G}$  are *equivalent* if they have the same factor  $\Gamma$  relating input and output,  $\mathbf{E}_{\text{out}} = \Gamma \mathbf{E}_{\text{in}}$ .

### Consecutive edges

Suppose a vertex  $P_2$  is connected only to two other vertices: vertex  $P_1$ , by an incoming edge  $\alpha_{1,2}$ , and vertex  $P_3$ , by an outgoing edge  $\alpha_{2,3}$ . A walk from  $P_1$  to  $P_3$  passing by  $P_2$  must contain  $\alpha_{1,2}$  and  $\alpha_{2,3}$ , which contribute with a factor  $\Phi_{1,2}\Phi_{2,3}$  to the weight of the walk. An equivalent graph  $\hat{G}$  is obtained by removing the vertex  $P_2$  and joining  $P_1$  and  $P_3$  by an edge  $\alpha_{1,3}$  of weight  $\Phi_{1,2}\Phi_{2,3}$ . Similarly, for an arbitrary number of consecutive edges as shown in Figure 2.2(a), consecutive edges may be replaced by a single edge of weight given by the product of the weights of the individual edges.

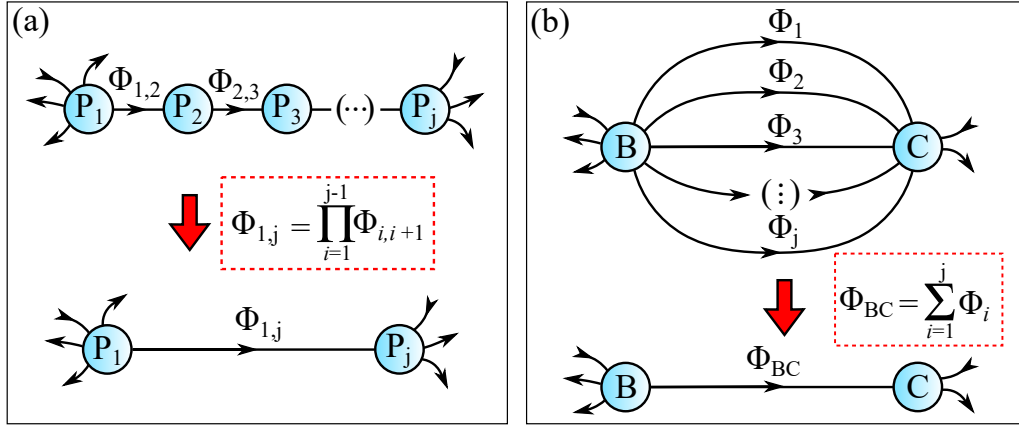


Figure 2.2: Graphs  $G$  and  $\hat{G}$  for two different rules in which multiple edges are replaced by a single edge with equivalent weight equal to (a) the product of the weights of each individual edge, if they are consecutive edges, or (b) the sum of the weights of each individual edge, if they are in parallel.

### Parallel edges

Consider now a graph  $G$  with two vertices  $B$  and  $C$  joined by  $j$  different edges  $\alpha_i$ , with common orientation, and respective weights  $\Phi_i$ , as in Figure 2.2(b). Take  $\hat{G}$  to be the graph obtained from  $G$  replacing these edges by a single one,  $\alpha_{BC}$ , of weight  $\sum_i \Phi_i$ . We show that  $G$  and  $\hat{G}$  are equivalent.

Each walk in  $G$  gives rise to a monomial given by the product of its edge weights. Each walk in  $\hat{G}$ , instead, gives rise to a number of such monomials. It turns out that there is a simple bijection between equal monomials related to both graphs. Indeed, suppose that in  $G$  the walk goes from  $B$  to  $C$   $k$  times, with a contribution  $\Phi_{i_1}\Phi_{i_1}\dots\Phi_{i_k}$  to the overall weight of the walk. Such walk in  $G$  corresponds to a walk in  $\hat{G}$  where edge  $\alpha_{BC}$  is traversed  $k$  times, contributing with  $(\sum_i \Phi_i)^k$  to the weight of the walk. The monomial  $\Phi_{i_1}\Phi_{i_2}\dots\Phi_{i_k}$  is naturally associated with the monomial in  $(\sum_i \Phi_i)^k$  obtained

by collecting  $\Phi_{i_1}$  in the first term  $\sum_i \Phi_{i_1}$ ,  $\Phi_{i_2}$  in the second term,  $\dots$ ,  $\Phi_{i_k}$  in the  $k$ -th term.

Edges between B and C are not required to have the same orientation. Collect edges with different orientations in two sets, and each set is replaced by a single edge as above.

### Loop contraction

Let a vertex C, that contains a loop, be connected to only two other vertices B and D, as in Figure 2.3(a). Every walk from B to D starts with the edge  $\alpha_{BC}$ , continues with a number  $n$ ,  $n = 0, 1, \dots, \infty$ , of loops  $\alpha_{CC}$  and ends with the edge  $\alpha_{CD}$ . Adding up, since  $|\Phi_{CC}| < 1$ , we have the weight from B to D is given by

$$\Phi_{BD} = \Phi_{BC} \left( \sum_{n=0}^{\infty} \Phi_{CC}^n \right) \Phi_{CD} = \frac{\Phi_{BC} \Phi_{CD}}{1 - \Phi_{CC}}. \quad (2-5)$$

Therefore, the simplification rule in this case is: the vertex C and its adjacent edges are eliminated and a single edge  $\alpha_{BD}$  is left with weight  $\Phi_{BC} \Phi_{CD} / (1 - \Phi_{CC})$ , provided that  $|\Phi_{CC}| < 1$ .

Take now a graph with  $j$  loops at C with weights  $\Phi_1, \dots, \Phi_j$ , as in Figure 2.3(b). As in the simplification of parallel edges, an equivalent graph  $\hat{G}$  is obtained by removing all but one loop, for which we assign weight  $\sum_i \Phi_i$ .

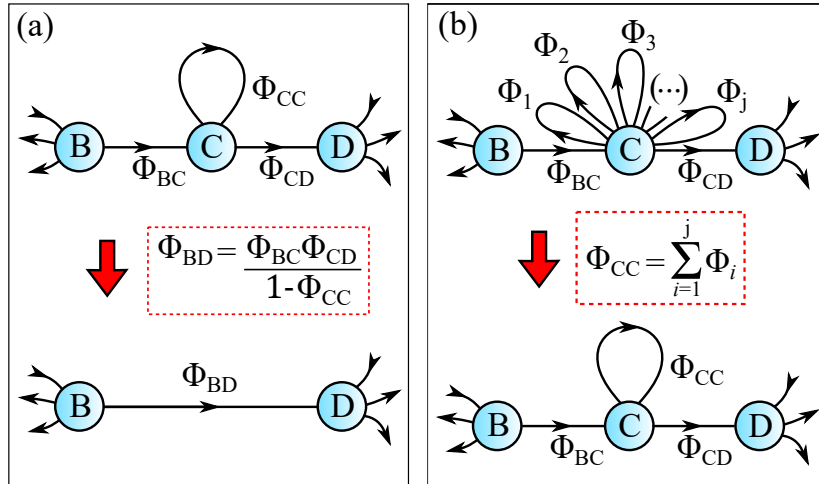


Figure 2.3: (a) A loop in vertex C, connected only to vertices B and D, is contracted by joining B and D with an equivalent edge. (b) Multiple loops at a vertex C can be replaced by a single loop with weight equal to the sum of the weights of each individual loop.

### Vertex detaching

As a final rule, consider a graph  $G$  where a vertex  $D$  has  $i$  incoming edges,  $o$  outgoing edges and  $\ell$  loops attached to it. From the simplification rule for loops,  $\ell = 1$  without loss of generality; also,  $i, o \neq 0$ . In Figure 2.4,  $i = 2$ ,  $o = 2$ ,  $\ell = 1$ . The equivalent graph  $\hat{G}$  is obtained by replacing  $D$  by  $i \cdot o$  vertices  $D_{m,n}$ ,  $m = 1, \dots, i$ ,  $n = 1, \dots, o$  with single incoming and outgoing edges (and the  $\ell$  loops) such that the  $i \cdot o$  pairs (incoming edge, outgoing edge) through  $D$  are reproduced in the  $i \cdot o$  copies  $D_{m,n}$ .

To show the equivalence of  $G$  and  $\hat{G}$ , we again present a bijection between the sets of walks  $\{w\}$  in  $G$  and  $\{\hat{w}\}$  in  $\hat{G}$  which preserves the weight of each walk. Given  $w$  in  $G$ , the corresponding  $\hat{w}$  is constructed by performing an alteration in  $w$  whenever it passes through  $D$ . Each pass belongs to a short stretch  $I_m D O_n$  for unique vertices  $I_m$ , from which the  $m^{\text{th}}$  edge comes, and  $O_n$ , to which the  $n^{\text{th}}$  edge goes. The pass contributes to the weight of  $w$  with  $\Phi_{I_m D} \Phi_{D O_n}$ . To obtain  $\hat{w}$ , replace the stretch  $I_m D O_n$  by a stretch  $I_m D_{m,n} O_n$  joining the vertices of  $\hat{G}$  and preserve loops, if any. Clearly, the construction yields the desired bijection.

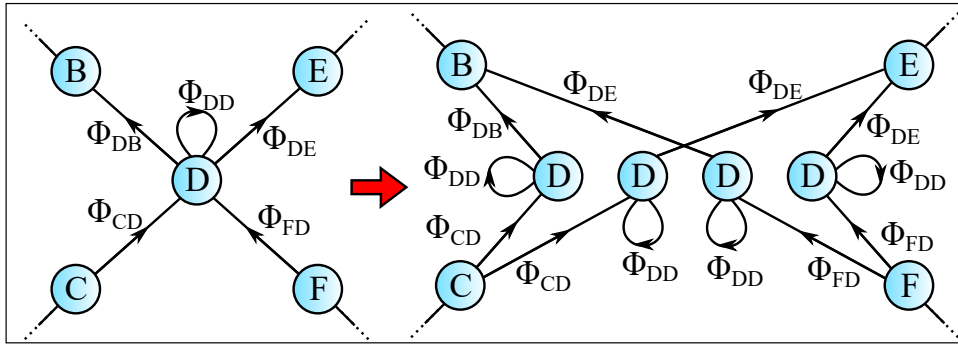


Figure 2.4: Vertex detaching:  $\hat{G}$  is obtained by creating copies of the vertex  $D$  so that walks are conserved; each copy of  $D$  has a single incoming and outgoing edge, which allows for the application of previous rules.

As a final remark, notice that all simplification rules are *local*: they are performed in a very limited region of the graph, and absolutely do not depend on the graph outside of this region. Thus for example, vertex detaching is circumscribed to one vertex ( $D$ , in the example above) and the edges which contain it. The reader will have no difficulty in identifying the appropriate region of each simplification rule.

## 2.3

### Optical cavities

An optical cavity is an arrangement of mirrors that can confine resonating light. At this moment, consider its simplest form, the Fabry-Pérot cavity, consisting of two highly reflecting flat parallel mirrors separated by a distance  $L$ . These set the boundary conditions on the EM fields inside it, allowing only a discrete set of resonance frequencies  $\omega_{\text{cav},n} = n\pi(c/L)$ , where  $c$  is the speed of light and  $n \in \mathbb{N}$ .

Optical cavities are frequently used to increase the circulating power in a interferometer [63, 64], enhance sensitivity in displacement measurements [65–67], cool the center of mass of mechanical oscillators [15, 46, 55, 56] and generate nonclassicality in optomechanical systems [24, 68]. Here we present a brief introduction on this topic and, in Sections 4 and 5, we describe how a cavity field can interact with mechanical objects quantum mechanically. We also refer the reader to [69, 70] for a more in depth classical description of Fabry-Pérot cavities.

In this work, apart from the resonance frequency, there are three main quantities of interest to us when theoretically modelling an optical cavity. The separation between two consecutive resonating frequencies is called *free spectral range* denoted by  $v_{\text{FSR}} = \pi c/L$ , which we assume to be large enough such that we can study only a single optical cavity mode at a time. The *cavity linewidth*  $\kappa$  arising from imperfections in the cavity end mirrors, sometimes also defined as *full width at half maximum* of the resonance peak, is the photon cavity decay rate dictating the photon lifetime within the cavity  $\tau = \kappa^{-1}$ . Finally, the cavity Finesse  $\mathcal{F} = v_{\text{FSR}}/\kappa$  only depends on the cavity losses [69] and gives us the the average number of round-trips a photon performs before leaving the cavity [23].

Since cavities give rise to an infinite number of possible optical paths, summing the amplitude of the waves undergoing each possible path might become a challenging task. To show how the graph-based method can handle this type of calculation, different systems containing optical cavities are studied.

### Fabry-Pérot Cavity

Consider, as a second example, the Fabry-Pérot interferometer in Figure 2.5(a) with states A, B and C. The equivalent graph is shown in Figure 2.5(b), in which  $\Phi_{AB} = it$ ,  $\Phi_{BB} = r^2 e^{2ikd}$ ,  $\Phi_{BC} = ite^{ikd}$ . The edge  $\alpha_{BB}$  corresponds to a round trip inside the cavity: the wave-front travels from the first to the

second mirror, gets reflected by it and then travels back to the first mirror, being reflected one more time, as indicated in the weight  $\Phi_{BB}$ .

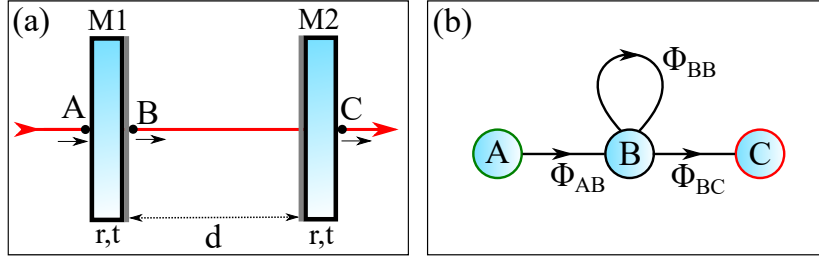


Figure 2.5: (a) Optical schematics of a Fabry-Pérot cavity. Since in this example the cavity's reflection is not of interest, only the output state C is defined. (b) Graph G corresponding to the Fabry-Pérot cavity. The loop in vertex B corresponds to the situation in which the wave-front undergoes one round-trip inside the cavity, going from state B back to state B.

The associated graph is equivalent to the one presented in Figure 2.3(a); thus, we need only to perform a loop contraction to find the response factor for a Fabry-Pérot cavity

$$\Gamma = \Phi_{AB} \left( \sum_{n=0}^{\infty} \Phi_{BB}^n \right) \Phi_{BC} = \frac{\Phi_{AB} \Phi_{BC}}{1 - \Phi_{BB}}. \quad (2-6)$$

Substituting the values of the weights in equation (2-6) yields the expression  $\mathbf{E}_{\text{out}}$  for the transmission of a Fabry-Pérot cavity [71],

$$\mathbf{E}_{\text{out}} = - \frac{t^2 e^{ikd}}{1 - r^2 e^{2ikd}} \mathbf{E}_{\text{in}}. \quad (2-7)$$

## N membranes inside an optical cavity

In optomechanics, more involved graphs arise from a Fabry-Pérot cavity containing thin membranes. The membranes, typically made of Silicon Nitride ( $\text{Si}_3\text{N}_4$ ), act as dispersive optical elements, and change the cavity resonance frequency according to their position with respect to the cavity's nodes [44, 72].

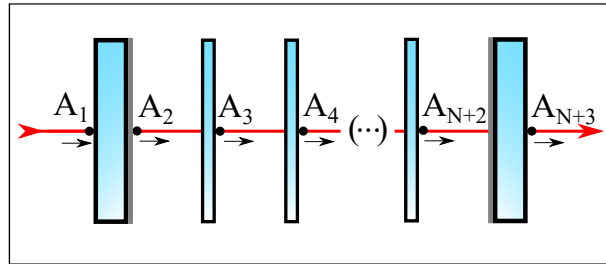


Figure 2.6: Schematics for  $N$  membranes inside a cavity. Since one state is defined before the input mirror and one state is defined after each optical element, there is a total of  $N + 3$  states.

We now consider the general case of  $N$  membranes inside a cavity, as illustrated in Figure 2.6. The optomechanical interaction between optical modes and the membranes has been studied in previous works [60, 61, 73] and will be examined in Section 4. At this moment the focus will be on deriving a method for calculating the system's transmission.

To do so draw the graph formed by the  $N + 3$  vertices corresponding to the states defined in Figure 2.6 and by the edges:

- $\alpha_{k,k+1}$  for  $1 \leq k \leq N+2$ ;
- $\alpha_{k,j}$  for  $2 \leq j < k \leq N+2$ ;
- $\alpha_{k,k}$  for  $2 \leq k \leq N+2$ ;

with  $\alpha_{k,j}$  being the edge from  $A_k$  to  $A_j$ . In particular, the state  $A_{N+2}$  has

- the incoming edge  $\alpha_{N+1,N+2}$ ;
- the outgoing edges  $\alpha_{N+2,k}$ , for  $2 \leq k \leq N+1$ , and  $\alpha_{N+2,N+3}$ ;
- the loop  $\alpha_{N+2,N+2}$ .

Detaching the state  $A_{N+2}$  yields (i) one walk from  $A_{N+1}$  to  $A_k$  as the one shown in Figure 2.7(a) for all  $k$  such that  $2 \leq k \leq N+1$  and (ii) one walk from  $A_{N+1}$  to  $A_{N+3}$  as the one shown in Figure 2.7(b). Eliminating the loop in the walk from  $A_{N+1}$  to  $A_k$ , for  $2 \leq k \leq N+1$ , gives a new edge from  $A_{N+1}$  to  $A_k$  that is in parallel with the initially existing edge  $\alpha_{N+1,k}$ . Merging these two edges yields the final weight for the edge from  $A_{N+1}$  to  $A_k$ :

$$\Phi_{N+1,k}^{(N)'} = \Phi_{N+1,k}^{(N)} + \frac{\Phi_{N+1,N+2}^{(N)} \Phi_{N+2,k}^{(N)}}{1 - \Phi_{N+2,N+2}^{(N)}} \quad (2-8)$$

where the superscript (N) emphasizes that the  $\Phi$ 's in this equation are the ones defined for the  $N$  membranes in the middle case, whereas the prime symbol is used to distinguish the weight after the simplification from the weights before any change is made to the graph.

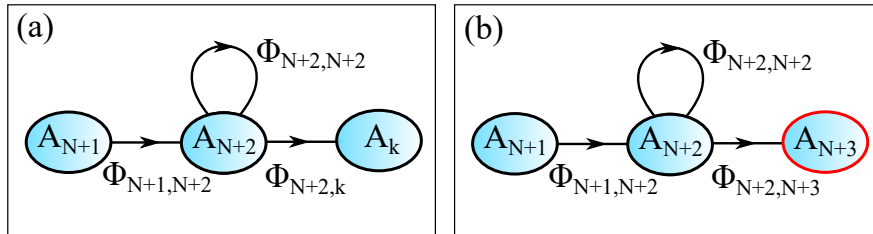


Figure 2.7: Walks arising from the detachment of the state  $A_{N+2}$ : (a) Walk from vertex  $A_{N+1}$  to vertex  $A_k$ , for  $k$  such that  $2 \leq k \leq N+1$ . This walk and the edge  $\alpha_{N+1,k}$  are in parallel. (b) Walk from vertex  $A_{N+1}$  to the output vertex  $A_{N+3}$ .

For the walk from  $A_{N+1}$  to  $A_{N+3}$ , eliminating the loop yields an edge with weight

$$\Phi_{N+1,N+3}^{(N)'} = \frac{\Phi_{N+1,N+2}^{(N)} \Phi_{N+2,N+3}^{(N)}}{1 - \Phi_{N+2,N+2}^{(N)}} \quad (2-9)$$

Renaming the vertex  $A_{N+3}$  to  $A_{N+2}$ , the resulting graph has the same structure, although not the same weights, of a graph for  $N + 1$  membranes: states  $A_k$ , with  $k$  ranging from 1 to  $N+2$ , and the edges

- $\alpha_{k,k+1}$  for  $1 \leq k \leq N+1$ ;
- $\alpha_{k,j}$  for  $2 \leq j < k \leq N+1$ ;
- $\alpha_{k,k}$  for  $2 \leq k \leq N+1$ .

Therefore, if the response factor  $\Gamma^{(N-1)}$  is known for  $N-1$  membranes as a function of the weights  $\Phi_{i,j}^{(N-1)}$ , the response factor  $\Gamma^{(N)}$  for  $N$  membranes can be easily obtained by making the following substitutions

$$\begin{aligned} \Phi_{N+1,N+2}^{(N-1)} &\rightarrow \frac{\Phi_{N+1,N+2}^{(N)} \Phi_{N+2,N+3}^{(N)}}{1 - \Phi_{N+2,N+2}^{(N)}}, \\ \Phi_{N+1,N+2}^{(N-1)} &\rightarrow \Phi_{N+1,k}^{(N)} + \frac{\Phi_{N+1,N+2}^{(N)} \Phi_{N+2,k}^{(N)}}{1 - \Phi_{N+2,N+2}^{(N)}}, \text{ for } 2 \leq k \leq N+1; \\ \Phi_{i,j}^{(N-1)} &\rightarrow \Phi_{i,j}^{(N)}, \text{ for the remaining weights.} \end{aligned} \quad (2-10)$$

The case of an empty Fabry-Pérot cavity ( $N-1 = 0$ ), presented previously, can be used as an example. By making a suitable change in the notation of equation (2-6), the response factor for this cavity is given by

$$\Gamma^{(0)} = \frac{\Phi_{1,2}^{(0)} \Phi_{2,3}^{(0)}}{1 - \Phi_{22}^{(0)}}. \quad (2-11)$$

Now, making the substitutions prescribed in equation (2-10), one arrives at

$$\begin{aligned} \Gamma^{(1)} &= \frac{\Phi_{1,2} [\Phi_{2,3} \Phi_{3,4} / (1 - \Phi_{3,3})]}{1 - [\Phi_{2,2} + \Phi_{2,3} \Phi_{3,2} / (1 - \Phi_{3,3})]} \\ &= \frac{\Phi_{1,2} \Phi_{2,3} \Phi_{3,4}}{1 - \Phi_{2,2} - \Phi_{3,3} + \Phi_{2,2} \Phi_{3,3} - \Phi_{2,3} \Phi_{3,2}}, \end{aligned} \quad (2-12)$$

where the superscript (1) in all the  $\Phi$ 's has been omitted. This is the right expression for the response factor of a cavity containing one membrane, as can be directly verified by calculating  $\Gamma^{(1)}$  from the graph shown in Figure 2.8.

Note that to get the structure of the graph for  $N-1$  membranes starting from the graph for  $N$  membranes,  $N+1$  loop eliminations followed by  $N$  merges



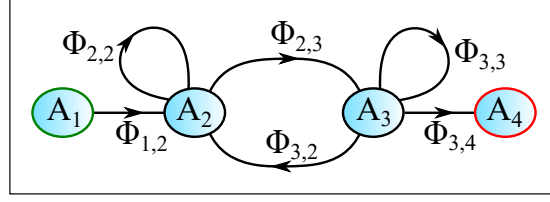


Figure 2.8: Graph associated to the transmission of a cavity with a membrane in the middle. Applying the simplification described in the present Section to this graph yields the graph associated to a cavity with no membranes inside of it. Conversely, applying the substitutions prescribed in equation (2-10) to the response factor of a Fabry-Perót cavity gives the response factor for the displayed graph.

of edges in parallel are necessary. Therefore, the number of operations in this procedure is of order  $\mathcal{O}(N)$ . By repeating this process it is possible to simplify the graph for  $N$  membranes to get a single edge connecting the initial and final vertices with a number of operations that is of order  $\mathcal{O}(N^2)$ .

## 2.4

### Multiple inputs and outputs

Up to this point solely interferometers with one input and one output have been studied, but the presented graph-based method can be easily generalized for homodyne systems containing an arbitrary number of inputs and outputs.

As discussed in the end of Section 2.2, the simplification rules are local, and, therefore, must remain valid regardless of the number of I/O vertices. A difference appears at each output, where one must sum over the fields coming from each input port of the interferometer. In terms of the response factors, the electric field in a given output  $O_M$  is

$$\mathbf{E}_{O_m} = \sum_n \Gamma_{nm} \mathbf{E}_{I_n} \quad (2-13)$$

where  $n$  must run over all input ports.

The following example serves to illustrate how to find the transmitted field through an interferometer with multiple inputs/outputs. The Mach-Zehnder interferometer displayed in Figure 2.9(a) has two BS's, with reflectance and transmittance  $r, t$  as well as two perfect mirrors. The phase shift between each arm of the interferometer is taken to be  $\theta$ , due to a phase shifter.

States A through F are defined, giving rise to the graph in Figure 2.9(b),

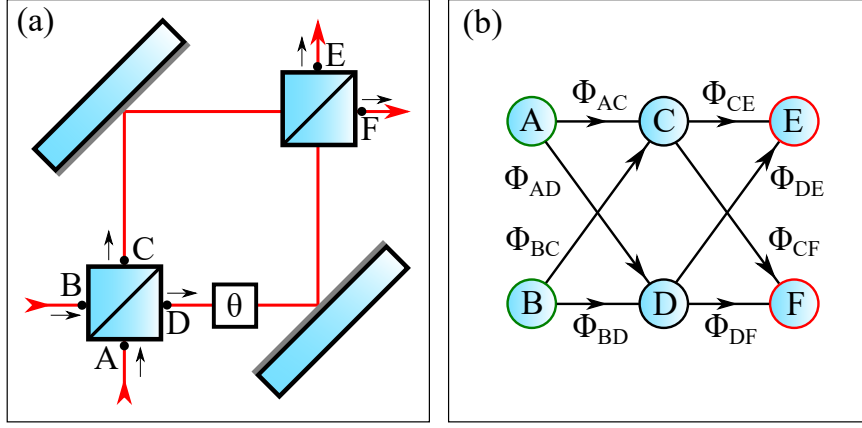


Figure 2.9: (a) Optical schematics corresponding to a Mach-Zehnder interferometer. Differences between the two paths inside the interferometer are summarized by a phase  $\theta$ . (b) Graph corresponding to the Mach-Zehnder interferometer, with two input states, indicated by the green circles, and two output states, indicated by the red circles.

with the following weights

$$\begin{aligned}
 \Phi_{AC} &= it & \Phi_{AD} &= r \\
 \Phi_{BC} &= r & \Phi_{BD} &= it \\
 \Phi_{CE} &= r & \Phi_{CF} &= it \\
 \Phi_{DE} &= ite^{i\theta} & \Phi_{DF} &= re^{i\theta}
 \end{aligned} \tag{2-14}$$

To find the transmitted field through the interferometer, first one needs to detach the edges on vertices C and D and then replace the resulting consecutive and parallel edges. This sequence of operation is shown in Figure 2.10.

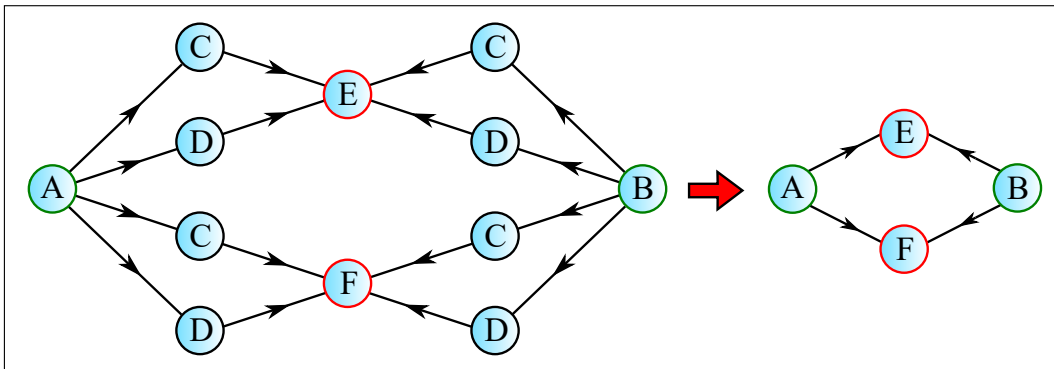


Figure 2.10: Simplification of the graph corresponding to a Mach-Zehnder interferometer. The graph is simplified until all that remains are the input and output vertices.

The output electric field at the output state E [F] will be the sum of the output electric field in E [F] coming from state A and the output electric field

in E [F] coming from state B

$$\begin{aligned}\mathbf{E}_{\text{out, E}} &= (\Phi_{AC}\Phi_{CE} + \Phi_{AD}\Phi_{DE})\mathbf{E}_{\text{in,A}} + (\Phi_{BC}\Phi_{CE} + \Phi_{BD}\Phi_{DE})\mathbf{E}_{\text{in,B}}, \\ \mathbf{E}_{\text{out, F}} &= (\Phi_{AC}\Phi_{CF} + \Phi_{AD}\Phi_{DF})\mathbf{E}_{\text{in,A}} + (\Phi_{BC}\Phi_{CF} + \Phi_{BD}\Phi_{DF})\mathbf{E}_{\text{in,B}}.\end{aligned}\quad (2-15)$$

Plugging the edge weights from equation (2-14) into equation (2-15) the standard result is obtained

$$\begin{aligned}\mathbf{E}_{\text{out, E}} &= irt\left(1 + e^{i\theta}\right)\mathbf{E}_{\text{in,A}} + \left(r^2 - t^2e^{i\theta}\right)\mathbf{E}_{\text{in,B}}, \\ \mathbf{E}_{\text{out, F}} &= \left(r^2e^{i\theta} - t^2\right)\mathbf{E}_{\text{in,A}} + irt\left(1 + e^{i\theta}\right)\mathbf{E}_{\text{in,B}}.\end{aligned}\quad (2-16)$$

For an interferometer with  $N$  input ports and  $N$  output ports, the relation in equation (2-13) can be expressed in matrix form as

$$\mathbf{v}_O = U\mathbf{v}_I, \quad (2-17)$$

where  $\mathbf{v}_O = [\mathbf{E}_{O_1} \cdots \mathbf{E}_{O_N}]$ ,  $\mathbf{v}_I = [\mathbf{E}_{I_1} \cdots \mathbf{E}_{I_N}]$  and  $U$  is a  $N \times N$  matrix with  $U_{nm} \equiv \Gamma_{mn}$ . If all inputs and outputs of the interferometer are taken into account, the unitarity of  $U$  follows from the conservation of energy in the system. Therefore, the initial interferometer is a physical implementation of the unitary matrix  $U$ . This matter has been addressed previously, and the combination of BS and phase-shifters has been shown to be sufficient for implementing any unitary matrix [74, 75].

## 2.5

### Quantum interferometry

The present graph-based method can also be used to describe interferometers whose inputs are not classical electric fields, but quantum states of light [76].

So far the effect of an interferometer upon input electric fields transforming into output electric fields has been described. With second quantization, the same principle can be applied to unravel how the input modes' creation/annihilation operators evolve to the output modes' creation/annihilation operators.

In order to do so, note that the response factors carry information about how much of the light that enters an interferometer through one port leaves it through another, as well as the phase gained by doing so. This can be described mathematically by a transformation of the form

$$\hat{a}^\dagger \rightarrow \Gamma_{AB} \hat{b}^\dagger + \Gamma_{AC} \hat{c}^\dagger + \cdots, \quad (2-18)$$

where  $\hat{a}^\dagger$  is the creation operator associated with the input state A;  $\hat{b}^\dagger, \hat{c}^\dagger, \dots$  are the creation operators associated with the output states B, C, ... and  $\Gamma_{AB}, \Gamma_{AC}, \dots$  are the response factors between state A and states B, C, and so on.

When treating quantum states of light, all possible optical paths must be considered, otherwise, the evolution of the input creation operators will not be unitary. This is in contrast with the classical case, in which paths that are not of interest might be ignored.

As a final remark, any multi-mode quantum state in the Fock basis can be written as a function of each mode's creation and annihilation operators acting on the vacuum state

$$|\psi\rangle = \hat{\Psi}(\hat{a}, \hat{b}, \hat{c}, \dots, \hat{a}^\dagger, \hat{b}^\dagger, \hat{c}^\dagger, \dots)|0\rangle \quad (2-19)$$

and so, the effect of the interferometer upon an arbitrary input quantum state can be obtained by transforming the input modes according to the interferometer.

## 2.6

### Conclusions

In summary, we have shown how to associate a directed weighted graph to an interferometric setup. Using the so-called simplification rules, it is possible to transform the directed graph, as to simplify it as much as possible, and get the response factors for the interferometer's outputs. From these response factors, the electric field, as well as quantum states of light in the Fock basis, within an interferometer can be obtained.

To illustrate the technique, several examples were analysed, such as the Michelson, Fabry-Pérot and Mach-Zehnder interferometers, and the optomechanical setups of multiple membranes inside an optical cavity.

The graphical approach provides a clear physical picture in contrast to the standard transfer-matrix approach, by translating the physical problem of calculating the electrical field in an interferometer to a combinatorial problem. This clear picture combined with our simplification rules may also provide insight on new correspondences between physical implementations and abstract structures such as graphs [77, 78] and matrices [74, 75].

Tightly focused laser beams can be used to exert forces upon dielectric particles. If the particle's refractive index is *larger* than that of its surroundings, the laser pulls it to regions of higher intensity of light. This technique, introduced by Arthur Ashkin in 1986 [13] and known today as optical tweezing, allows one to hold and manipulate very tiny objects and finds applications in a large number of fields ranging from biology [79–82] to fundamental physics [83–87]. In standard optical tweezers, Gaussian beams are used to create the trapping focus. To a good approximation, the trap can be described as a three dimensional quadratic potential.

Notably it was also pointed out by Ashkin that air droplets immersed in water were pushed away from the Gaussian focus [88]. This is a consequence of the fact that when the refractive index of the particle is *smaller* than that of its surroundings, the particle is repelled from the region of high intensity. One can then envision an *inverted* optical trap, in which an engineered beam of light has a high-intensity boundary and a dark focus. A particle with the appropriate refractive index will be trapped within the dark focus by the absence of light [89]. We refer to this type of beam, which was first proposed as a tool to trap atoms [90–93], as *bottle beams*.

In this chapter, we will study how optical beams can interact and effectively trap micron-sized particles, including living organisms. In Section 3.1, we present fundamental beam modes: Gaussian beam and Laguerre-Gauss (LG) beam, and a composition of both: the optical bottle beam. In Section 3.2, in two different regimes, we show how transfer of momentum between an optical beam and a particle gives rise to effective optical forces acting on the latter. In Section 3.3, the standard optical trapping technique using a Gaussian beam is shown to generate approximately a 3D harmonic potential close to its focus, which can optically levitate dielectric particles. Finally, in Section 3.4, we present the results obtained in our work [94], studying optical trapping using bottle beams.

### 3.1

#### Optical Beams 101

In the absence of charges, Maxwell's equations are known to give rise to wave equations for both the electric and magnetic fields. When modelling laser beams it is useful to consider the paraxial approximation [95], i.e., beams propagating in a given direction along which its spatial profile varies much slower than its transverse profile [69]. Under this approximation, the electromagnetic fields obey the paraxial Helmholtz equation

$$\nabla_{\perp}^2 E(x, y, z) + 2ik \frac{\partial E}{\partial z}(x, y, z) = 0, \quad (3-1)$$

for an optical beam with electric field amplitude  $E(x, y, z)$  propagating in the  $z$  direction;  $\nabla_{\perp}^2 \equiv \frac{\partial^2}{\partial x^2} + \frac{\partial^2}{\partial y^2}$  denotes the Laplacian operator in the transverse directions to the propagation. We note here that throughout this Chapter we will consider linearly polarized electric fields only.

#### 3.1.1

##### Laguerre-Gauss beam

The LG modes describe a complete orthonormal set of solutions for the paraxial Helmholtz equation, therefore any optical beam's spatial profile can be decomposed into a combination of LG modes. Its electric field magnitude is given by

$$E_{\ell,p}^{LG}(\rho, \phi, z) = \sqrt{\frac{4P_0}{c\epsilon\pi\omega(z)^2}} \sqrt{\frac{p!}{(|\ell|+p)!}} \left(\frac{\sqrt{2}\rho}{\omega(z)}\right)^{|\ell|} L_p^{|\ell|}\left(\frac{2\rho^2}{\omega(z)^2}\right) \\ \times \exp\left[-\frac{\rho^2}{\omega(z)^2}\right] \exp\left[ik_m z + ik_m \frac{\rho^2}{2R(z)} - i\zeta(z) + i\ell\phi\right], \quad (3-2)$$

where  $c$  is the speed of light,  $\epsilon$  is the medium's permittivity,  $P_0$  is the laser power,  $k_m$  is the wavenumber in the medium and  $\omega(z)$ ,  $R(z)$ ,  $\zeta(z)$  and  $L_p^{|\ell|}$  are respectively the beam width, the wavefront radius, the Gouy phase and the associated Laguerre polynomial. These quantities are respectively given by

$$\omega(z) = \omega_0 \sqrt{1 + \frac{z^2}{z_R^2}}; \quad (3-3)$$

$$R(z) = z \left(1 + \frac{z_R^2}{z^2}\right); \quad (3-4)$$

$$\zeta(z) = (2p + |\ell| + 1) \arctan \frac{z}{z_R}; \quad (3-5)$$

$$L_p^{|\ell|}(x) = \sum_{i=0}^p \frac{1}{i!} \binom{p+|\ell|}{p-i} (-x)^i \quad (3-6)$$

where the Rayleigh range ( $z_R$ ) and the beam waist ( $\omega_0$ ) are defined as

$$\omega_0 = \frac{\lambda_0}{\pi NA}, \quad z_R = \frac{n_m \lambda_0}{\pi NA^2} \quad (3-7)$$

with  $\lambda_0$  the wavelength in vacuum,  $n_m$  the medium refractive index and  $NA = \lambda_0/(\pi\omega_0)$  the numerical aperture. In Figure 3.1, we present the transverse intensity profile for Laguerre-Gauss beams with  $\ell, p \in 0, 1, 2$ .

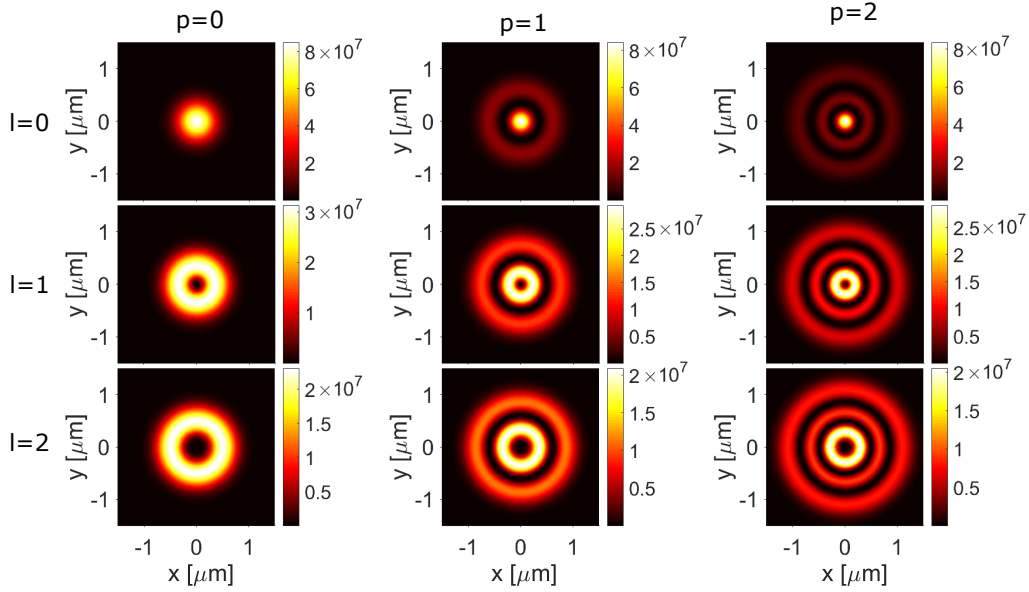


Figure 3.1: Intensities for profiles for Laguerre-Gauss beams at their focal plane,  $z = 0$ . For this simulation, we used:  $n_m = 1.33$ ,  $NA = 0.5$ ,  $\lambda = 780$  nm,  $P_0 = 50$  mW.

### 3.1.2

#### Gaussian beam

The fundamental LG beam with  $\ell = 0, p = 0$  is shown in the first plot of Figure 3.1. Its electric field magnitude is given by

$$E^G(\rho, z) = \sqrt{\frac{4P_0}{c\epsilon\pi\omega(z)^2}} \exp \left[ -\frac{\rho^2}{\omega(z)^2} + ik_m z + ik_m \frac{\rho^2}{2R(z)} - i \arctan\left(\frac{z}{z_R}\right) + i\ell\phi \right], \quad (3-8)$$

This fundamental LG mode is also called a Gaussian mode as its intensity profile in the plane transversal to its propagation direction follows a gaussian distribution

$$I = \frac{n_m \epsilon_0 c}{2} |E^G(\rho, z)|^2 = \frac{2Pn_m}{\pi\omega^2(z)} e^{-\frac{2\rho^2}{\omega^2(z)}}. \quad (3-9)$$

### 3.1.3

#### Optical Bottle beam

A bottle beam, such as the one proposed in [96], is one example in an infinite number of possible engineered optical traps aimed at different purposes such as Bessel beams [97], frozen waves [98], circular Airy beams [99–101], radially polarized beams [102, 103], and many others [104–109].

Several techniques can be employed to create bottle beams, such as the generation of Bessel beams using axicons [110–112], the interference of Gaussian beams of different waists [113] and the superposition of different modes [114–116] created using Spatial Light Modulators. Here, we focus on the bottle beam created by the superposition of a Gaussian beam and a Laguerre-Gauss beam with  $\ell = 0, p \neq 0$ , each with power  $P_0$ , and a relative phase of  $\pi$  presented in [96].

The intensity of such bottle beam reads

$$I_p(\rho, z) = I_0 \frac{\omega_0^2}{\omega(z)^2} \exp \left[ -\frac{2\rho^2}{\omega(z)^2} \right] \times \left[ 1 - 2 \cos \left( 2p \arctan \frac{z}{z_R} \right) L_p^0 \left( \frac{2\rho^2}{\omega(z)^2} \right) + L_p^0 \left( \frac{2\rho^2}{\omega(z)^2} \right)^2 \right] \quad (3-10)$$

where  $I_0 = 2P_0/\pi\omega_0^2$  is the intensity at the origin of the Gaussian beam. Figures 3.2(a) and 3.2(b) shows the intensity as a function of the transverse coordinate  $x$  and the longitudinal coordinate  $z$ . The potential landscape in the  $xz$  plane is shown in Figures 3.2(c) for the cases  $p = 1$ , and 3.2(d)  $p = 2$ . A dielectric particle with the appropriate refractive index placed at the origin would be trapped in the dark focus, since it would be repelled in all directions by the surrounding regions of higher electromagnetic intensity.

#### Dimensions of the bottle

We can define the width  $W$  (height  $H$ ) of the bottle as the distance between the two intensity maxima surrounding the dark region along the  $x$  axis ( $z$  axis). These values can be found by solving

$$dI_p(x, 0, 0)/dx|_{x=W/2} = 0, \quad (3-11)$$

$$dI_p(z, 0, 0)/dz|_{z=H/2} = 0. \quad (3-12)$$

The above equations admit analytical solutions for small  $p$ , yielding  $W = 2\omega_0, H = 2z_R$  for  $p = 1$  and  $W = 2\sqrt{2 - \sqrt{2}\omega_0}, H = \sqrt{2}z_R$  for  $p = 2$ .



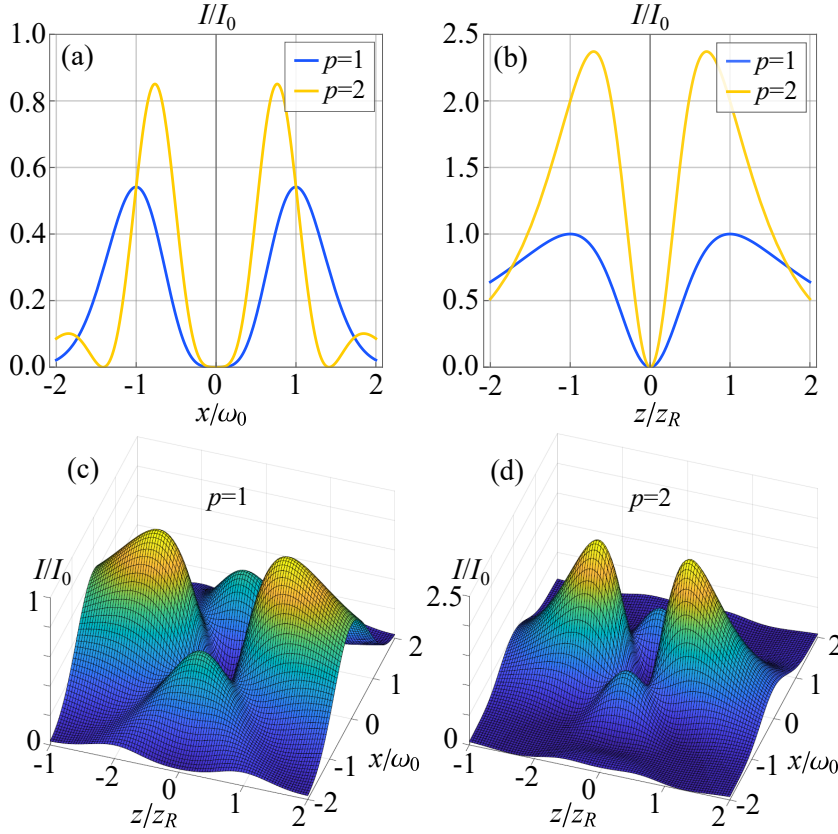


Figure 3.2: Intensity in the (a) radial and (b) axial directions for bottle beams with  $p = 1$  and  $p = 2$ . Intensity landscape in the  $xz$  plane for bottle beams with (c)  $p = 1$  and (d)  $p = 2$ . Due to the normalization of  $x$ ,  $z$  and  $I$ , these plots depend only on  $p$ , and are independent from the remaining beam parameters.

To gain insight into  $H$  and  $W$  it is useful to make the change of variables  $\rho/\omega_0 \rightarrow \rho'$ ,  $z/z_R \rightarrow z'$  in the intensity given in Eq.(3-10). The function  $I_p(\rho', z')$  has no explicit dependence on any of the beam's parameters other than  $p$  and  $I_0$ , with its associated re-scaled width  $W'$  and height  $H'$ . The pre-factor  $I_0$  does not alter the distance between maxima along the  $x'$  and  $z'$  axis, meaning that  $W' = W'(p)$  and  $H' = H'(p)$  depend only on  $p$ . Going back to the original variables we find that  $W = \omega_0 W'(p)$  and  $H = z_R H'(p)$ . From Eq. (3-7), we observe that the width of the bottle scales with  $\text{NA}^{-1}$  and the height scales with  $\text{NA}^{-2}$ . Hence an increase in  $\text{NA}$  causes the bottle to become overall smaller and compressed along the  $z$  direction.

### Total power of a bottle beam

In order to find the exact relation between  $P_0$  and the total power of the beam, we need to integrate equation (3-10) along some plane orthogonal to

the propagation of the beam. Choosing the plane  $z = 0$ ,

$$\begin{aligned}
 P &= \int_0^\infty d\rho \int_0^{2\pi} (d\theta \rho) I_0 e^{-2\rho^2/\omega_0^2} \left[ 1 - 2L_p^0 \left( \frac{2\rho^2}{\omega_0^2} \right) + L_p^0 \left( \frac{2\rho^2}{\omega_0^2} \right)^2 \right] \\
 &= 2\pi I_0 \int_0^\infty \frac{\omega_0^2 du}{4} e^{-u} [1 - 2L_p^0(u) + L_p^0(u)^2] \\
 &= P_0 \int_0^\infty du e^{-u} [1 - 2L_p^0(u) + L_p^0(u)^2].
 \end{aligned} \tag{3-13}$$

The Laguerre-Polynomials satisfy

$$\int_0^\infty x^\ell e^{-x} L_p^{|\ell|}(x) L_q^{|\ell|}(x) = \frac{(p+\ell)!}{p!} \delta_{p,q}, \tag{3-14}$$

which implies that we have the following relation between the total power of a bottle beam and the power of each beam in the superposition

$$P = 2P_0. \tag{3-15}$$

## 3.2

### Optical Forces

Light carries both energy and momentum. When an incident light beam hits a particle, exchange of momentum between them gives rise to effective force on the particle. Consider, for example, a single photon with wavelength  $\lambda$  and wavenumber  $k = 2\pi/\lambda$  carrying momentum  $\hbar k$ . If a violet light photon,  $\lambda = 380 \text{ nm}$ , were to hit and reflect on a particle, it would result in maximal momentum transfer of [23]  $|\Delta p| = 2\hbar k \approx 1.7 \times 10^{-27} \text{ kg} \cdot \text{m/s}$ . Therefore, such force is feeble in everyday life.

However, when considering very light particles and/or highly focused light beams, this force builds up and can influence the motion of the object. In the following, we quantitatively address these optical forces for both the cases when a dielectric is much smaller than the wavelength of the trapping beam and when it is comparable to it.

#### 3.2.1

##### Dipole Approximation

When a dielectric particle of mass  $m$  and radius  $R$  is placed in a monochromatic EM field of wavelength  $\lambda$  such that  $R \ll \lambda$ , we can approximate the particle as a dipole consisting of two point charges  $-q$  and  $+q$ , each of mass  $m/2$ , at positions  $r_-$  and  $r_+$ , respectively. An electric dipole experiences Lorentz forces from the external incident electric  $\mathbf{E}_i$  and magnetic  $\mathbf{B}_i$  fields, therefore, its equation of motions are [117]

$$\frac{m}{2} \frac{d^2 \mathbf{r}_+}{dt^2} = +q \operatorname{Re} \left\{ \mathbf{E}_i(\mathbf{r}_+, t) + \frac{d\mathbf{r}_+}{dt} \times \mathbf{B}_i(\mathbf{r}_+, t) \right\}, \quad (3-16)$$

$$\frac{m}{2} \frac{d^2 \mathbf{r}_-}{dt^2} = -q \operatorname{Re} \left\{ \mathbf{E}_i(\mathbf{r}_-, t) + \frac{d\mathbf{r}_-}{dt} \times \mathbf{B}_i(\mathbf{r}_-, t) \right\}, \quad (3-17)$$

We can find the optical force on the particle by summing both equations above in order to find the equation of motion for the dielectric's position  $\mathbf{r}_d = \frac{\mathbf{r}_+ + \mathbf{r}_-}{2}$ . As the particle is much smaller than the EM's wavelength, the electric field varies smoothly inside the dielectric and we expand it up to first order, arriving at

$$m \frac{d^2 \mathbf{r}_d}{dt^2} = +q \operatorname{Re} \left\{ (\mathbf{r}_+ - \mathbf{r}_-) \cdot \nabla \mathbf{E}_i(\mathbf{r}_d, t) + \frac{d(\mathbf{r}_+ - \mathbf{r}_-)}{dt} \times \mathbf{B}_i(\mathbf{r}_d, t) \right\}. \quad (3-18)$$

We now assume that the particle is a linear dielectric, such that its polarization vector  $\mathbf{p} \equiv +q(\mathbf{r}_+ - \mathbf{r}_-)$  can be written as  $\mathbf{p} = \alpha \mathbf{E}_i$ , where  $\alpha_s = 4\pi\epsilon_0 R^3(n_R^2 - 1)/(n_R^2 + 2)$  is the static polarizability such that [69, 118]

$$\alpha = \alpha_s + i \frac{k^3}{6\pi\epsilon_0} |\alpha_s|^2 \quad (3-19)$$

is the complex particle polarizability with  $n_R$  its refractive index,  $k = 2\pi/\lambda$  the external incident field wavenumber, and  $\epsilon_0$  the medium's permittivity. After some manipulation, we arrive at [118]

$$m \frac{d^2 \mathbf{r}_d}{dt^2} = \operatorname{Re} \left\{ \frac{\alpha}{2} \nabla \mathbf{E}_i^2(\mathbf{r}_d, t) + \frac{d}{dt} \left[ \mathbf{E}_i(\mathbf{r}_d, t) \times \mathbf{B}_i(\mathbf{r}_d, t) \right] \right\}. \quad (3-20)$$

We remember that the incident fields are time-harmonic, which allows us to simplify the derivative above. More so, as the EM field oscillates much faster than we can sample, we take the time average of the right hand side of the above equation in order to arrive at the optical forces acting on a dielectric particle

$$m \frac{d^2 \mathbf{r}_d}{dt^2} = \operatorname{Re} \left\{ \frac{\alpha}{4} \nabla |\mathbf{E}_i(\mathbf{r}_d)|^2 - i\omega \mathbf{E}_i(\mathbf{r}_d) \times \mathbf{B}_i^*(\mathbf{r}_d) \right\}. \quad (3-21)$$

Employing the formula for the complex polarizability, Equation (3-19), and the fact that the fields propagate in the  $z$  direction, after some tedious manipulations, we arrive at two forces [69, 118, 119]

$$\mathbf{F}^{(scat)}(\mathbf{r}) = \hat{\mathbf{z}} \frac{128\pi^5 R^6}{3c\lambda^4} \left( \frac{m^2 - 1}{m^2 + 2} \right)^2 n_m^5 I(\mathbf{r}), \quad (3-22)$$

$$\mathbf{F}^{(grad)}(\mathbf{r}) = \frac{2\pi n_m R^3}{c} \left( \frac{m^2 - 1}{m^2 + 2} \right) \nabla I(\mathbf{r}), \quad (3-23)$$

where  $m = n_p/n_m$  is the particle-medium refractive index ratio and  $I = \frac{n_m \epsilon_0 c}{2} |\mathbf{E}_i(\mathbf{r})|^2$  is the intensity of the incident field.

The first is called scattering force, and is proportional to the Poynting vector. Near the origin, the scattering force points in the direction of propagation of the beam. The second is called gradient force and it is proportional to the gradient of the intensity of the external electromagnetic field. Note that, for  $m > 1$ , the latter points towards the region with higher light intensity, pulling the particle closer to this region; for  $m < 1$ , this force repels the particle away from the region with higher light intensity.

Moreover, we note that while the scattering force is non-conservative, the gradient force is, following the optical potential given by [69, 118, 119]

$$V(\mathbf{r}) = -\frac{2\pi n_m R^3}{c} \left( \frac{m^2 - 1}{m^2 + 2} \right) I(\mathbf{r}). \quad (3-24)$$

We briefly comment that we have not included in our discussion a third force, called spin-curl force, which is a result of polarisation gradients [120], and can be disregarded in the case of uniform linear polarization we are interested in.

### 3.2.2

#### Intermediate Regime

In many applications it is desirable to trap ‘large’ micron-sized particles such as living cells [121, 122]. This presents an intermediate regime, in which the size of the particle is comparable to the wavelength of the trapping beam ( $R \approx \lambda$ ) and neither the dipole ( $R \ll \lambda$ ) nor geometric optics ( $R \gg \lambda$ ) approximations can be used to calculate the optical forces. Instead, the forces must be calculated using the so-called generalized Lorenz–Mie theory, for which we provide a brief introduction following the treatment presented in [123].

#### Generalized Lorenz-Mie Theory

Regardless of the size of the trapped particle, optical forces arise from the exchange of momentum with the photons from the trapping beam. Therefore, the total momentum transferred to the particle is equal to the change in momentum of the scattered electromagnetic field. It is then useful to separate the field in incoming  $\mathbf{E}_{in}$  and outgoing  $\mathbf{E}_{out}$  parts, which in turn can be expanded in terms of vector spherical wave-functions (VSWFs) defined in a

coordinate system centered at the particle's center,

$$\mathbf{E}_{in} = \sum_{i=1}^{\infty} \sum_{j=-i}^i a_{ij} \mathbf{M}_{ij}^{(2)}(k\mathbf{r}) + b_{ij} \mathbf{N}_{ij}^{(2)}(k\mathbf{r}), \quad (3-25)$$

$$\mathbf{E}_{out} = \sum_{i=1}^{\infty} \sum_{j=-i}^i p_{ij} \mathbf{M}_{ij}^{(1)}(k\mathbf{r}) + q_{ij} \mathbf{N}_{ij}^{(1)}(k\mathbf{r}), \quad (3-26)$$

where  $\mathbf{M}_{ij}^{(1)}$ ,  $\mathbf{N}_{ij}^{(1)}$ ,  $\mathbf{M}_{ij}^{(2)}$  and  $\mathbf{N}_{ij}^{(2)}$  are the VSWFs, with the upper index (1) standing for outward-propagating transverse electric and transverse magnetic multipole fields and (2) for the corresponding inward-propagating multipole fields.

The coefficients  $a_{ij}$  and  $b_{ij}$  can be calculated for the incident beam and used to obtain the  $p_{ij}$  and  $q_{ij}$  coefficients for the scattered field by a simple matrix-vector multiplication between the so-called  $T$ -matrix and a vector containing the coefficients of the incoming field. The  $T$ -matrix depends only on the characteristics of the trapped particle, which we assume spherical. Once the coefficients are calculated, the force along the axial direction  $z$  is given by

$$\begin{aligned} F_z = & \frac{2n_{md}P}{cS} \sum_{i=1}^{\infty} \sum_{j=-1}^i \frac{j}{i(i+1)} \text{Re}(a_{ij}^* b_{ij} - p_{ij}^* q_{ij}) - \\ & \frac{1}{i+1} \sqrt{\frac{i(i+2)(i-j+1)(i+j+1)}{(2i+1)(2i+3)}} \times \\ & \text{Re}(a_{ij} a_{i+1,j}^* + b_{ij} b_{i+1,j}^* - p_{ij} p_{i+1,j}^* - q_{ij} q_{i+1,j}^*) \end{aligned} \quad (3-27)$$

with

$$S = \sum_{i=1}^{\infty} \sum_{j=-i}^i (|a_{ij}|^2 + |b_{ij}|^2). \quad (3-28)$$

Forces acting along the  $x$  and  $y$  axis have more complicated formulae and can be more easily calculated by rotating the coordinate system. The effect of displacing the particle can be taken into account by appropriate translations of the trapping beam.

Due to the linearity of Eqs. (3-25) and (3-26), the expansion coefficients for a superposition of different beams can be found by adding the expansion coefficients for each beam, and subsequently substituted in Eq. (3-27) to calculate the resultant force. In the following Sections, we shall use the latest version of the toolbox developed in [123] to perform these computations for the case of a particle trapped by a bottle beam.

### 3.3

#### Optical Trapping in a Bright Focus

We know that a gaussian beam will be able to 3D trap a dielectric nanosphere with  $m = n_p/n_m > 1$ . This can be promptly noticed by the intensity profile of a gaussian beam, Equation (3-9), and the form of the forces acting on it in the dipole regime, Equations (3-22) and (3-23). The condition  $m > 1$  sets the gradient force to point towards the higher-intensity region, i.e., the center of the gaussian beam. If the particles moves away from the focus of the beam, this force pull it back, effectively trapping it in any direction.

Close to the focus of a gaussian beam, we can Taylor expand its intensity up to second order as

$$I(\rho, z) \simeq \frac{2Pn_m}{\pi\omega_0^2} - \frac{2Pn_m}{\pi\omega_0^2 z_R^2} z^2 - \frac{4Pn_m}{\pi\omega_0^4} \rho^2, \quad (3-29)$$

from which we observe that the optical potential, Equation (3-24), acts as a 3D harmonic well that traps dielectric particles close to the focus of a gaussian beam.

As an example, consider a nanosphere of silica, refractive index  $n_p = 1.46$  and radius  $R = 50$  nm, in suspension in water,  $n_m = 1.33$ . These pair of particle and medium are chosen such that we have  $m > 1$  implying that the sphere will be attracted to the higher-intensity region. We choose to shine a gaussian beam in this particle, with the same parameters present as in the first plot of figure 3.1.

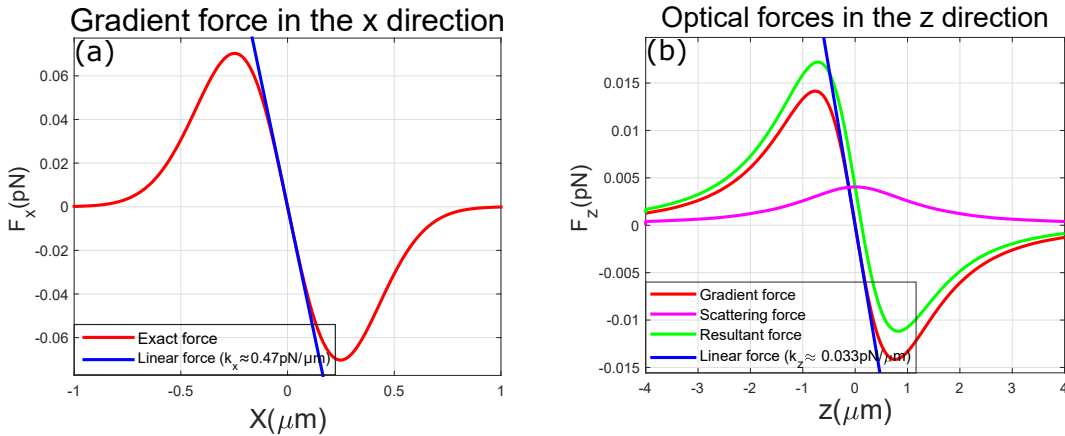


Figure 3.3: Forces generated by a Gaussian optical trap: (a) in the radial direction  $x$ ; (b) in the longitudinal direction  $z$ .

The gradient force in the  $x$  direction is plotted in figure 3.3(a) as a function of the displacement in that same direction when  $y = z = 0$ . As it can be seen, the force is approximately linear for small displacements, which

could be approximated by a harmonic force,  $F = -k_x x$ , with spring constant  $k_x \approx 0.47 \text{ pN}/\mu\text{m}$ , and analogously for the  $y$  direction as the beam intensity is symmetric in the plane transversal to the propagation. The same is true for the gradient force in the  $z$  direction ( $k_z \approx 0.033 \text{ pN}/\mu\text{m}$ ), plotted in figure 3.3(b) together with the scattering force and the resultant force. As it can be seen, the scattering force shifts the equilibrium position ( $F_{res}(z) = 0 \rightarrow z \approx 123 \text{ nm}$ ), while maintaining an harmonic approximation,  $k'_z \approx 0.032 \text{ pN}/\mu\text{m}$ .

We observe that as the density of silica is approximately twice the density of water [54], although the nanosphere is suspended in a liquid, it would not float due to buoyancy. More so, for the case in question, the weight of the particle would only account for a gravitational force 3 orders of magnitude lower than the resultant optical force in the  $z$  direction that the particle feels. Thus, the particle would be trapped.

### 3.4

#### Optical Trapping in a Dark Focus

The bottle beam, defined in Section 3.1.3, is an interesting choice for a trapping potential for a number of reasons. First, as we will show, it yields a simple mathematical description from which the trapping potential can be readily obtained. Moreover, description of the trap in terms of its width, height and shape are simple and clearly defined. Furthermore, such superposition is promptly obtained by the use of a Spatial Light Modulator (SLM), a well established technique for engineering structured light beams available in the laboratory [124–127].

Because optical trapping can be applied to particles in a wide size range [128, 129], we analyse both the cases of small Rayleigh particles and of larger micron-sized particles, following our discussion in Section 3.2. In the former, the optical forces and potential are derived from the dipole approximation and thoroughly analysed under different assumptions, which are verified by simulating the motion of the trapped particle in a viscous medium. In the latter, generalized Lorenz–Mie theory is employed to calculate the forces caused by the beam, with the aid of the tools introduced in [123]. Constraints on the numerical aperture, particle size and relative refractive index are found.

Understanding particle dynamics under the influence of a bottle beam can lead to striking applications. Notably, the bottle is an interesting tool for trapping experiments requiring little or no light scattering upon the trapped object. This is of particular interest in biology, where trapping a living cell or organelles within the cell without the constant influence of laser light might be crucial to reveal mechanical properties of the organism without excessive

heating and laser interference [130–132]. We thus propose a set of experimental parameters that could be used to trap living organisms in the dark focus of a bottle beam.

### 3.4.1

#### Radiation forces in the Dipole Approximation

Following our discussion in Section 3.2, we are interested in situations in which the parameter  $m = n_p/n_m$  is smaller than 1, in such a way that the particle is repelled by light. From the intensity given by Eq. (3-10), the scattering force  $\mathbf{F}_p^{(scat)}(\mathbf{r})$ , the gradient force  $\mathbf{F}_p^{(grad)}(\mathbf{r})$  and the optical potential  $V_p(\mathbf{r})$  acting on a trapped particle with radius  $R$  and refractive index  $n_p$  can be readily calculated using Equations (3-22 – 3-24).

The forces acting on a spherical water droplet ( $n_p = 1.33$ ) with 70 nm radius trapped in oil ( $n_m = 1.46$ ) by a bottle beam ( $\lambda = 780$  nm,  $P_0 = 200$  mW for each beam in the superposition) focused by an objective lens (NA = 0.5) are displayed in Figure 3.4. Latter on we will also consider the environmental effects on the dynamics of the particle. As expected, the gradient forces point to the origin. Note that the scattering force, which points along the propagation direction, is null at the equilibrium position. This is in strong contrast to standard Gaussian traps and presents an advantage since the imbalance between scattering and gradient forces often poses challenges to optical trapping [133].

Another interesting feature of the bottle beam trap is the flat bottom of the intensity well in the  $z = 0$  plane, seen in Figure 3.2(a), and the approximate null derivative of the force along the radial direction at the origin. This can be understood by looking at the potential near the origin ( $\rho \ll \omega_0$ ,  $z \ll z_R$ ). It can be approximated to 4<sup>th</sup> order as

$$\frac{V_p(\rho, z)}{V_0} \approx \underbrace{\frac{4p^2}{\omega_0^4} \rho^4}_{T_{\rho^4}} - \underbrace{\frac{8p^2(p+1)}{\omega_0^2 z_R^2} \rho^2 z^2}_{T_{\rho^2 z^2}} + \underbrace{\frac{4p^2}{z_R^2} z^2}_{T_{z^2}}, \quad (3-30)$$

where  $V_0 = 2\pi n_m R^3 (m^2 - 1) / [c(m^2 + 2)] I_0$  and the term of order  $\mathcal{O}((z/z_R)^4)$  has been neglected since  $(z/z_R)^4 \ll (z/z_R)^2$  for  $z \ll z_R$ . At the plane  $z = 0$  the potential scales with  $\rho^4$ . Therefore, the force scales with  $\rho^3$  and has vanishing first and second derivatives. For  $z \neq 0$ , Eq. (3-30) has a crossed term  $\rho^2 z^2$  that couples motion along the axial and radial directions. Because the scattering force is proportional to the intensity, it also has null derivatives at the equilibrium position and hence vanishes for a particle placed at and near the origin.

Finally, the potential in the  $xz$  plane is displayed in Figures 3.4(c) and



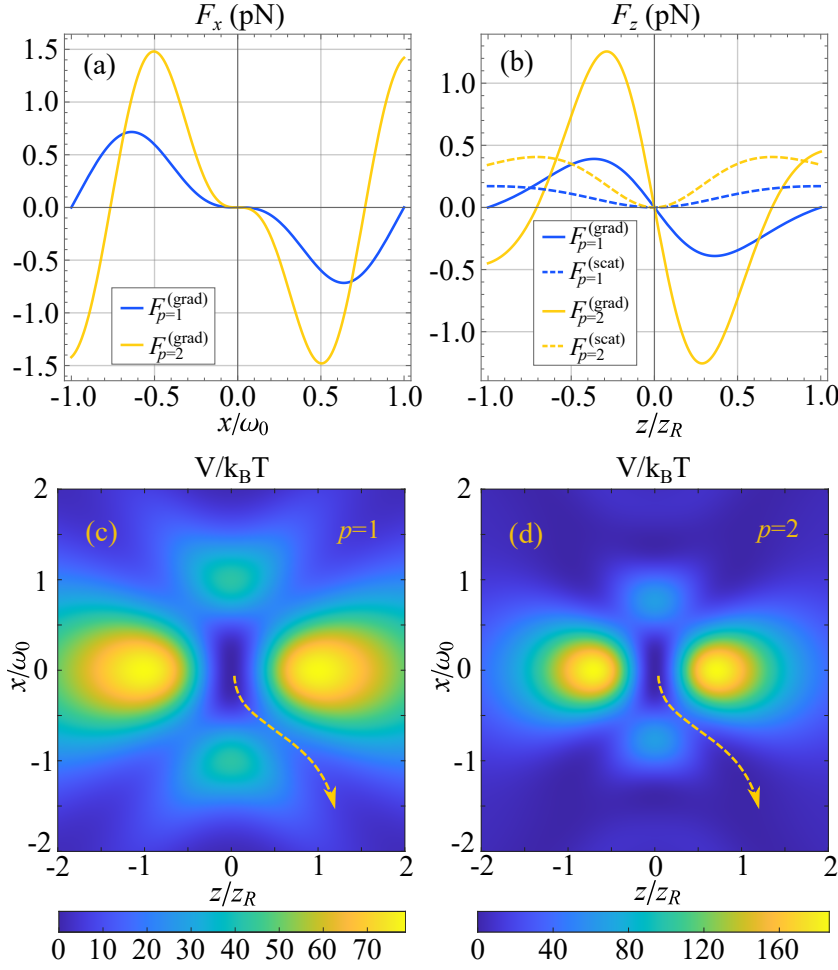


Figure 3.4: Forces acting on a trapped sphere in the (a)  $x$  direction and (b)  $z$  direction for  $p = 1$  and  $p = 2$ . Solid lines are gradient forces, while dashed lines are scattering forces. Potential landscape in the  $xz$  plane for a sphere trapped by a bottle beam with (c)  $p = 1$  and (d)  $p = 2$ . The parameters used for these plots are:  $NA = 0.5$ ,  $R = 70$  nm,  $\lambda_0 = 780$  nm,  $n_m = 1.46$ ,  $n_p = 1.33$ ,  $P_0 = 200$  mW,  $T = 300$  K.

3.4(d) for the cases of  $p = 1$  and  $p = 2$ . As it can be seen, a trapped particle does not need to go through the high intensity peaks along the  $x$  or  $z$  axis in order to escape the trap. Smaller potential barriers have to be climbed if the particle undergoes paths like the yellow dashed ones. We will call the lowest potential energy needed for the particle to leave the trap  $V_{min}$ . Because the potential scales with  $V_0$ , we have  $V_{min} \propto V_0$ .

### 3.4.2 Decoupling approximation

The axial and radial movements can be decoupled if the coupling term in Eq.(3-30) is much smaller than the remaining terms. The conditions under which this assumption holds true can be found by estimating the magnitude

of the particle's displacements under the influence of the trap. Neglecting the cross term and considering thermal equilibrium we may write

$$\langle \rho^4 \rangle = \frac{1}{Z_0} \int d^3\mathbf{r} \rho^4 \exp \left\{ \left[ -\frac{4V_0 p^2}{k_B T} \left( \frac{\rho^4}{\omega_0^4} + \frac{z^2}{z_R^2} \right) \right] \right\} \quad (3-31)$$

$$\langle z^2 \rangle = \frac{1}{Z_0} \int d^3\mathbf{r} z^2 \exp \left\{ \left[ -\frac{4V_0 p^2}{k_B T} \left( \frac{\rho^4}{\omega_0^4} + \frac{z^2}{z_R^2} \right) \right] \right\}, \quad (3-32)$$

where  $k_B$  is the Boltzmann constant,  $T$  is the temperature and  $Z_0$  is given by

$$Z_0 = \int d^3\mathbf{r} \exp \left\{ \left[ -\frac{4V_0 p^2}{k_B T} \left( \frac{\rho^4}{\omega_0^4} + \frac{z^2}{z_R^2} \right) \right] \right\}. \quad (3-33)$$

From Eqs. (3-31)-(3-33) we find that

$$\sqrt[4]{\langle \rho^4 \rangle} = \sqrt[4]{\frac{\omega_0^4 k_B T}{8p^2 V_0}} \quad (3-34)$$

$$\sqrt{\langle z^2 \rangle} = \sqrt{\frac{z_R^2 k_B T}{8p^2 V_0}}. \quad (3-35)$$

Although Eqs. (3-34) and (3-35) were derived by neglecting the cross term, they can be used to estimate the magnitude of the three different terms in Eq. (3-30). Through simple scaling we are led to

$$\frac{T_{\rho^2 z^2}}{T_{\rho^4}} \sim \frac{T_{\rho^2 z^2}}{T_{z^2}} \sim \frac{1+p}{\sqrt{2}p} \left( \frac{V_0}{k_B T} \right)^{-1/2}. \quad (3-36)$$

Because  $V_{min}/k_B T \gg 1$  is required for the particle to be confined in the presence of a thermal bath [119] and  $V_{min} \propto V_0$ , fulfillment of the decoupling condition is associated with increased trap stability.

In the decoupling regime the optical potential becomes

$$V_p(\rho, z) \approx \frac{k_\rho^{(3)}}{4} \rho^4 + \frac{k_z}{2} z^2, \quad (3-37)$$

with the constants  $k_\rho^{(3)}$  and  $k_z$  given by,

$$k_\rho^{(3)} = \frac{64n_m P_0 R^3}{c} \left( \frac{\pi \text{NA}}{\lambda_0} \right)^6 \left( \frac{1-m^2}{2+m^2} \right) p^2 \quad (3-38)$$

$$k_z = \frac{32P_0 R^3 \lambda_0^2}{\pi^2 n_m c} \left( \frac{\pi \text{NA}}{\lambda_0} \right)^6 \left( \frac{1-m^2}{2+m^2} \right) p^2. \quad (3-39)$$

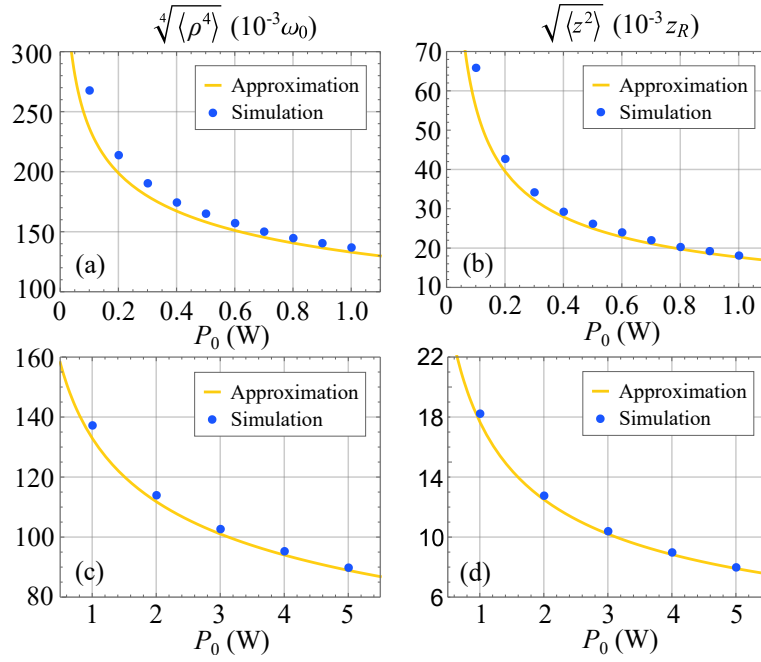


Figure 3.5: Comparison between the values of  $\sqrt[4]{\langle \rho^4 \rangle}$  in (a),(c) and of  $\sqrt{\langle z^2 \rangle}$  in (b),(d) obtained from the approximated potential in Eq.(3-37) and from simulation of the particle's motion subject to the exact potential in Eq.(3-24) for different laser powers. The motion was simulated during 10s with time steps of  $0.5\mu\text{s}$  using  $\text{NA} = 0.5$ ,  $R = 70 \text{ nm}$ ,  $\lambda_0 = 780 \text{ nm}$ ,  $n_m = 1.46$ ,  $n_p = 1.33$ ,  $T = 295 \text{ K}$ ,  $p = 1$ .

### 3.4.3

#### Trapped particle dynamics

To further evaluate the validity of the above estimates and approximations, it is useful to simulate the dynamics of a particle trapped by the potential of a bottle beam in its exact form, calculated from Eqs. (3-10) and (3-24). The equation of motion for a spherical particle under this condition is

$$M\ddot{\mathbf{r}}(t) = -\gamma\dot{\mathbf{r}}(t) - \nabla V(\mathbf{r}(t)) + \sqrt{2\gamma k_B T} \mathbf{W}(t), \quad (3-40)$$

where  $\eta$  is the medium's viscosity,  $\gamma = 6\pi\eta R$  is the drag coefficient and  $M$  is the particle's mass. The environmental fluctuations are modelled using a Gaussian, white and isotropic stochastic process  $\mathbf{W}(t) = (W_x(t), W_y(t), W_z(t))$ , with zero mean and no correlations among different directions. We have that

$$\langle W_i(t)W_i(t') \rangle = \delta(t - t'), \quad (3-41)$$

where  $\delta(t - t')$  is the Dirac delta in the time-domain.

For a sufficiently small particle the inertial term  $M\ddot{\mathbf{r}}$  is negligible in comparison to the viscous term  $\gamma\dot{\mathbf{r}}$ . In this so-called *over-damped* regime we can numerically integrate equation (3-40) using

$$\mathbf{r}(t + \Delta t) = \mathbf{r}(t) - \frac{\nabla V(\mathbf{r}(t))}{\gamma} \Delta t + \sqrt{\frac{2k_B T \Delta t}{\gamma}} \mathbf{eta}(t) \quad (3-42)$$

where  $\mathbf{eta}(t)$  is the Wiener process,  $\Delta t = \tau/n$  is the time interval between iterations,  $\tau$  the total time of simulation and  $n$  the total number of iterations.

Numerical integration of the motion of a water droplet ( $n_p = 1.33$ ,  $R = 70$  nm) trapped in oil ( $n_m = 1.46$ ) by a bottle beam ( $p = 1$ ,  $\lambda = 780$  nm) focused using an objective lens ( $\text{NA} = 0.5$ ) was performed for different trapping powers. Note that the total trapping power is two times larger than the power  $P_0$  of each beam, as discussed in Section 3.1.3.

The motion was simulated for a period of 10 s using time steps of 0.5  $\mu\text{s}$ . This resulted in  $20 \times 10^6$  position values for each trapping power. The values of  $\sqrt[4]{\langle x^4 \rangle}$  and  $\sqrt{\langle z^2 \rangle}$  obtained from this simulation of the exact potential and the curves predicted using the approximated potential in Eq. (3-37) together with Eqs. (3-31) and (3-32) are displayed in Figure 3.5. The largest values of  $\sqrt[4]{\langle x^4 \rangle}/\omega_0$  and  $\sqrt{\langle z^2 \rangle}/z_R$  obtained are approximately 0.27 and 0.067, respectively. This justifies the fourth order approximation leading to Eq. (3-30) for the entire simulated range of trapping powers.

Moreover, we can see from Figure 3.5 that agreement between the simulated dynamics of the exact potential and the approximate potential of Eq. (3-37) increases with  $P_0$ . For  $P_0 > 1$  W, exact and approximate values differ by less than 3%, and hence Eq. (3-37) can be considered a good approximation of the potential. This behavior is consistent with the previous estimate that the ratios  $T_{\rho^2 z^2}/T_{\rho^4}$  and  $T_{\rho^2 z^2}/T_{z^2}$  scale with  $V_0^{-1/2}$ , and hence, the larger the trapping power the smaller the cross term in comparison to the remaining relevant terms.

This can be further verified in Figure 3.6, where we plot the ratios

$$r_1 = \frac{\langle T_{\rho^2 z^2} \rangle}{\langle T_{\rho^4} \rangle}, \quad r_2 = \frac{\langle T_{\rho^2 z^2} \rangle}{\langle T_{z^2} \rangle}, \quad (3-43)$$

obtained from the simulations. The decreasing behavior of  $r_1$  and  $r_2$  with respect to  $P_0$  confirms that increasing the trapping power is an effective way of decoupling the radial and axial directions.

Another consequence of the interplay between a radial quartic and a longitudinal quadratic potential is that elongation of the trap can be adjusted by tuning the laser power. This is illustrated in Figure 3.7, in which the positions of the trapped particle obtained from the numerical simulation are displayed in a scatter plot, for  $P_0 = 100$  mW and  $P_0 = 5$  W. As it can be seen, the trap is appreciably compressed along the  $z$  axis in the latter case, but not in the former. This feature is not present in regular Gaussian tweezers:

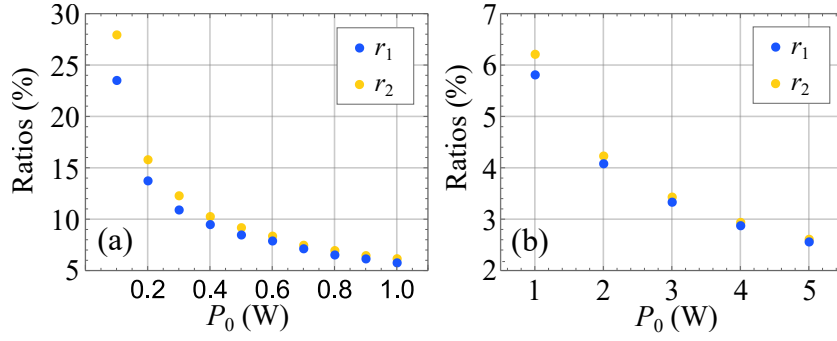


Figure 3.6: Ratios  $r_1 = \langle T_{\rho^2 z^2} \rangle / \langle T_{\rho^4} \rangle$  and  $r_2 = \langle T_{\rho^2 z^2} \rangle / \langle T_{z^2} \rangle$  obtained by simulating the motion of a particle subject to the exact potential in Eq.(3-24) for different laser powers. The motion was simulated during 10s with time steps of  $0.5\mu\text{s}$  using  $\text{NA}=0.5$ ,  $R = 70\text{nm}$ ,  $\lambda_0 = 780\text{nm}$ ,  $n_m = 1.46$ ,  $n_p = 1.33$ ,  $T = 295\text{K}$ .

since the potential is quadratic along the three axis, the expected value of the displacement along all axes scale equally with  $\sqrt{P}$ .

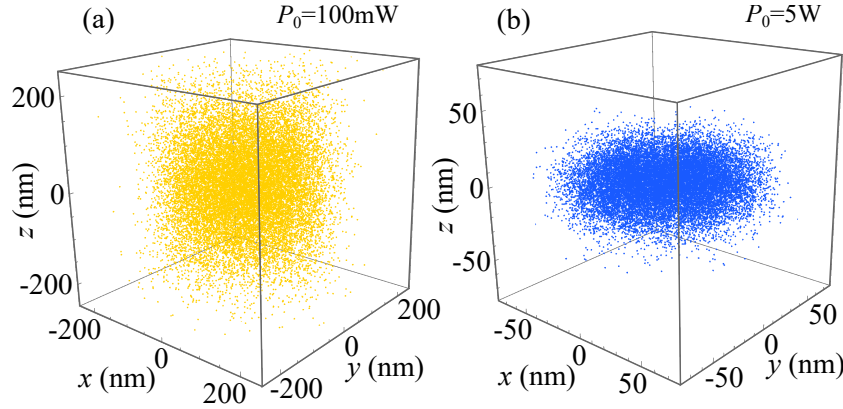


Figure 3.7: Positions of the particle obtained by simulating the motion of a particle trapped by the exact potential in Eq.(3-24) for (a)  $P_0 = 100\text{mW}$  and (b)  $P_0 = 5\text{W}$ . The motion was simulated during 10s with time steps of  $0.5\mu\text{s}$  using  $\text{NA} = 0.5$ ,  $R = 70\text{nm}$ ,  $\lambda_0 = 780\text{nm}$ ,  $n_m = 1.46$ ,  $n_p = 1.33$ ,  $T = 295\text{K}$ ,  $p = 1$ . To allow better visualization, the  $20 \times 10^6$  positions generated by the simulation were divided in 1000 sets, and only the first value of each set is displayed in the figure.

We note that this compression is different from the one caused by an increase in numerical aperture, mentioned previously. In that case we have a compression of the overall shape of the intensity landscape along the  $z$  axis, which happens in the case of a Gaussian beam due to the scaling of  $\omega_0$  with  $\text{NA}^{-1}$  and of  $z_R$  with  $\text{NA}^{-2}$ . In contrast, an increase in the trapping power of a bottle beam compresses the region visited by the particle over time.

In summary, we conclude that in the dipole regime Eq. (3-30) is a good approximation for the optical potential generated by a bottle beam for a wide range of trapping powers, as it only relies on  $\rho^4/\omega_0^4 \ll 1$  and  $z^4/z_R^4 \ll 1$ . On

the other hand, decoupling of the radial and axial motions only occurs for high trapping powers that make the cross term in Eq. (3-30) negligible. This allows approximating the potential by Eq. (3-37). Furthermore, increasing the trapping power causes squashing along the axial direction of the accessible region for a trapped particle.

### 3.4.4

#### Decoupling by addition of an extra mode

High trapping powers are only necessary if one wishes to decouple the radial and axial dependencies of the trapping potential, but when considering power-sensitive samples, such as biological ones, this is not viable. An alternative, valid independent of the trapping power, is to add an extra Laguerre-Gauss mode with  $\ell_2 = 0$  and  $p_2 \neq 0$  to the superposition. Consider the intensity  $I(\rho, z)$  of the following superposition:

$$E(\rho, z) = E_{0,0}^{LG}(\rho, z) + \alpha_1 E_{0,p_1}^{LG}(\rho, z) + \alpha_2 E_{0,p_2}^{LG}(\rho, z). \quad (3-44)$$

We want to obtain a relationship between the complex coefficients  $\alpha_1$  and  $\alpha_2$ , and the radial orders  $p_1$  and  $p_2$  that achieve the desired decoupling and bottle-beam profile. The LG modes with zero OAM are given by

$$E_{0,p}^{LG}(\bar{\rho}, \bar{z}) = \frac{\mathcal{N}}{\sqrt{1+\bar{z}^2}} e^{-\frac{\bar{\rho}^2}{2}} L_p^0(\bar{\rho}^2) \left( \frac{1-i\bar{z}}{\sqrt{1+\bar{z}^2}} \right)^{2p+1} \exp \left[ ikz + ik \frac{\rho^2}{2R(z)} \right],$$

where we defined  $\mathcal{N} = \sqrt{4P_0/c\epsilon\pi\omega_0^2}$ ,  $\bar{\rho} = \sqrt{2}\rho/w(z)$ ,  $\bar{z} = z/z_R$  and the last term is the Gouy phase.

The trapping potential is proportional to the light intensity distribution and, therefore, to the square modulus of the electric field

$$\begin{aligned} I(\bar{\rho}, \bar{z}) &= \frac{I_0}{1+\bar{z}^2} e^{-\bar{\rho}^2} \left| 1 + \alpha_1 L_{p_1}^0(\bar{\rho}^2) \left( \frac{1-i\bar{z}}{\sqrt{1+\bar{z}^2}} \right)^{2p_1} \right. \\ &\quad \left. + \alpha_2 L_{p_2}^0(\bar{\rho}^2) \left( \frac{1-i\bar{z}}{\sqrt{1+\bar{z}^2}} \right)^{2p_2} \right|^2. \end{aligned} \quad (3-45)$$

We seek an approximate expression for the trapping potential around the beam focus, which can be obtained from a power series expansion around this point. The bottle-beam condition requires that the light intensity vanishes at the focus. Note that  $L_p^0(0) = 1$ , so the light intensity at the beam focus is proportional to

$$I(\mathbf{0}) = I_0 |1 + \alpha_1 + \alpha_2|^2, \quad (3-46)$$

which implies

$$|1 + \alpha_1 + \alpha_2|^2 = 0. \quad (3-47)$$

This condition cancels out the zero order contribution to the power series expansion. We will keep terms up to  $\bar{\rho}^4$  and  $\bar{z}^2$ , which are the first non vanishing contributions to the power series. Since the zero order term vanishes, it will be easier to expand first the expression inside the square modulus in Eq. (3-45) and keep terms up to  $\bar{\rho}^2$  and  $\bar{z}^2$ . The following approximations are assumed

$$e^{-\bar{\rho}^2} \approx 1 - \bar{\rho}^2, \quad (3-48)$$

$$L_p^0(\bar{\rho}^2) \approx 1 - p\bar{\rho}^2, \quad (3-49)$$

$$\left( \frac{1 - i\bar{z}}{\sqrt{1 + \bar{z}^2}} \right)^{2p} \approx 1 - 2ip\bar{z} - 2p^2\bar{z}^2. \quad (3-50)$$

$$\frac{1}{1 + \bar{z}^2} \approx 1 - \bar{z}^2 \quad (3-51)$$

Applying the approximations above together with the bottle-beam condition (3-47), we find the following approximate expression for the trapping intensity

$$I(\bar{\rho}, \bar{z}) \approx I_0 \left[ 4|B|^2 \left( \frac{z^2}{z_R^2} + \frac{\rho^4}{w_0^4} \right) - 8[|B|^2 + \text{Re}(AB^*)] \frac{z^2 \rho^2}{z_R^2 w_0^2} \right],$$

where we defined

$$A = \alpha_1 p_1^2 + \alpha_2 p_2^2, \quad (3-52)$$

$$B = \alpha_1 p_1 + \alpha_2 p_2. \quad (3-53)$$

The two-mode bottle-beam potential is recovered by making  $\alpha_1 = -1$  and  $\alpha_2 = 0$ .

Decoupling between the radial ( $\rho$ ) and longitudinal ( $z$ ) dependencies is achieved by choosing  $\alpha_1$  and  $\alpha_2$  such that

$$|B|^2 + \text{Re}(AB^*) = 0 \quad (B \neq 0). \quad (3-54)$$

We can write this condition in terms of the real and imaginary parts of the coefficients  $\alpha_j = a_j + ib_j$ . Including the bottle-beam condition, the following equations must hold

$$1 + a_1 + a_2 = 0, \quad (3-55)$$

$$b_1 + b_2 = 0, \quad (3-56)$$

$$\begin{aligned} & (a_1^2 + b_1^2)(p_1^2 + p_1^3) + (a_2^2 + b_2^2)(p_2^2 + p_2^3) \\ & + p_1 p_2 (p_1 + p_2 + 2)(a_1 a_2 + b_1 b_2) = 0. \end{aligned} \quad (3-57)$$

By using (3-55) and (3-56) in (3-57), we derive the following condition:

$$\begin{aligned} & (a_1^2 + b_1^2) \left[ p_1^2(p_1 + 1) + p_2^2(p_2 + 1) - p_1 p_2(p_1 + p_2 + 2) \right] \\ & + a_1 \left[ 2p_2^2(p_2 + 1) - p_1 p_2(p_1 + p_2 + 2) \right] + p_2^2(p_2 + 1) = 0. \end{aligned} \quad (3-58)$$

For example, let us set  $p_1 = 1$  and  $p_2 = 2$ , giving

$$a_1^2 + b_1^2 + \frac{7}{2}a_1 + 3 = 0 \Rightarrow b_1^2 = -\left(a_1^2 + \frac{7}{2}a_1 + 3\right) \geq 0. \quad (3-59)$$

This condition has infinite solutions in the interval  $-2 \leq a_1 \leq -3/2$ . Its limits provide real solutions for the superposition coefficients:

- $\alpha_1 = -2, \alpha_2 = 1$ .
- $\alpha_1 = -3/2, \alpha_2 = 1/2$ .

Note that the first real solution is useless, since it gives  $B = 0$  and cancels out all terms up to  $\rho^4$  and  $z^2$  in the trapping potential. The other real solution gives  $A = 1/2$  and  $B = -1/2$ , resulting in the following expression for intensity of the electric field

$$I(\rho, z) \approx I_0 \left( \frac{z^2}{z_R^2} + \frac{\rho^4}{w_0^4} \right), \quad (3-60)$$

which provides the desired bottle-beam configuration with decoupled dynamics along the transverse and longitudinal directions. Moreover, we can easily show that this solution is optimal. Under the bottle-beam and decoupling condition, the trapping strength is

$$4|B|^2 = 2a_1 + 4, \quad (3-61)$$

which is a linear function of  $a_1$  with positive slope. Therefore, its maximum value is obtained at the upper limit  $a_1 = -3/2$ , yielding the maximum trap stiffness of the three mode configuration.

### 3.4.5

#### Calibration of the optical trap

In laboratory conditions, quantitative measurements using optical tweezers rely on knowledge of the trap's parameters. In the case of a bottle trap defined by the potential in Eq. (3-37), the relevant parameters are  $k_z$  and  $k_\rho^{(3)}$ . To properly operate the tweezer these must be found by measuring the particle's position during a finite interval of time. This yields a time series



$\mathbf{r}_m(t) = \beta \cdot \mathbf{r}(t)$ , where  $\beta = \text{diag}(\beta_x, \beta_y, \beta_z)$  are conversion factors between position displacements and the measured quantity, such as the voltage in a position sensitive detector. For simplicity, we will assume  $\beta_x = \beta_y = \beta_\rho$ .

For a bottle beam trap the particle's position can be measured using a high speed camera [134], or alternatively by applying a purely Gaussian beam at a different wavelength with respect to the bottle beam. The second beam can be focused onto the trapped particle by the same objective lens used for the bottle, and collected by a second objective lens after separation from the trapping beam by a dichroic mirror. The collected Gaussian light can then be directed onto a Quadrant Photo Detector, where the usual forward scattering measurement is performed [135]. The Gaussian power should be kept significantly weaker than the Bottle power to avoid disturbances due to the presence of this auxiliary Gaussian trap.

In the decoupled regime, movement along the  $z$  axis is independent from movement along the  $x$  and  $y$  axes and the equations of motion can be separated from Eq. (3-40), yielding

$$-\gamma\dot{z}(t) - k_z z(t) + \sqrt{2\gamma k_B T} W_z(t) = 0, \quad (3-62)$$

where once again we assume the inertial term is negligible. The constants  $k_z$  and  $\beta_z$  can be found using the standard procedure of analysing the autocorrelation function [136] or the power spectral density [137, 138] of the measured axial displacements  $z_m(t) = \beta_z z(t)$ .

To find the remaining relevant constants we need two independent equations. Using Eqs.(3-31) and (3-38) we may write

$$\frac{k_\rho^{(3)} \langle \rho^4 \rangle}{4} = \frac{k_B T}{2} \rightarrow \langle \rho^4 \rangle = \frac{2k_B T}{k_\rho^{(3)}}, \quad (3-63)$$

leading to the relation,

$$\langle \rho_m^4 \rangle = \beta_\rho^4 \frac{2k_B T}{k_\rho^{(3)}}. \quad (3-64)$$

A second equation can be obtained from an active method of calibration consisting of moving the sample in which the particle is immersed with a known velocity  $\mathbf{v}_{drag}$  [139, 140]. This will cause a constant drag force  $\gamma \mathbf{v}_{drag}$  on the particle, and taking  $\mathbf{v}_{drag} = v_{drag} \hat{\mathbf{x}}$  the equation of motion along the  $x$  axis becomes

$$\gamma v_{drag} - \gamma \dot{x}(t) - k_\rho^{(3)} x(t) \rho(t)^2 + W_x(t) = 0. \quad (3-65)$$

After a transient time the particle reaches an equilibrium position displaced with respect to the trap's center, with  $\langle \dot{x}(t) \rangle = 0$ . Taking the time average of Eq.(3-65) leads to

$$\gamma v_{drag} - k_\rho^{(3)} \langle x(t) \rho(t)^2 \rangle = 0, \quad (3-66)$$

which can then be used to obtain the relation

$$\langle x_m(t)\rho_m(t)^2 \rangle = \beta_\rho^3 \frac{\gamma v_{drag}}{k_\rho^{(3)}}. \quad (3-67)$$

Eqs.(3-64) and (3-67) together with the standard autocorrelation procedure for the axial motion enables the measurement of the four parameters  $\beta_\rho, \beta_z, k_\rho^{(3)}$  and  $k_z$  in the decoupled approximation.

### 3.4.6

#### Optical forces from a bottle beam in the Intermediate Regime

We move our discussion on the trapping capability of the optical bottle beam for particles in the intermediary regime, whose dimension are of the order of the wavelength of the trapping beam, as discussed in Section 3.2.2. Optical forces generated by the superposition of a Gaussian beam and a Laguerre-Gauss beam with  $\ell = 0, p \neq 0$  are obtained with the aid of [123, 141]. For simplicity, we focus on the  $p = 1$  case and a particle of refractive index  $n_p = 1.33$  trapped by a 500 mW beam at  $\lambda_0 = 780$  nm immersed in oil of refractive index  $n_m = 1.46$ .

Figure 3.8 shows the plots of  $F_z(z)$  and  $F_x(x)$  divided by the particle's mass for four different NA's and four different particle radii. The force in the  $z$  direction is evaluated for  $x = y = 0$ , while  $F_x(x)$  is evaluated at  $y = 0, z = z_{eq}$ , where  $z_{eq}$  is the equilibrium coordinate along the  $z$  direction, i.e.,

$$\begin{cases} F_z(z_{eq}) = 0 \\ dF_z(z)/dz|_{z=z_{eq}} < 0 \end{cases} \quad (3-68)$$

When no equilibrium position exists,  $F_x(x)$  is evaluated at  $z = 0$ .

Some general trends can be extracted from Figure 3.8. First, we note that if the sphere is small ( $R = \lambda_0/4$ ) and the numerical aperture is low ( $\text{NA} = 0.3, 0.5$ ), the force in the  $x$  direction resembles the one calculated using the dipole approximation, i.e., it appears to scale with  $x^3$  around the origin. As  $R$  or NA increases, this cubic dependence starts to vanish, giving place to a linear dependence.

We can also notice that the size of the particle and the numerical aperture play an important role on the existence of an equilibrium position in the axial direction, with large radius  $R$  and large NA being detrimental to the trap stability along the  $z$  axis. For  $\text{NA} = 0.7$ , for instance, there is an equilibrium position if  $R = \lambda_0/4$  or  $R = \lambda_0/2$ , but not if  $R$  is larger. For a fixed  $R = \lambda_0$ ,  $z_{eq}$  doesn't exist for  $\text{NA} > 0.5$ . This is rather different from what happens in the regular Gaussian trap, in which increasing the NA is associated with an increase in trap stability [119].

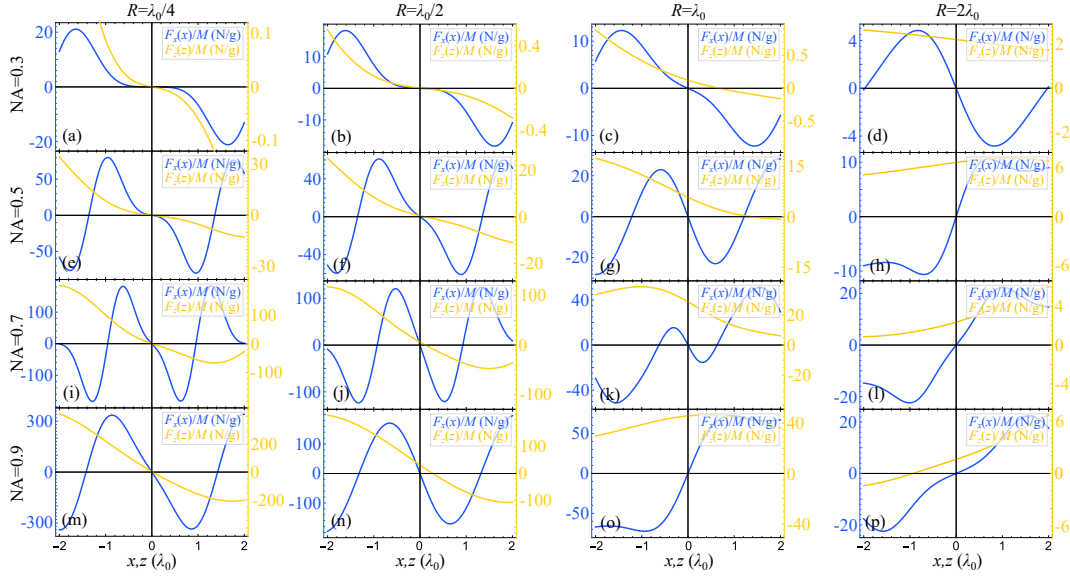


Figure 3.8: Optical forces acting on a particle trapped by a bottle beam in the intermediate regime ( $R \approx \lambda$ ). The force in the axial direction ( $F_z(z)$ ) is calculated for  $x = y = 0$ , while the force in the radial direction ( $F_x(x)$ ) is calculated for  $y = 0$  and  $z = z_{eq}$ . If no axial equilibrium position is found,  $F_x(x)$  is evaluated at  $z = 0$ . The particle's radius is constant within each column, while the numerical aperture is constant within each line. The forces are normalized by the particle's mass, other parameters used in simulation are:  $n_p = 1.33$ ,  $n_m = 1.46$ ,  $\lambda_0 = 780$  nm,  $P = 500$  mW, density of the particle =  $10^3$  kg/m<sup>3</sup>,  $p = 1$ .

### 3.4.7

#### Limitations of trapping in a dark focus

The trends observed in Figure 3.8 can be understood qualitatively by recalling that a bottle beam is a dark region surrounded by a finite bright light boundary. If the particle is small enough it will fit inside the dark region and will be repelled by the boundary. In contrast, if the particle is too big it does not fit inside the bottle and the dark focus becomes irrelevant, with the beam effectively pushing the particle away.

This can be seen for in Figures 3.8(e)-(h): the dimensions of the bottle when  $NA = 0.5$  are  $W = 0.99$   $\mu\text{m}$  and  $H = 2.9$   $\mu\text{m}$ . Therefore, a particle of diameter  $0.5\lambda$  fits entirely inside the bottle and is free within the dark region, causing the force in the  $x$  direction to have vanishing derivative near the origin. When  $R = \lambda_0$ , the particle no longer fits in the dark focus, and the influence of light gives a linear scaling to  $F_x(x)$  around the equilibrium position. When  $R = 2\lambda_0$  the particle has an increased overlap with the light intensity and no longer encounter an equilibrium position.

Similarly, an increase in numerical aperture causes the dark focus to

shrink. When the bottle becomes too small to comprise the particle the situation in the third column of Figure 3.8 is reached and the forces eventually turns into non-restorative ones.

This qualitative reasoning is confirmed in Figure 3.9, in which the equilibrium position  $z_{eq}$  and the derivative along the  $x$  direction near the equilibrium position are displayed as a function of the particle's radius and the numerical aperture. Two main regions can be identified in each of the plots. The first of them, is the region for which  $z_{eq}$  was not found in the range of inspected axial coordinates  $-6\lambda_0 < z < 6\lambda_0$ . In this region, the derivative along the  $x$  axis was not evaluated. The remaining areas are the ones in which an axial equilibrium position exists.

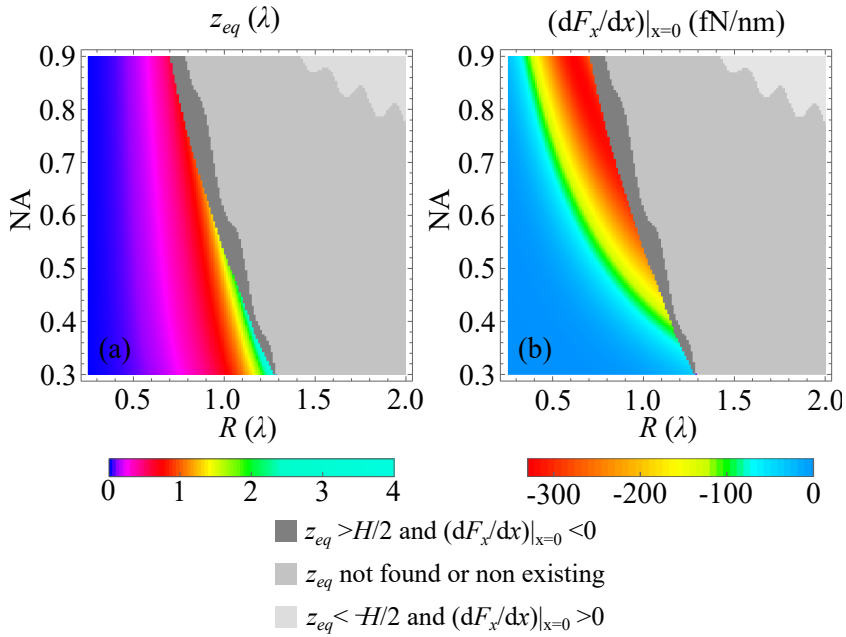


Figure 3.9: Intermediate regime simulations for different values of NA and  $R$ : (a) Axial equilibrium coordinate and (b) first derivative of the force in the radial direction. Medium gray: no equilibrium position was found in the inspected range ( $-6\lambda_0 < z < 6\lambda_0$ ). Light (dark) gray: an equilibrium position was found outside the bottle, at  $z_{eq} < -H/2$  ( $z_{eq} > H/2$ ) and the force is non-restorative (restorative) along the radial direction. The regions in different colors are the ones in which trapping inside the bottle is possible. The parameters used in the simulation were  $\lambda_0 = 780$  nm,  $P = 500$  mW,  $n_m = 1.46$ ,  $n_p = 1.33$ ,  $p = 1$ .

Because we wish to trap the particle in the dark focus, we need to avoid equilibrium situations as the ones described in [142] in the context of vortex beams, in which the scattering force is balanced by the repelling gradient force before the focus. To exclude trapping positions outside the bottle, the regions in which  $z_{eq} > H/2$  were displayed in dark grey and the regions in which  $z_{eq} < -H/2$  were displayed in light grey. In the latter case, the derivative of

the radial force was found to be positive and hence non-restorative, while in the former this derivative was found to be negative. The coloured region, then, is the region for which stable trapping inside the bottle is possible.

We can then conclude that for a given  $R$ , there is a maximum numerical aperture that can be used to form a stable trap. Conversely, for a given NA, there is a limit on the size of the particles that can be trapped. Figure 3.10(a) shows how this limit varies for different refractive indices of the medium and a fixed  $N = 0.5$ . The curves were chopped when  $z_{eq}$  became larger than  $H/2$ , and we can clearly see that the closer the refractive index gets to that of the particle, the larger the radius of the particle that can be trapped. Figure 3.10 confirms that the radial force is restorative for the entire range of  $R$  and  $n_m$  we considered. It also shows that while decreasing  $n_m$  can help trapping larger particles, it also diminishes the force experienced by the particle, and hence plays an important role in the trap's stability.

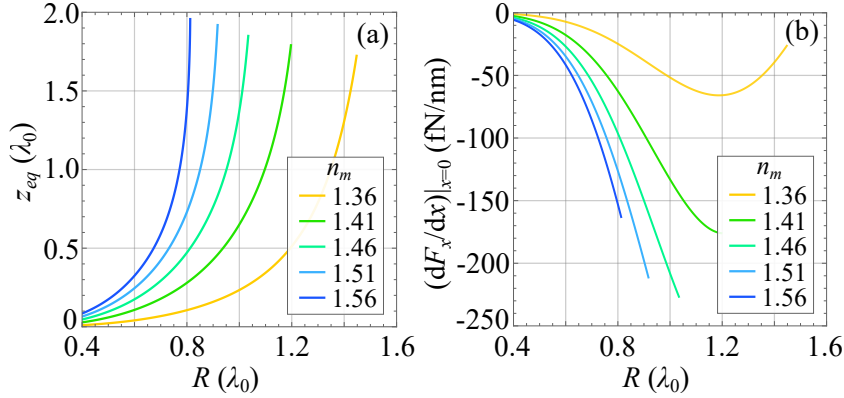


Figure 3.10: Intermediate regime simulations for different values  $n_m$ : (a) Axial equilibrium coordinate and (b) first derivative of the force in the radial direction as a function of particle's radius. Points for which  $z_{eq} > H/2$  are not displayed. The parameters used in the simulation were  $\lambda_0 = 780$  nm,  $P = 500$  mW,  $n_m = 1.46$ ,  $n_p = 1.33$ ,  $p = 1$ .

### 3.4.8

#### Trapping living organisms in the dark

The bottle beam trap finds promising applications in biology. For instance it has been reported that organelles with a refractive index lower than its surroundings are repelled from standard Gaussian optical tweezers [143]. The bottle beam could then be used to manipulate such organelles within a cell.

Similarly, a dark optical trap could also be employed to trap living organisms without excessive laser damage onto the cell by appropriate choice of a surrounding medium. Iodixanol has been reported as a non-toxic medium

for different organisms, with high water solubility, in which the refractive index can be linearly tuned in the visible to near-IR range from  $\sim 1.33$  to  $\sim 1.40$  by changing concentration [144]. Assuming a mean refractive index for a living cell to be within the range  $\sim 1.36$  to  $\sim 1.39$  [145,146] it is expected that stable trapping in a dark focus can be attained.

Table 3.1: Proposed values for trapping a Mycoplasma cell using a bottle beam.

Parameter	Units	Value
Particle refractive index $n_p$	-	1.36-1.39
Medium refractive index $n_m$	-	1.40
Particle radius $R$	$\mu\text{m}$	0.3
Laser wavelength $\lambda_0$	nm	1064
Numerical aperture NA	-	0.7
Laser power	mW	500
Index $p$	-	1

Mycoplasma are known to be among the smallest living organisms, and perhaps the simplest cells [147]. With radii around  $\sim 0.3 \mu\text{m}$ , these organisms lack a cell wall [148], being protected from the surrounding environment solely by their cellular membrane. This may present interesting mechanical and elastic properties which could be probed with the bottle beam. We propose investigating the trapping of Mycoplasma cells immersed in a non-toxic mixture of refractive index 1.40. Iodixanol presents a possible such medium, but further empirical tests must be carried over to fully determine how it affects living Mycoplasma cells. Figure 3.11 shows the simulated forces acting on a trapped Mycoplasma when the parameters shown in Table 3.1 are used. As it can be seen, forces along radial and axial directions are restorative and should provide stable trapping inside the bottle.

It is known that direct incidence of focused laser light onto living cells can affect their division and growth [143]. As an interesting application of the bottle beam one could observe the process of cell division without directly sending a focused beam onto the trapped particle. The following experiment could be performed: at each round of measurement, a cell undergoing division is trapped in the dark focus by a given laser power and the complete cycle of the division process is observed. A trapped dividing cell will occupy an increasing volume and unavoidably encounter the boundary of the dark region, where the trapping beam will impose a pressure against the volume expansion. By increasing the laser power used in each round, one can look for the threshold power for which cell division is precluded. With the proper tweezer calibration presented in the previous section, the threshold power provides information on

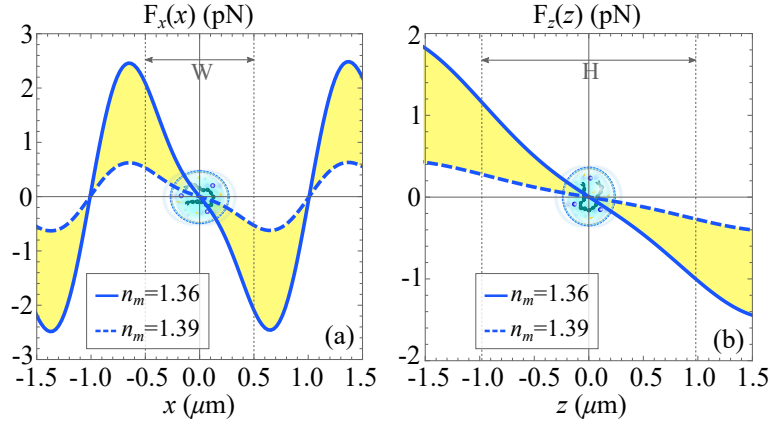


Figure 3.11: Forces acting on a trapped Mycoplasma cell, shown here centered at the origin for size comparison, (a) along the  $x$  direction as a function of radial displacement and (b) along the  $z$  direction as a function of axial displacement. The solid and the dashed curves correspond to a medium's refractive index of 1.36 and 1.39, respectively, while the yellow area correspond to  $1.36 \leq n_m \leq 1.39$ . The other parameters used in the simulation are displayed in Table 3.1.

the forces acting during the process of cell division.

As for the trapping beam, we note that the desired superposition can be created using a SLM, a versatile tool for shaping arbitrary amplitude and phase distributions without the need for combining aligned multiple beams. For the purpose of the present work, controlled preparation of a desired superposition of Laguerre-Gaussian modes can be efficiently implemented, as recently demonstrated in [114]. For the moderate NA of 0.7 - much smaller than the usual value of 1.3 used when trapping particles in liquid media - we don't expect aberrations to pose a serious challenge for optical trapping with the bottle beam.

### 3.5 Conclusions

We studied the fundamental modes that describe laser beams, LG modes, from which any optical beam's spatial profile can be decomposed as a superposition. From them, we were able to build a mathematical description of an optical bottle beam, a beam of light with a high-intensity boundary surrounding a dark focus, generated by the superposition of a Gaussian beam and a Laguerre-Gauss beam with  $\ell = 0$  and  $p \neq 0$ .

We have theoretically analysed the optical forces a highly-focused light beam performs on a linear dielectric particle, for both the dipole and intermediate regimes. For the case of a particle with higher refractive index than its surrounding medium, in the dipole approximation, we have show that a Gaus-

sian beam can effectively 3D trap a silica nanosphere in water if it is close to the beam focus.

When considering a particle of lower refractive index than its surrounding medium, we envisioned the dark focus of a bottle beam to be able to also act as a trapping potential. Because the size of trapped particles commonly range from tens of nanometers [128] to several microns [129], here, we analysed the optical forces acting on particles much smaller than and with dimensions comparable to the wavelength of the trapping beam.

In the case of small particles, the dipole approximation was applied, resulting in a number of distinguishing features of the investigated trap. Scattering was found to be null at the focus of the beam, eliminating imbalance between gradient and scattering forces [133]. The optical potential, on the other hand, coupled the motion along the radial and axial directions. It was shown that these could be decoupled by using a sufficiently high trapping power. The approximated decoupled potential turns out to be quartic and quadratic in the radial and axial directions, respectively. To test the validity of the approximated potential, motion of a particle trapped by the exact potential in a viscous medium was simulated and the results were confronted with those expected from the approximation as a function of laser power. We have also shown that by superposing a third mode, motion along the axial and radial directions can be decoupled independently of the trap power. To guide future experimental realizations, a calibration method was proposed.

In the case of larger objects, for which the dipole approximation is not valid, the tools developed in [123,141] were used to calculate the optical forces. Equilibrium positions after the focus were found, indicating a trapping regime different from the one described in [142]. The interplay between the numerical aperture and the sphere's radius were explored and led to the conclusion that there is an upper bound for both of these quantities when using bottle beams for optical trapping. These limitations were interpreted in terms of the size of the optical bottle in comparison to the size of the particle, and were found to be eased by choosing a medium with refractive index close to that of the particle.

Finally, the findings obtained through exploration of the intermediate regime led to an experimental proposal to trap a living organism using the bottle beam. Considering values of refractive index reported in the literature, it is expected that trapping of small cells such as the *Mycoplasma* immersed in a non toxic high-refractive index medium in a dark focus is within reach. This could be applied to situations in which focusing a high laser power onto the scrutinized cell is detrimental [132], as in the case of cellular division [143].



As a final remark, we note that the present analysis could be applied to other types of bottle beams and structured beams in general. This would be specially interesting for applications dealing with micron-sized objects, since many works deal only with the case of Rayleigh particles [100–102, 105, 109]. Additionally, it would be interesting to explore how the dark focus affect the transfer of angular momentum between trapping beam and trapped particle when a superposition of circularly polarized beams or beams possessing angular momentum is used.

## 4

### Dispersive Optomechanics

Any interaction between light and a mechanical object that alters the momentum of the former will give rise to a radiation pressure force acting on the latter, e.g., the gradient and scattering forces studied in Chapter 3. When considering optical cavities, such interactions can couple its optical field with nano- and micromechanical degrees of freedom, giving rise to non-trivial dynamics for a plethora of different optomechanical systems. The field of quantum optomechanics studies such interaction and serves as a resourceful platform for quantum technologies given its ability to generate nonclassical states of both light [149, 150] and matter [151–154], perform quantum control over matter [15–18, 47, 155], and realize precision force and displacement measurements [10, 65, 83, 156].

In the following sections, we will study three physical scenarios where radiation pressure interaction emerges, which are mathematically equivalent, in the sense that their unitary dynamics is governed by the same dispersive Hamiltonian. A derivation of the unitary time evolution operator this Hamiltonian entails will be carried out and we will show that it can generate quantum correlations between both light and matter, following our work [157].

#### 4.1

##### Dispersive Hamiltonian

##### 4.1.1

###### Fabry-Pérot cavity with movable end mirror

First, we consider the simplest optomechanical system: a Fabry-Pérot cavity with bare cavity length  $L$ , bare resonant frequency  $\omega_c = \pi c/L$  and perfect end mirrors. We let one of the mirrors of mass  $m$  to be movable, performing a harmonic motion with natural frequency  $\omega_m$ , as schematically depicted in Figure 4.1. We assume that the cavity was previously populated by an external laser, see Section 5.2.1.1 for more details.

In the following, we present an phenomenological derivation of this system's Hamiltonian [158]. The formal demonstration, first performed by C. K. Law, can be found at Ref. [159].

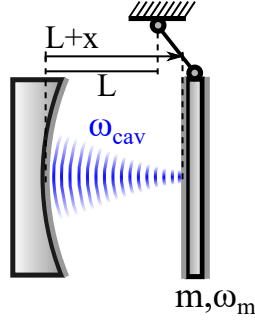


Figure 4.1: Schematic representation of an optical cavity with a movable extremity following harmonic motion.

As both the optical and mechanical modes are modelled as quantum harmonic oscillators, their Hamiltonian read

$$\hat{H} = \hbar\omega_{\text{cav}}(\hat{x})\hat{a}^\dagger\hat{a} + \hbar\omega_m\hat{b}^\dagger\hat{b}, \quad (4-1)$$

where  $\hat{a}$  ( $\hat{a}^\dagger$ ) and  $\hat{b}$  ( $\hat{b}^\dagger$ ) are the annihilation (creation) operators of the optical and mechanical modes, respectively. Note that the optical frequency in this case,  $\omega_{\text{cav}}(\hat{x})$ , is dependent on the movable mirror position, as it naturally alters the cavity length, and it is given by

$$\omega_{\text{cav}}(x) = \frac{\pi c}{(L+x)}, \quad (4-2)$$

Although this Hamiltonian exactly describes the dynamics of the system, its analytical treatment is arduous. Therefore, we only consider small amplitudes for the movement of this mirror, such that we can approximate the cavity frequency through a series expansion around its equilibrium position

$$\omega_{\text{cav}}(x) \approx \omega_c - \frac{\omega_c}{L}x + \frac{\omega_c}{L^2}x^2 + \mathcal{O}(x^3). \quad (4-3)$$

In the following, we will only keep up to linear terms in this expansion. Therefore, the Hamiltonian simplifies to

$$\frac{\hat{H}}{\hbar} \approx (\omega_c - G\hat{x})\hat{a}^\dagger\hat{a} + \omega_m\hat{b}^\dagger\hat{b} \quad (4-4)$$

where  $G \equiv \omega_c/L$ . A special remark should be made at this point in order to be no confusion in the future: the sign of the interaction reflects our choice of coordinate system, when  $x > 0$ , the movable mirror is increasing the cavity length and conversely decreasing the cavity frequency. If we had defined our coordinate axis reversed, or considered the leftmost mirror to be movable, then the sign of the interaction would also reverse.

Moreover, it is usual in the literature to expand the position operator in terms of the mechanical annihilation and creation operators:  $\hat{x} = x_{\text{ZPF}}(\hat{b}^\dagger + \hat{b})$ , where  $x_{\text{ZPF}} = \sqrt{\hbar/(2m\omega_m)}$  is the zero point fluctuation of the moving mirror, in order to rewrite the Hamiltonian as

$$\frac{\hat{H}}{\hbar} \approx \omega_c \hat{a}^\dagger \hat{a} + \omega_m \hat{b}^\dagger \hat{b} - g_{0,\text{mirror}} \hat{a}^\dagger \hat{a} (\hat{b}^\dagger + \hat{b}) \quad (4-5)$$

where  $g_{0,\text{mirror}} \equiv Gx_{\text{ZPF}}$  is the single photon coupling strength, with units of frequency, and every operator present in the Hamiltonian is now dimensionless.

It is straightforward to notice that this Hamiltonian gives rise to a radiation pressure force if we write the Heisenberg equations of motions for the mirror's position operator  $\hat{x}$  and momentum operator  $\hat{p} = i \sqrt{\hbar m \omega_m / 2} (\hat{b}^\dagger - \hat{b})$ :

$$\dot{\hat{x}} = +\omega_m \hat{p}, \quad (4-6)$$

$$\dot{\hat{p}} = -\omega_m \hat{x} + G \hat{a}^\dagger \hat{a}. \quad (4-7)$$

The first term on the right hand side (RHS) of both equations together define the harmonic motion of the mirror and the second term in the second line is effectively a force acting on the mirror, proportional to the number of photons inside the cavity. Thus, one example of the so-called radiation pressure force. As a matter of fact, in a closed system dynamics, the number operator for the optical mode commutes with the full Hamiltonian and, thus, remains constant as time passes, making this a constant force. One should note that if the system is allowed to follow a open quantum dynamics, this is no longer true.

#### 4.1.2

##### Levitated nanoparticle inside an optical cavity

Consider now the system shown in Figure 4.2: a nanoparticle of radius  $r$ , mass  $m$  and refractive index  $n_p$  is trapped in a harmonic trap of frequencies  $\omega_{j=x,y,z}$  created by an optical tweezer inside a cavity populated by a single optical mode of frequency  $\omega_a$  and annihilation/creation operators  $\hat{a}/\hat{a}^\dagger$ , respectively. At this moment, we will not derive the Hamiltonian for this system, as an analogous proof will be carried out in Section 5.1. Here we present the main result: if the optical tweezer is finely tuned with the cavity, the presence of the particle causes a position dependent shift on the cavity's resonance frequencies, so that the Hamiltonian of this system becomes [46]

$$\frac{\hat{H}}{\hbar} = \omega_a \hat{a}^\dagger \hat{a} + \sum_{\substack{j= \\ x,y,z}} \omega_j \hat{b}_j^\dagger \hat{b}_j - U_{0,a} \sin^2[k_a(x_0 + \hat{x})] \hat{a}^\dagger \hat{a}, \quad (4-8)$$

where  $x_0$  is the position of the center of the trap,  $\hat{x}$  is the particle's displacement,  $U_{0,a} = \omega \hat{a} \alpha / (2\epsilon_0 V_a)$  is the frequency shift when the particle is at an intensity maximum of the cavity,  $\alpha = 4\pi\epsilon_0 r^3 (n_p^2 - 1) / (n_p^2 + 2)$  is the polariz-

ability of the particle,  $V_a$  and  $k_a$  are the volume and the wavenumber of the optical mode, respectively, and  $\hat{b}_j/\hat{b}_j^\dagger$  is the phonon annihilation/creation operators along axis  $j = x, y, z$ . As before, we do not consider an external driving laser and assume that the optical cavity was previously populated.

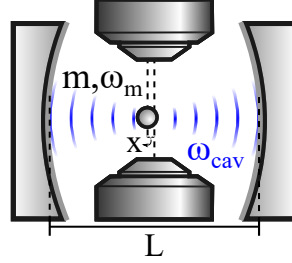


Figure 4.2: A nanoparticle, trapped by an optical tweezer, is placed along the axis of a cavity populated by a single optical mode of frequency  $\omega_a$ . If the position  $x_0$  of the center of the optical trap is properly chosen, the coupling between particle and light becomes linear on the particle's displacement.

The interaction terms may yield linear coupling between the optical mode and the sphere if  $x_0$  and  $k_a$  are properly chosen. Once again, considering small amplitude motion, we can expand  $\sin^2 k_a(x_0 + \hat{x})$  around  $x_0$  such that

$$\sin^2[k_a(x_0 + \hat{x})] = \sin^2(k_a x_0) + k_a \sin(2k_a x_0)x + 2k_a^2 \cos(2k_a x_0)x^2 + \mathcal{O}(x^3). \quad (4-9)$$

Now, consider the particular case in which the length of the optical cavity is  $L = 2n(\lambda_a/2)$ . Then, if the sphere is placed near the center of the cavity at  $x_0 = L/2 + \lambda_a/8$ , we have

$$\sin^2 k_a(x_0 + \hat{x}) \approx \frac{1}{2} + k_a \hat{x}. \quad (4-10)$$

Substituting these approximations in equation (4-8) and disregarding the motion along the  $y$  and  $z$  axes, we get

$$\hat{H}/\hbar = \omega'_a \hat{a}^\dagger \hat{a} + \omega_x \hat{b}_x^\dagger \hat{b}_x - g_{0,\text{levitated}} \hat{a}^\dagger \hat{a} (\hat{b}_x^\dagger + \hat{b}_x), \quad (4-11)$$

where  $\omega'_a = \omega_a - U_{0,a}/2$  and  $g_{0,\text{levitated}} = U_{0,a} k_a x_{\text{ZPF}}$  is the intended linear coupling strength.

### 4.1.3

#### Ultracold atom cloud trapped inside optical cavity

In ultracold atom optomechanical experiments, an atomic ensemble is trapped inside an optical cavity. The effective Hamiltonian describing the interaction between  $N$  atoms with a single cavity optical mode is the Tavis-Cummings Hamiltonian [160, 161]. However, in the appropriate regime [161], the collective center-of-mass motion of the atoms acts similarly to the dispersive optomechanical experiments with levitated spheres described in the previ-

ous section, with the cloud of atoms playing the role of levitated nanoparticle altering the cavity resonance frequency. Accordingly, the Hamiltonian describing the collective center of mass motion of the atomic cloud is, once again, the dispersive Hamiltonian

The optomechanical coupling strength between an ultracold atomic cloud and a cavity optical mode with wavelength  $\lambda_a$  is [162]

$$g_{0,\text{atoms}} = k_a N \frac{\alpha_0^2}{\Delta_{ca}} \sin(2k_a z_0) \sqrt{\frac{\hbar}{2Nm\omega_m}}, \quad (4-12)$$

where  $k_a$  is the wavenumber,  $N$  is the number of atoms,  $\Delta_{ca}$  is the atom-cavity detuning,  $m$  is the mass of a single atom,  $\omega_m$  is the mechanical frequency and  $\alpha_0 = \sqrt{d^2\omega_c/(2\hbar\epsilon_0 V_c)}$  is the atom-single photon coupling rate, with  $d$  the dipole moment for the transition between the relevant atomic levels and  $V_c$  the cavity mode volume.

## 4.2

### Unitary quantum dynamic

Once the dispersive Hamiltonian is found, we are able to calculate the corresponding time evolution operator  $\hat{U}(t) = \exp(-\frac{i}{\hbar}\hat{H}t)$  that dictates the unitary quantum dynamics of the optomechanical system. Here we will use the following notation for the Hamiltonian

$$\frac{\hat{H}}{\hbar} = \omega_m \hat{b}^\dagger \hat{b} + \omega_c \hat{a}^\dagger \hat{a} - g_0 \hat{a}^\dagger \hat{a} (\hat{b} + \hat{b}^\dagger), \quad (4-13)$$

where  $\hat{a}$  and  $\hat{b}$  ( $\hat{a}^\dagger$  and  $\hat{b}^\dagger$ ) denote annihilation (creation) operators for the optical mode and the mechanical oscillator, respectively. In what follows we will work with the re-scaled time  $\tau \equiv \omega_m t$ , and introduce the dimensionless variables  $r_a = \omega_a/\omega_m$  and  $k = g_0/\omega_m$ .

First, we define the unitary operator [151]

$$\hat{E}(k) = \exp(k \hat{a}^\dagger \hat{a} (\hat{b}^\dagger - \hat{b})). \quad (4-14)$$

The operator  $\hat{E}(k)$  commutes with  $\hat{a}^\dagger \hat{a}$ , but not with  $\hat{b}$ , such that

$$\hat{E}(k)^\dagger \hat{b} \hat{E}(k) = \hat{b} + k \hat{a}^\dagger \hat{a}, \quad (4-15)$$

which is calculated through the general identity,

$$e^{-\hat{A}} \hat{B} e^{+\hat{A}} = \hat{B} + [\hat{B}, \hat{A}] + \frac{1}{2!} [[\hat{B}, \hat{A}], \hat{A}] + \dots \quad (4-16)$$

Using equation (4-15) and its adjoint, we have

$$\hat{E}(k)^\dagger \frac{\hat{H}}{\hbar \omega_m} \hat{E}(k) = \hat{b}^\dagger \hat{b} + r_a \hat{a}^\dagger \hat{a} - k^2 (\hat{a}^\dagger \hat{a})^2. \quad (4-17)$$

Considering the number basis  $\{|n, m\rangle\}$ , we see by the equation above that  $\hat{E}(k)|n, m\rangle$  are the energy eigenstates of the system. Given the form of the operator  $\hat{E}(k)$ , Equation (4-14), those are of the form:

$$\hat{E}(k)|n, m\rangle = \hat{\mathcal{D}}_m(k)n|n, m\rangle, \quad (4-18)$$

where we denote the displacement operator of the mechanical oscillator by  $\hat{\mathcal{D}}_m(\kappa) = \exp(\kappa\hat{c}^\dagger - \kappa^*\hat{c})$ , where  $\kappa$  is a complex number, see Appendix B. The energies corresponding to the eigenstates above are

$$E_{n,m} = \hbar\omega_m m + \hbar\omega_a n - \hbar\omega_m k^2 n^2. \quad (4-19)$$

By exponentiation of equation (4 – 17), the unitary evolution operator is found to be

$$\hat{U}(\tau) = \hat{E}(k) e^{-i(\hat{b}^\dagger \hat{b} + r_a \hat{a}^\dagger \hat{a} - k^2 (\hat{a}^\dagger \hat{a})^2)\tau} \hat{E}(k)^\dagger. \quad (4-20)$$

Next, we recall that  $e^{i\hat{b}^\dagger \hat{b}\tau} \hat{b}^\dagger e^{-i\hat{b}^\dagger \hat{b}\tau} = e^{i\tau} \hat{b}^\dagger$  and  $e^{i\hat{b}^\dagger \hat{b}\tau} \hat{b} e^{-i\hat{b}^\dagger \hat{b}\tau} = e^{-i\tau} \hat{b}$ , from which we derive the following identity

$$e^{i\hat{b}^\dagger \hat{b}\tau} \hat{A}(\hat{b}^\dagger - \hat{b}) e^{-i\hat{b}^\dagger \hat{b}\tau} = \hat{A}(e^{i\tau} \hat{b}^\dagger - e^{-i\tau} \hat{b}) \quad (4-21)$$

$$\Rightarrow e^{i\hat{b}^\dagger \hat{b}\tau} e^{\hat{A}(\hat{b}^\dagger - \hat{b})} e^{-i\hat{b}^\dagger \hat{b}\tau} = e^{\hat{A}(e^{i\tau} \hat{b}^\dagger - e^{-i\tau} \hat{b})}, \quad (4-22)$$

where  $\hat{A}$  is any operator that commutes with both  $\hat{b}$  and  $\hat{b}^\dagger$ . Letting  $\hat{A} = k \hat{a}^\dagger \hat{a}$  in the identity above, we conclude that

$$\begin{aligned} \hat{E}(k) e^{-i\hat{b}^\dagger \hat{b}\tau} &= e^{-i\hat{b}^\dagger \hat{b}\tau} e^{i\hat{b}^\dagger \hat{b}\tau} \hat{E}(k) e^{-i\hat{b}^\dagger \hat{b}\tau} \\ &= e^{-i\hat{b}^\dagger \hat{b}\tau} \exp\left(k \hat{a}^\dagger \hat{a} (\hat{b}^\dagger e^{i\tau} - \hat{b} e^{-i\tau})\right), \end{aligned} \quad (4-23)$$

hence

$$\hat{E}(k) e^{-i\hat{b}^\dagger \hat{b}\tau} \hat{E}(k)^\dagger = e^{-i\hat{b}^\dagger \hat{b}\tau} \times \exp\left(k \hat{a}^\dagger \hat{a} (\hat{b}^\dagger e^{i\tau} - \hat{b} e^{-i\tau})\right) \times \exp\left(-k \hat{a}^\dagger \hat{a} (\hat{b}^\dagger - \hat{b})\right). \quad (4-24)$$

From the commutator

$$\frac{1}{2}[\hat{b}^\dagger e^{i\tau} - \hat{b} e^{-i\tau}, \hat{b}^\dagger - \hat{b}] = i \sin(\tau), \quad (4-25)$$

it becomes straightforward to compute

$$[k \hat{a}^\dagger \hat{a} (\hat{b}^\dagger e^{i\tau} - \hat{b} e^{-i\tau}), k \hat{a}^\dagger \hat{a} (\hat{b}^\dagger - \hat{b})] = 2ik^2 (\hat{a}^\dagger \hat{a})^2 \sin(\tau). \quad (4-26)$$

Since this commutes with both  $\hat{a}^\dagger \hat{a} (\hat{b}^\dagger e^{i\tau} - \hat{b} e^{-i\tau})$  and  $\hat{a}^\dagger \hat{a} (\hat{b}^\dagger - \hat{b})$ , equation (4 – 24) can be simplified using the particular form of the Baker-Campbell-Hausdorff formula

$$e^{\hat{A}} e^{\hat{B}} = e^{\hat{A} + \hat{B} + \frac{1}{2}[\hat{A}, \hat{B}]}, \quad (4-27)$$

valid when operators  $\hat{A}$  and  $\hat{B}$  commute with  $[\hat{A}, \hat{B}]$ . Thus, the expression,

$$\hat{U}(\tau) = e^{-i\hat{b}^\dagger \hat{b} \tau} e^{-ir_a \hat{a}^\dagger \hat{a} \tau} e^{k \hat{a}^\dagger \hat{a} (\hat{b} \eta(\tau) - \hat{b}^\dagger \eta(\tau)^*)} e^{-i(\hat{a}^\dagger \hat{a})^2 B(\tau)} \quad (4-28)$$

holds for the unitary evolution operator  $\hat{U}(t)$ , where  $\eta(t) = 1 - e^{-it}$  and  $B(t) = -k^2(t - \sin(t))$ .

Now that we have an amenable analytical formula for the time evolution operator arising from a radiation pressure interaction, we are able to study the closed quantum dynamics dictating the optomechanical systems presented in the previous Section and analogous ones, once the proper auxiliar unitary operator  $\hat{E}$  is found.

### 4.3

#### Entanglement dynamics in dispersive optomechanics

In this Section, we present the results obtained in our work [157]. There, we studied entanglement dynamics in dispersive optomechanical systems, analogous systems to the ones studied in Section 4.1, consisting of two optical cavity field modes interacting with a mechanical oscillator. In these systems, the two optical modes interact with the mechanical object, but not directly with each other. Thus, the appearance of optical entanglement witnesses nonclassicality of the oscillator as shown in [163]. We studied the dependence of the optical entanglement dynamics with the optomechanical coupling, the mean photon number in the cavity and the oscillator temperature, and proposed an experimental realization with ultracold atomic ensembles.

#### 4.3.1

##### Introduction

Entanglement is one of the most striking phenomena of quantum theory [164]. Generating, manipulating and measuring entanglement in systems with many constituents and with a large number of degrees of freedom is one of the challenges of quantum information and metrology [165], and an interesting frontier in fundamental physics [166]. In particular, entangling massive objects could open the way to interesting tests of quantum theory [167, 168] and experiments aimed at probing gravitational effects of quantum mechanical matter [169–174]. Optomechanical systems provide a resourceful platform to this end.

It is well known that entanglement of massive objects can be realized in quantum cavity optomechanical experiments [23]. For instance, a cavity with a moving end mirror can be used to generate entangled “cat states” of both light [149, 150] and matter [151–154]. Similar systems have also been proposed as an effective nonlinear medium [29, 175, 176] and squeezing [24–26] as well as



optical entanglement [30] have been experimentally demonstrated in a variety of set-ups such as cavity cold atomic ensembles [162], dispersive dielectric membranes [44] and silicon micro-resonators [177]. In the linearized regime, particularly, entanglement dynamics [68, 178] and stationary entanglement [32, 36, 179, 180] have attracted much attention as these systems have a wide applicability ranging from precision force measurements [35, 36] to quantum networks [31, 37].

Certifying quantumness of optomechanical systems, however, is a far-from-obvious task. Relations among entanglement and nonclassicality measures of quantum states can be used to probe the quantum nature of inaccessible objects such as a harmonic oscillator in an optical cavity [181]. Recurrence of optical squeezing in a cavity with a moving mirror has also been proposed as a witness of nonclassicality [182] and it has been shown that when two subsystems locally interact with a third one, but not directly with each other, the appearance of entanglement among those subsystems is sufficient to prove nonclassicality of the third party [163]. Building on some of these ideas, the present Section studies the entanglement dynamics of a dispersive optomechanical system, how to use that dynamics to probe the quantum nature of the oscillator through optical degrees of freedom and how to optimize the generated optical entanglement by careful choice of the optomechanical coupling and the number of photons in an experiment.

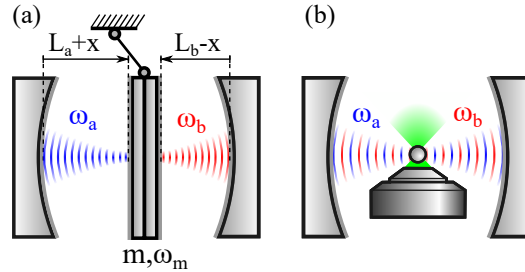


Figure 4.3: (a) Schematics of coupled optical cavities sharing a “mirror-in-the-middle” under a harmonic potential. No photon transfer from one cavity to the other is allowed. (b) Schematics of a particle trapped by an optical tweezer coupled to two modes of a cavity. The particle can be considered as a Silica nano-sphere or a cloud of ultracold atoms. When the levitated object is properly positioned, the Hamiltonian describing both systems acquires the same form.

Considering as possible implementations levitated optomechanical systems, such as Silica nano-spheres or cold atomic ensembles, and a “two-sided” cavity with a moving mirror in the middle, we map how entanglement appears and evolves among the various optical and mechanical subsystems for different optomechanical coupling strengths and optical field intensities. The appear-

ance of mechanically induced optical entanglement and its subsequent death and revival are generic in these systems, and thus could be used to probe the quantization of the center-of-mass of the moving object in real experiments. We also point out in a simplified context that under certain circumstances entanglement seems to “flow” through different subsystems, and such dynamics can be used to infer nonclassicality and entanglement among different components of the system. We consider examples of both non-Gaussian and Gaussian initial quantum states, for which we study the dynamics of concurrence and the Duan criteria [183], respectively. An experiment using levitated cold atomic ensembles is proposed.

### 4.3.2

#### Hamiltonian description

The system we are primarily interested in is shown in Figure 4.3(a): two optical cavities, of lengths  $L_a$  and  $L_b$ , are populated by modes of frequencies  $\omega_a$  and  $\omega_b$  and share a common perfect movable mirror of mass  $m$  subject to a harmonic potential of frequency  $\omega_m$ . We refer to this as the “mirror-in-the-middle” configuration, which is analogous to the optomechanical setup studied in Section 4.1.1. In this system the optical modes never interact directly, except via the dispersive coupling due to the presence of the mechanical mode.

Since we are interested in studying entanglement dynamics in optomechanics, we shall assume cavities can be initialized in particular states, the laser driving-term can be turned off during the course of the experiment and that optical losses are negligible during the time of the experiment, i.e., the same assumptions made in Section 4.1.1 for the single cavity case. A discussion of the conditions under which this is true and the experimental feasibility is addressed in Section 4.3.5.

Generalizing the dispersive Hamiltonian in Equation (4-5) to account for an additional optical mode, we get

$$\frac{H}{\hbar} = \omega_a \hat{a}^\dagger \hat{a} + \omega_b \hat{b}^\dagger \hat{b} + \omega_m \hat{c}^\dagger \hat{c} - g_{0,a} \hat{a}^\dagger \hat{a} (\hat{c}^\dagger + \hat{c}) + g_{0,b} \hat{b}^\dagger \hat{b} (\hat{c}^\dagger + \hat{c}), \quad (4-29)$$

where  $g_{0,i} = \omega_i x_{\text{ZPF}}/L_i$  are the optomechanical couplings, with  $x_{\text{ZPF}} = \sqrt{\hbar/(2m\omega_m)}$  the zero point fluctuation of the mirror and  $\hat{a}$ ,  $\hat{b}$ ,  $\hat{c}$  ( $\hat{a}^\dagger$ ,  $\hat{b}^\dagger$ ,  $\hat{c}^\dagger$ ) are the annihilation (creation) operators of each optical and mechanical modes, denoted by  $A$ ,  $B$  and  $C$ , respectively. As we have seen before, such Hamiltonian can also be implemented using a cavity with a levitated nano-particle [14, 46, 184] or an ultracold atom cloud [162, 185, 186] properly positioned along the cavity axis. This is illustrated in Figure 4.3(b).

Assuming equal frequencies for the optical modes  $\omega_a = \omega_b$ , and approximately equal cavity lengths  $L_a \sim L_b$  we may simplify the notation and directly write  $g_0 \equiv g_{0,a} \sim g_{0,b}$ . Following the procedure outlined in Section 4.2 now with the operator  $\hat{E}(k) = \exp(k(\hat{a}^\dagger \hat{a} - \hat{b}^\dagger \hat{b})(\hat{c}^\dagger - \hat{c}))$ , we are able to find the unitary evolution operator resulting from equation (4-29)

$$\hat{U}(t) = e^{-i\hat{c}^\dagger \hat{c} t} e^{-ir_a \hat{a}^\dagger \hat{a} t} e^{-ir_b \hat{b}^\dagger \hat{b} t} e^{k(\hat{a}^\dagger \hat{a} - \hat{b}^\dagger \hat{b})(\hat{c}^\dagger \eta(t) - \hat{c} \eta(t)^*)} e^{-i(\hat{a}^\dagger \hat{a} - \hat{b}^\dagger \hat{b})^2 B(t)}, \quad (4-30)$$

where we define the dimensionless optomechanical coupling  $k = g_0/\omega_m$ , the “normalized frequencies”  $r_i = \omega_i/\omega_m$ , the scaled time  $\omega_m t \rightarrow t$ , and the functions  $\eta(t) = 1 - e^{-it}$  and  $B(t) = -k^2(t - \sin t)$ . Note the evolution operator is comprised of a *Kerr-like* term, responsible for an effective optical non-linearity [187], as well as an *optically-driven* displacement operator acting on the mechanical mode.

It is expected that a generic separable state will evolve into an entangled one by virtue of the unitary evolution (4-30). We note that if an initially separable state gives birth to optical entanglement then there will certainly be its entanglement death. This springs from the fact that when  $B(t) = 2\pi n$ ,  $n \in \mathbb{N}$ , the term in the evolution operator responsible for entangling the optical modes reduces to the identity operator at those times, therefore preserving the separability of the initial state. Analogous arguments show that optomechanical entanglement must also face death when  $\eta(t) = 0$ .

Not every state will evolve to an entangled one, as can be seen by considering the energy eigenstates of the system

$$\hat{\mathcal{D}}_C(k(n_A - m_B)) |n_A, m_B, \ell_C\rangle, \quad (4-31)$$

where  $\{|n_A, m_B, \ell_C\rangle\}$  denotes the number basis and  $\hat{\mathcal{D}}_C(\alpha)$  the displacement operator acting on the mechanical oscillator, mode  $C$ , by a displacement  $\alpha \in \mathbb{C}$ , in close analogy to the eigenstate discovered in Section 4.2.

### 4.3.3 Qubit states

Consider the cavities in Figure 4.3(a) initially populated by the state

$$|\Psi(0)\rangle = \left( \frac{|0\rangle + |1\rangle}{\sqrt{2}} \right) \otimes \left( \frac{|0\rangle + |1\rangle}{\sqrt{2}} \right) \otimes |0\rangle. \quad (4-32)$$

We refer to these as ‘qubit states’ as they are restricted to the vacuum-one-photon subspace. These states can be prepared in quantum optics in an approximate way using photon pair sources and displacement-based detec-

tion [188, 189] or non-linear light-matter interactions in cavity quantum electrodynamics [190, 191]. In levitated quantum electrodynamics [50], it is also possible to couple two qubits to a nano-sphere or rotor according to the interaction Hamiltonian (4-29), with the qubits assuming the role of the optical fields and the levitated object the role of the mirror-in-the-middle. Among the advantages of this type of scheme is the fact that the optomechanical coupling admits a wide tunability, potentially allowing tests of the optomechanical interaction in novel regimes. Moreover, read-out of the “optical” modes can be achieved through standard qubit read-out techniques [192]. The “mirror-in-the-middle” is taken to be in the ground state for simplicity; in the next section we shall consider the effects of a finite temperature oscillator. Notice the initial state is separable and hence the appearance of entanglement between modes  $A$  and  $B$  would evidence the nonclassical nature of mode  $C$  [163].

Here, it is convenient to work in the interaction picture; following Equation (4-30), we evolve states by the unitary operator

$$\hat{U}_{\text{I.P.}}(t) = e^{k(\hat{a}^\dagger \hat{a} - \hat{b}^\dagger \hat{b})(\hat{c}\eta(t) - \hat{c}^\dagger \eta(t)^*)} e^{-i(\hat{a}^\dagger \hat{a} - \hat{b}^\dagger \hat{b})^2 B(t)}. \quad (4-33)$$

Then, time evolution of (4-32) in the interaction picture is explicitly given by

$$|\Psi(t)\rangle = \frac{|00\rangle}{2}|0\rangle + e^{iB(t)} \frac{|01\rangle}{2} \hat{\mathcal{D}}_C(k\xi(t))|0\rangle + e^{iB(t)} \frac{|10\rangle}{2} \hat{\mathcal{D}}_C(-k\xi(t))|0\rangle + \frac{|11\rangle}{2}|0\rangle, \quad (4-34)$$

where  $\xi(t) = e^{it} \eta(t)$ . The evolved state (4-34) exhibits entanglement between modes  $A$  and  $B$ . This can be promptly seen by noticing that coherent states are non-orthogonal and, in the limit of small coupling  $k$ , the state assumes the form  $|\Psi(t)\rangle \simeq |\varphi_{AB}\rangle \otimes |\varphi_C\rangle$ , where

$$|\varphi_{AB}\rangle \simeq \frac{|0\rangle}{2} (|0\rangle + e^{iB(t)} |1\rangle) + e^{iB(t)} \frac{|1\rangle}{2} (|0\rangle + e^{-iB(t)} |1\rangle) \quad (4-35)$$

and  $|\varphi_C\rangle \simeq |0\rangle$ . For times  $t$  such that  $|B(t)| \simeq \pi/2 + 2\pi n, n \in \mathbb{N}$ , the state  $|\varphi_{AB}\rangle$  becomes maximally entangled. The origin of this entanglement can be heuristically explained by a simple argument: the ground state of the mechanical oscillator is a Gaussian wave packet in the position basis. Each possible position adds-up coherently introducing correlations in the lengths of the left and right cavities in Figure 4.3(a). This imprints correlations in the phases of the corresponding electromagnetic fields in modes  $A$  and  $B$  giving rise to entanglement. As long as the dimensionless optomechanical coupling  $k$  due to radiation pressure on the middle mirror is sufficiently small, mode  $C$  will be approximately unperturbed and therefore, to a good approximation,

disentangled from  $AB$ . On the other hand, as the coupling strength increases mode  $C$  can become significantly entangled with modes  $A$  and  $B$ ; the question of entanglement among different subsystems as a function of  $k$  will be addressed in the next section.

To quantitatively evaluate the entanglement in (4-34) we calculate the three-partite density matrix  $\rho_{ABC} = |\Psi(t)\rangle\langle\Psi(t)|$ , from which we obtain the reduced state  $\rho_{AB} = \text{Tr}_C(\rho_{ABC})$ :

$$\rho_{AB}(t) = \frac{1}{4} \begin{pmatrix} 1 & e^{C(t)} & e^{C(t)} & 1 \\ e^{C^*(t)} & 1 & e^{-2k^2|\eta(t)|^2} & e^{C^*(t)} \\ e^{C^*(t)} & e^{-2k^2|\eta(t)|^2} & 1 & e^{C^*(t)} \\ 1 & e^{C(t)} & e^{C(t)} & 1 \end{pmatrix} \quad (4-36)$$

with  $C(t) = iB(t) - k^2|\eta(t)|^2/2$ . Notice that for small values of  $k$  the mirror is “weakly entangled” with modes  $A$  and  $B$  and some of the off-diagonal terms of the reduced density matrix acquire exponentials that alternate between periods of decay and periods of growth. This can be seen as an example of a weak form of decoherence and “non-Markovian” evolution for the partitions of the whole system, in which information about the optical modes leak into correlations with the mirror and is later retrieved. The mirror introduces a “memory” in the system [193]. Non-Markovianity springs from the fact that the mirror is part of the system under study and hence its degrees of freedom are under control.

Since the state  $\rho_{AB}(t)$  is restricted to the subspace spanned by  $\{|0\rangle, |1\rangle\}$ , we can use concurrence as a measure of entanglement, as it is an entanglement monotone. It can be obtained from a bipartite density matrix of two qubits  $\rho$  by calculating

$$\mathcal{C}(\rho) = \max(0, \lambda_1 - \lambda_2 - \lambda_3 - \lambda_4) \quad (4-37)$$

where the  $\lambda_i$ 's (in decreasing order) are the square roots of the eigenvalues of

$$W = \rho(\sigma_y \otimes \sigma_y) \rho^*(\sigma_y \otimes \sigma_y) \quad (4-38)$$

where  $\sigma_y$  is a Pauli matrix and  $\rho^*$  is the element-wise complex conjugate of  $\rho$  in the eigenbasis of  $\sigma_z$ .

As an example, plots of the concurrence  $\mathcal{C}_{AB}(t)$  and von Neumann entropy  $S_{AB}(t)$  of  $\rho_{AB}$  are shown in Figure 4.4 for coupling value  $k = 0.5$ . The optical modes exhibit positive concurrence and hence entanglement as a function of time. Moreover, the system exhibits sudden death and birth of

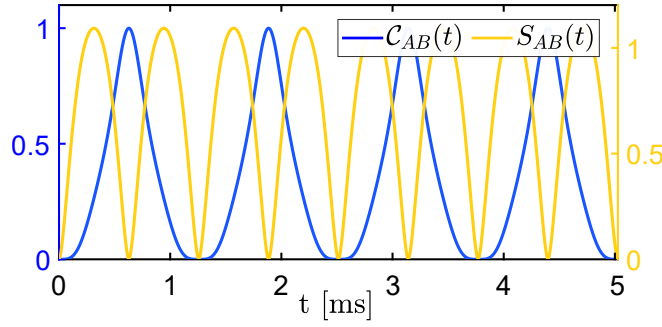


Figure 4.4: Concurrence (blue) and von Neumann entropy (yellow) for  $\rho_{AB}(t)$  as a function of time. For this plot  $k = 0.5$ .

entanglement. It is also possible to see that the entropy, which is initially zero, oscillates as a function of time. This is another indication of the non-Markovian nature of the system. A non-zero entropy of  $AB$  signals entanglement among the three-partite system  $ABC$ . Moreover, note that the maxima of concurrence (entanglement of  $AB$ ) coincide with the minima of entropy (entanglement of  $ABC$ ). This suggests that, after emerging in the system, entanglement “flows” (during the limited period of its lifetime) among different partitions of the system.

#### 4.3.4

##### Continuous Variable states and finite temperature

We now consider a scenario in which initially the optical modes are populated by monochromatic coherent states and the moving object (sphere, cloud of atoms or mirror) is in a thermal state at temperature  $T$

$$\rho(0) = |\alpha\rangle\langle\alpha| \otimes |\beta\rangle\langle\beta| \otimes \frac{1}{Z} \sum_n e^{-\frac{n\hbar\omega_m}{k_B T}} |n\rangle\langle n|, \quad (4-39)$$

where  $Z = \sum_n e^{-\frac{n\hbar\omega_m}{k_B T}}$  is the thermal partition function. Note that although the initial state here considered is Gaussian, the Hamiltonian (4-29) has cubic terms in creation and annihilation operators and, therefore, does not preserve Gaussianity [194]. In order to study the dynamics of entanglement for Continuous Variable states, we turn our attention to the time-dependent Duan Criteria [183], as presented in Appendix B.4. At this moment, we need to lay out some definitions: first, we define the quadratures for each mode ( $j = A, B, C$ )

$$\hat{x}_j = \frac{1}{\sqrt{2}}(\hat{a}_j^\dagger + \hat{a}_j) \quad , \quad \hat{p}_j = \frac{i}{\sqrt{2}}(\hat{a}_j^\dagger - \hat{a}_j) \quad , \quad (4-40)$$

obeying the commutation relations  $[\hat{x}_j, \hat{p}_k] = i\delta_{jk}$ ,  $j, k = A, B, C$ , such that we can define the EPR operators

$$\hat{u}_{jk} = \hat{x}_j + \hat{x}_k, \quad (4-41)$$

$$\hat{v}_{jk} = \hat{p}_j - \hat{p}_k. \quad (4-42)$$

Finally, we define  $D_{ij}$  as an average of the Einstein-Podolski-Rosen (EPR) variance for modes  $i, j$

$$D_{ij} \equiv \frac{1}{2} \left[ (\Delta \hat{u}_{ij})^2 + (\Delta \hat{v}_{ij})^2 \right]. \quad (4-43)$$

The Duan Criteria states that any separable state satisfies

$$D_{ij} \geq 1. \quad (4-44)$$

Therefore, if at any time  $t$  a violation of the above inequality is observed, modes  $i$  and  $j$  are necessarily entangled at that time. As the Duan criteria is written in terms of field quadratures, it can be promptly measured with homodyne detection techniques readily available in the laboratory [195]. We also note that when  $t = 2\pi n/\omega_m$ ,  $n \in \mathbb{N}$ , the unitary evolution (4-30) acts analogous to a  $\chi^{(3)}$  interaction in nonlinear optics [196]. In these moments, the optomechanical system behaves as a nonlinear optical source of squeezing, verified numerically, from which quantum correlations can be readout from the leaking fields of the cavity [197].

Given the time evolution operator in equation (4-30) we are able to find analytical expressions for the EPR variance of every bipartition of the system. For the optical modes we have

$$\begin{aligned} D_{AB}(t) = & 1 + \left[ |\alpha|^2 + 2\alpha\beta \cos((r_a + r_b)t) + |\beta|^2 \right] \\ & - \left[ |\alpha|^2 + 2\alpha\beta \cos((r_a + r_b)t + 2B(t)) + |\beta|^2 \right] \\ & \times e^{-2[|\alpha|^2 + |\beta|^2]} \left[ 1 - \cos(2B(t)) \right] e^{-k^2|\eta(t)|^2 [2\bar{n} + 1]}, \end{aligned} \quad (4-45)$$

where  $\bar{n} = \left[ e^{\hbar\omega_m/(K_B T)} - 1 \right]^{-1}$  is the thermal occupation number for the mechanical oscillator.

Figure 4.5 shows the time evolving EPR variances for different bipartitions of the system:  $AB$  (opto-opto),  $BC$  (opto-mechanical) and  $AC$  (opto-mechanical). We once again observe periodic birth of entanglement and, from the discussion in Section 4.3.2, we can assert that there is death and revivals

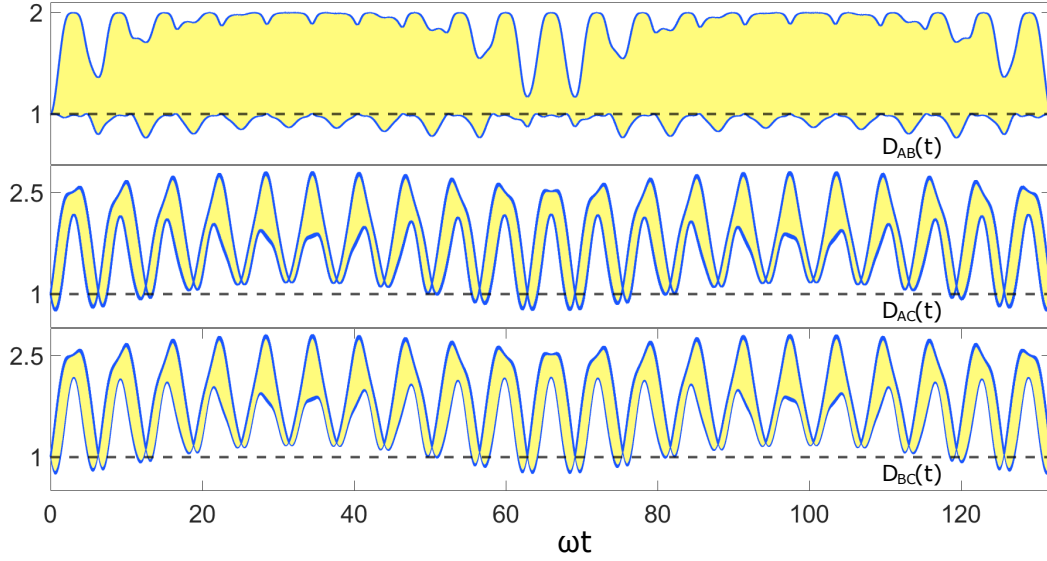


Figure 4.5: Time-dependent EPR variances  $D_{ij}(t)$  (yellow) for the various bipartitions of the system, with its envelope (blue) and threshold for the Duan Criteria (black dashed line). We use  $\omega_a = \omega_b \simeq 2\pi \cdot 1.59 \times 10^{14}$  Hz and the remaining parameters as in Table 4.3.

of entanglement for every bipartition of the system. Moreover, as in the qubit case, the appearance of entanglement between optical modes given the initially separable state can be used in experiments to probe the nonclassicality of the mechanical mode [163]. Although the analytical formulas for the EPR variance are rather involved, it is possible to obtain insight into the entanglement dynamics by looking into their periodicity.

For typical optical and mechanical frequencies, the term  $\cos((r_a + r_b)t)$  represents fast oscillations that do not contribute significantly to the overall envelope of the EPR variances. Consequently, when  $k \ll 1/\sqrt{2}$ , equation (4-45) is dominated by the term  $\exp\left\{-2[|\alpha|^2 + |\beta|^2][1 - \cos(2B(t))]\right\}$  which has a period of  $\tau = \pi/k^2$ . We call this the “low coupling” regime. On the other hand, if  $k \gg 1/\sqrt{2}$  the variance is dominated by the term  $\exp\left\{-k^2|\eta(t)|^2[2\bar{n} + 1]\right\}$ , of period  $\tau = 2\pi$ . We refer to this as the “high coupling” regime. The periodicity of these functions dictates the overall periodicity of the envelope of the EPR variances. We now move back to non-scaled time we make the substitution  $\tau \rightarrow \tau/\omega_m$ . Then, for values in the low coupling regime, observation of EPR variance revivals are only possible when  $\pi/\omega_m k^2 \ll \kappa^{-1}$ , where  $\kappa^{-1}$  is the inverse cavity linewidth, or the approximate photon lifetime in the cavity. This translates into the so-called photon blockade condition  $g_0^2/(\omega_m \kappa) \gg 1$  [185, 198]. For the high coupling regime, observation of full entanglement dynamics is conditioned on satisfying  $2\pi/\omega_m \ll \kappa^{-1}$ , which translates into the resolved-sideband regime  $\omega_m \gg \kappa$  [199].



Knowledge of the behavior of the EPR variance as a function of optomechanical coupling and temperature is useful when designing an experiment. We observe that the optical entanglement in modes  $AB$  is strongly affected by the dimensionless coupling  $k$  in a non-trivial way. Figure 4.6(a) shows the minimum of the EPR variance for the optical modes within the photon lifetime  $\kappa^{-1}$  inside the cavity as a function of coupling  $k$  and oscillator initial temperature  $T$ . In the low coupling regime, where  $k \ll 1/\sqrt{2}$ , above a threshold coupling of  $k \approx 0.1$ ,  $\min(D_{AB}(t))$  generally falls below one and hence the system always exhibits entanglement. In contrast, the Duan criteria is very sensitive to  $k$  in the high coupling regime  $k \gg 1/\sqrt{2}$ , presenting  $\min(D_{AB}(t)) \geq 1$  in the vicinity of  $2k^2 = N$ , where  $N$  is a positive integer. Under this condition the criteria becomes greater than 1 and no entanglement can be certified regardless of the oscillator temperature. An immediate implication is that as  $k$  grows, the separation between inconclusive regions becomes smaller. At high coupling values, small uncertainties in the coupling can then place the system in a parameter region in which the Duan criteria is inconclusive, presenting challenges to an experiment. Therefore, increasing coupling may not be the best strategy for an experiment aimed at verifying optical entanglement.

Moreover we observe that entanglement persists well above the microkelvin temperatures reported in current optomechanical experiments [15, 55, 56, 162], consistent with the theoretical results for the linearized regime in [34]. Conversely, from our numerical calculations, we have observed that although the minimum value of  $D_{AB}(t)$  remains well below 1, the time spent below this threshold becomes increasingly smaller as the temperature grows higher, making it effectively harder to experimentally verify entanglement with the Duan Criteria at micro-kelvin temperatures.

The mean number of photons in the cavity also plays an important role in optical entanglement generation. Figure 4.6(b) shows a surface plot of  $\min(D_{AB}(t))$  within the photon lifetime as a function of the coherent state amplitudes  $\alpha$  and  $\beta$ , taken to be real numbers for simplicity. The Duan Criteria can only be conclusive when the energy is approximately evenly distributed among the two optical modes, which happens when  $\alpha \sim \beta$ . For the parameters used, the optimal coherent amplitudes that minimizes  $D_{AB}(t)$  are found to be  $\alpha \sim \beta \sim 0.91$ .

### 4.3.5

#### Experimental proposal

With increasing advances in the field of quantum cavity optomechanics [15, 55, 56], experiments in the high coupling and long coherence time regimes

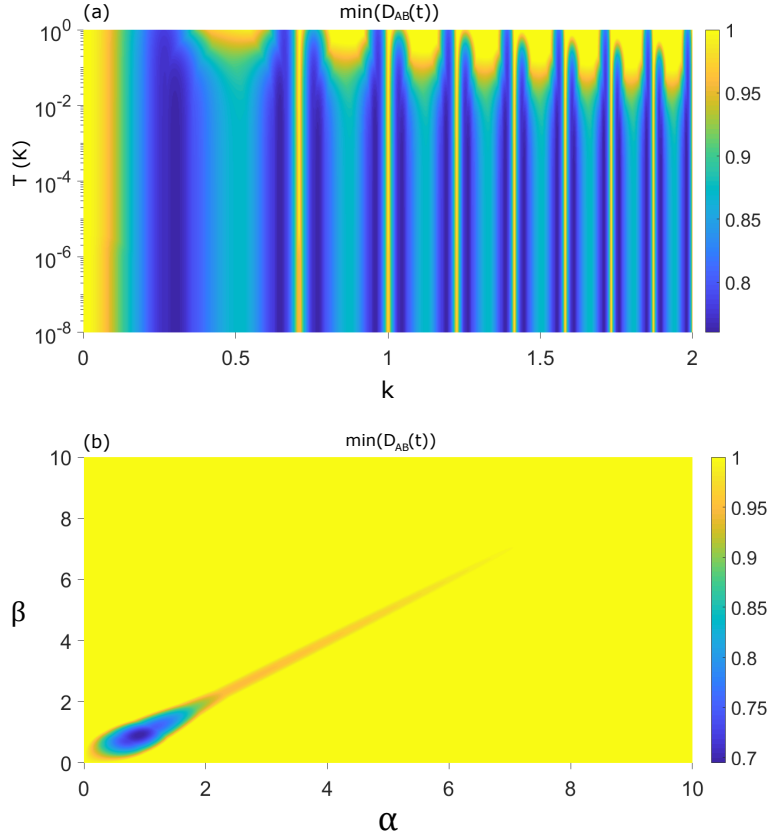


Figure 4.6: **(a)** Minimum value of  $D_{AB}(t)$  within the photon lifetime inside the cavity,  $\tau = \kappa^{-1} \sim 15.6 \mu s$ , as a function of **(a)** dimensionless coupling  $k$  and mechanical oscillator's temperature  $T$ , and **(b)** coherent state amplitudes of  $\alpha$  and  $\beta$ . The optimal coherent amplitudes that globally minimizes the Duan criteria are found to be  $\alpha \sim \beta \sim 0.91$ . We use  $\omega_a = \omega_b \simeq 2\pi \cdot 1.59 \times 10^{14}$  Hz and every other parameter as in in Table 4.3.

are expected, although observing entanglement as described in the present work remains challenging. One notable exception and a promising candidate is optomechanics with ultracold atomic ensembles, where a coherent cloud of atoms is trapped within an optical cavity by a standing wave (trap beam) and the collective center of mass coordinate effectively behaves as a quantum mechanical oscillator which can be monitored by a second optical mode (probe beam). Couplings as high as  $k \approx 10$  have been reported in such ultracold experiments [162], and the system allows wide tunability of the relevant parameters.

We remind that the optomechanical coupling between an ultracold atomic cloud and a cavity optical mode is given in Equation (4-12) and, in Table 4.1, we present the reported values from Ref. [162] for the experimental quantities needed to determine it. We chose  $\sin(2k_a z_0) = 1$  and the wavelength  $\lambda_b$ , for the optical mode  $B$ , should be chosen so that  $\sin(2k_b z_0) = -1$ , as to provide  $g_{0,a} = g_{0,b}$ .

Table 4.1: Values reported in [162].

Parameter	Units	Value
Number of atoms	-	$10^5$
Trap frequency $\omega_m$	kHz	$2\pi \times 40$
Coupling $k = \frac{g_0}{\omega_m}$	-	9.50
Cavity Finesse $\mathcal{F}$	-	$5.8 \times 10^5$
Cavity Length $L$	$\mu\text{m}$	194
Cavity mirror's radius $R$	cm	5
Cavity Linewidth $\kappa$	MHz	$2\pi \times 0.66$
Temperature $T$	$\mu\text{K}$	0.8

For the entanglement dynamics experiment to be feasible, the photon-lifetime  $\tau_p$  must be greater than the entanglement period  $\tau_e$ . One of the main constraints in fulfilling this condition is set by the Finesse of the cavity. Therefore, we look for the minimum value of  $\tau_e/\tau_p$  by varying the cavity length  $L$ , the number of atoms  $N$  and the mechanical frequency  $\omega_m$  around the values in Table 4.1, and then calculate the minimum Finesse necessary to make  $\tau_e/\tau_p < 1$  given the optimal values of  $L$ ,  $N$  and  $\omega_m$ .

In doing these calculations, it is necessary to account for the changes in the mode volume, given by  $V_c = \pi w_a^2 L$ , where

$$w_a = \sqrt{\frac{\lambda_a}{2\pi}} \sqrt{L(2R - L)} \quad (4-46)$$

is the mode's waist, and the changes in the cavity linewidth

$$\kappa = \frac{\mathcal{F}}{\nu_{FSR}} \quad (4-47)$$

with  $\nu_{FSR} = c/2L$  the cavity's free spectral range. Finally, it is important to make sure that  $k = g_0/\omega_m \neq \sqrt{n/2}$ ,  $n$  a positive integer, when the Duan Criteria is inconclusive. We find that for  $L = 783 \mu\text{m}$ ,  $N = 5.43 \times 10^5$  and  $\omega_m = 2\pi \times 95 \text{ kHz} \approx 2\pi \times 95.49 \text{ kHz}$  the dimensionless optomechanical coupling is  $k = 0.743$  and the entanglement period to photon lifetime ratio is  $\tau_e/\tau_p = 3.46$ . The Finesse should then be increased to  $2.01 \times 10^6$ , so that  $\tau_e/\tau_p \simeq 1$  and entanglement becomes measurable. The proposed Finesse is about 1.5 times larger, so that  $\tau_e/\tau_p = 0.669$ .

Another parameter that could be varied are the radii of the cavity mirrors. Considering 1 cm, 2.5 cm, 5 cm and 10 cm as possible radii, we find the values presented in Table 4.2. As we can see, the Finesse constraint can be relaxed provided that a smaller radius is used. Overall, the necessary values for  $N$ ,  $\omega_m$  and  $\mathcal{F}$  differ by less than one order of magnitude from reported values in the literature.

Table 4.2: Optimal parameters for different cavity mirror's radii.

R(cm)	$L(\mu\text{m})$	$N(10^5)$	$\omega_m(\text{kHz})$	$\mathcal{F}(10^6)$
1	1211	3.85	$2\pi \times 95$	1.30
2.5	1035	5.64	$2\pi \times 92$	1.57
5	783	5.43	$2\pi \times 95$	2.01
10	669	5.80	$2\pi \times 91$	2.47

Therefore, in order to observe entanglement dynamics, we propose the parameters presented in Table 4.3. With these values the resulting photon lifetime is  $\tau_p = 15.7 \times 10^{-6}$  s and within this lifetime the minimum value for the optical EPR variance is found to be  $D_{AB}(t) \approx 0.8$ . This suggests that in these systems the observation of mechanically-induced optical entanglement can be within reach.

Table 4.3: Proposed values for the experimental implementation with ultracold atoms.

Parameter	Units	Value
Number of atoms $N$	-	$5.43 \times 10^5$
Trap frequency $\omega_m/2\pi$	kHz	95.49
Coupling $k = \frac{g_0}{\omega_m}$	-	0.74
Mechanical dissipation $\Gamma/2\pi$	kHz	1
Cavity Finesse $\mathcal{F}$	-	$3 \times 10^6$
Cavity Length $L$	$\mu\text{m}$	783
Cavity Linewidth $\kappa/2\pi$	kHz	10.19
Temperature $T$	$\mu\text{K}$	0.8
Mean photon number $ \alpha ^2 =  \beta ^2$	-	0.25

Once  $D_{AB}(t) < 1$ , predicted by equation (4-30) and shown in Figure 4.5, the optomechanical interaction can be switched off by acting on the trap beam and moving the oscillator with respect to the nodes of the probe beam. Quantum correlations can then be readout from the leaking probe field of the cavity by using homodyne detection techniques [197, 200].

Moreover, following [162] where the motion of an ultracold gas of  $^{87}\text{Rb}$  was studied, we estimate the maximal heating rate of a cloud of atoms due to backaction from each optical mode,  $R_c = Ng_0^2/(4\Gamma\kappa)R_{\text{fs}}$ , and due to spontaneous emission,  $R_{\text{fs}} = \hbar^2 k_p^2 g_0^2 \bar{n}_{\text{cav}} \Gamma / (m \Delta_{\text{ca}}^2)$ , where  $k_p \simeq 2\pi/780 \text{ nm}^{-1}$  is the probe wave vector,  $m \simeq 1.44 \times 10^{-25} \text{ kg}$  is the atomic mass of  $^{87}\text{Rb}$ ,  $\bar{n}_{\text{cav}}$  is the mean photon number for each optical mode and  $\Delta_{\text{ca}}/(2\pi) \simeq 209.16 \text{ GHz}$  is the detuning between the frequencies for the optical modes and the atomic resonance frequency. Given the proposed parameters, heating is dominated by the backaction heating rate,  $R_{\text{fs}} \ll R_c \simeq 5.98 \times 10^{-32} \text{ J/s}$ . We note that when compared to the phonon energy, the maximal heating rate is much smaller than

phonon and photon loss decoherence rates,  $R_c/(\hbar\omega_m) \simeq 9.45 \times 10^{-4} \text{ Hz} \ll \kappa, \Gamma$ . Therefore, reheating of the mechanical oscillator should play a negligible role during the course of the experiment.

#### 4.4

#### Conclusions

In this Chapter, we have seen how the so-called radiation pressure interaction arises in three different optomechanical setups following the same Hamiltonian. We also discovered the corresponding unitary time evolution operator describing the closed dynamics of these systems. This allowed us to study the entanglement dynamics of a “mirror-in-the-middle” optomechanical system, where two optical modes interact dispersively with a single mechanical mode.

We have seen that an initially separable quantum state can evolve to an entangled one, exhibiting birth, death and revivals of entanglement and entropy for qubit and continuous variable states; moreover, the appearance of entanglement in this setting evidences the nonclassical nature of the mechanical oscillator. Therefore, optical entanglement will arise if and only if the mechanical oscillator is quantum mechanical.

The entanglement dynamics is strongly influenced by the system parameters, notably the dimensionless optomechanical coupling  $k = g_0/\omega_m$  and the mean number of photons in the experiment. We have shown the existence of two distinct regimes depending on whether  $k < 1/\sqrt{2}$  or  $k \geq 1/\sqrt{2}$ . In addition, we have observed that optical entanglement is maximized when the energy is evenly distributed in the optical modes and that it persists at microkelvin temperatures of the mechanical mode. These are valuable informations when designing an experiment. Optomechanics with ultracold atomic ensembles presents an interesting candidate for implementing the studied entanglement dynamics.

Although a promising candidate, the dispersive Hamiltonian is not the only available platform to untangle the dynamics of entanglement and information flow in optomechanical systems. Exploring alternatives such as coherent scattering [48, 49, 51, 55, 56, 201] might prove to be a very fruitful approach to observe entanglement and nonclassicality in experimental optomechanical systems.

## 5

### Coherent Scattering

Testing quantum mechanics in novel regimes, such as observing quantum effects in systems with many constituents or a large number of degrees-of-freedom, is one of the cornerstones of fundamental science and a promising achievement towards new technologies. A number of experiments have contributed along that direction by studying the quantum mechanics of nano- and microscale objects. For instance, entanglement of hundreds of ions has been observed and controlled [202], interferometric systems have achieved micron-spaced superposition of atomic wavefunctions [203], coherence in Bose-Einstein condensates has been observed [204] and ground state cooling of micron-sized cantilevers and their coupling to superconducting quantum electronics demonstrated [205].

Optically levitated nanoparticles allow exceptional control over translational [15, 16, 47] and rotational [17–19] degrees-of-freedom and achieve excellent environmental isolation [1, 21], thus providing a promising setup for pushing the boundaries of quantum theory towards unexplored regimes. Proposals for generating spatial superposition of levitated nanoparticles have been put forward [10, 184, 206], as well as for testing collapse models [207] and witnessing nonclassicality through recurrence of optical squeezing [182] and optical entanglement [157]. Moreover, levitated systems can give rise to steady-state entanglement [32–34, 51, 208] and help in the search for new physics [209]. On the experimental front, the possibility of detecting nonclassical correlations in levitated particles has been demonstrated [68]. Effective 3D cooling [55, 56], ground state cooling [15, 16] and strong light-matter coupling have been realized [48]. All of these are essential requirements towards entering and controlling the mesoscopic quantum regime.

Ground state cooling of levitated nanoparticles along a single axis was first enabled through the so-called coherent scattering interaction [15, 53], and it has been theoretically shown that simultaneous  $2D$  ground state cooling is possible with the same technique [57]. In this cooling scheme, motion of the particle coherently scatters photons from the trapping beam into an optical cavity tuned to enhance scattering of photons that carry away energy from the trapped object [15, 54]. Following the recent interest on entanglement dynamics

in optomechanical systems [157, 210–213], coherent scattering has also been considered as a platform for generating mechanical entanglement [50, 51].

We begin this Chapter by deriving the many-particle coherent scattering Hamiltonian in close analogy to [54, 214], where an arbitrary number of nanoparticles share a common optical cavity. We will see that by appropriate positioning of the particles with respect to the cavity nodes one can minimize the dispersive optomechanical interaction and favor the coherent scattering terms. Although the unitary dynamics is generated by the Hamiltonian, real-life quantum systems, however, are open. For this reason, we proceed to model the environmental interactions through a set of quantum Langevin equations, associated Lyapunov equation and decoherence mechanisms. We conclude this Chapter studying the entanglement generation in both closed and open dynamics, simulated with a custom numerical toolbox [215], see Appendix C.

## 5.1

### Levitated nanoparticle Hamiltonian

The system we are interested in is comprised of  $N$  optically trapped dielectric nanoparticles (NP) of mass  $m_j$ , each with radius  $R_j$  on the order of magnitude of 100 nm, refractive index  $n_{R,j}$ , homogeneous and isotropic permittivity  $\epsilon_j \approx n_{R,j}^2$ , and polarizability  $\bar{\alpha}_j \equiv 3\epsilon_0 \frac{\epsilon_j - 1}{\epsilon_j + 2}$ . Each NP is optically trapped by an independent optical tweezer (OT) and placed on the axis of a Fabry-Pérot cavity of length  $L$  and resonance frequency  $\omega_c$ , as depicted in Figure 5.1. The tweezers are assumed to be sufficiently apart such that any overlap and cross-talk between the traps can be neglected. All OTs propagate perpendicularly to the cavity axis, have the same frequency  $\omega_t = 2\pi c/\lambda_t$  and their polarization vectors  $\mathbf{e}_{t,j}$  can be decomposed as  $\mathbf{e}_{t,j} = \cos(\theta_j)\mathbf{e}_x + \sin(\theta_j)\mathbf{e}_y$  along the cavity axes.

Following [54], the total Hamiltonian governing the system dynamics can be written as

$$\hat{H} = \hat{H}_{\text{NP}} + \hat{H}_{\text{field}} + \hat{H}_{\text{int}}, \quad (5-1)$$

where the first term is the energy of the free NPs, the second term is the total energy stored in the electromagnetic (EM) field and the third term represents interactions between the NPs and the EM field. To place this Hamiltonian in a suitable form, we consider the different contributions from the electric field present in the system and work on approximating each of these terms individually.

The total electric field is considered to be approximately given by a sum of contributions from the fields of each OT,  $\mathbf{E}_{t,j}$ , the intracavity field,  $\hat{\mathbf{E}}_c$ , and

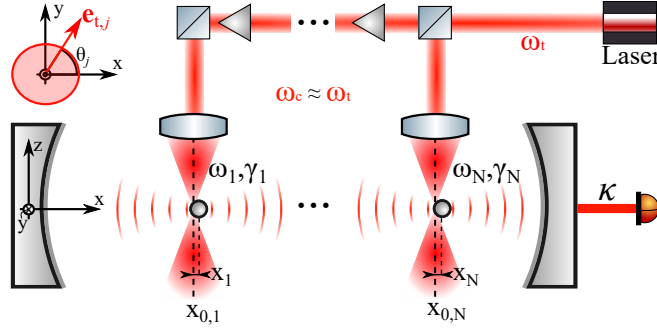


Figure 5.1: Schematics of  $N$  optically levitated nanoparticles, each by its own optical tweezer inside the same optical cavity. Every tweezer has the same frequency which is tuned with the cavity resonance frequency such that the scattered photons can survive inside the cavity. It is assumed that the tweezers are sufficiently spaced such that any overlap between them are negligible. A single external laser serves as the light source for the experiment which passes through a beam splitter (BS) that allows for part of it to tweezer a nanoparticle and part of it to follow to an amplifier and go on to the next BS. Information about the system is retrieved through the leaking field from the rightmost end mirror of the cavity.

the free-space field,  $\hat{\mathbf{E}}_f$ :

$$\hat{\mathbf{E}}(\mathbf{r}) \simeq \hat{\mathbf{E}}_c(\mathbf{r}) + \hat{\mathbf{E}}_f(\mathbf{r}) + \sum_{j=1}^N \mathbf{E}_{t,j}(\mathbf{r}). \quad (5-2)$$

The OTs are considered to be in strong coherent states [54] and thus well described by a classical field. The mean value of the  $j$ -th OT's electric field operator in an appropriate rotating frame is given by

$$\mathbf{E}_{t,j}(\mathbf{r}, t) = \frac{1}{2} \epsilon_t \frac{w_{0,j}}{w_j(z)} e^{-\frac{(x-x_{0,j})^2 + y^2}{w_j^2}} e^{ik_t z} e^{i\phi_{G,j}(z)} e^{i\omega_t t} \mathbf{e}_t + \text{c.c.}, \quad (5-3)$$

where  $P_{t,j}$  is the power,  $k_t = 2\pi/\lambda_t$  the wave-number,  $\mathbf{e}_{t,j}$  the polarization vector,  $w_{0,j}$  the waist and  $\epsilon_{t,j}$ ,  $w_j(z)$ ,  $\phi_G(z)$ ,  $z_{R,j}$  are the field amplitude, beam width, Gouy phase and Rayleigh range, respectively. In close analogy to Chapter 3, following the current notation, these quantities are given by

$$\begin{aligned} \epsilon_{t,j} &= \sqrt{\frac{4P_{t,j}}{w_{0,j}^2 \pi \epsilon_0 c}}, \\ w_j(z) &= w_{0,j} \sqrt{1 + z^2/z_{R,j}^2}, \\ \phi_G(z) &= -\arctan(z/z_{R,j}), \\ z_{R,j} &= k_t w_{0,j}^2 / 2. \end{aligned} \quad (5-4)$$

The intracavity electric field is modelled as a standing wave described quantum



mechanically by the operator

$$\hat{\mathbf{E}}_c(\mathbf{r}) = \epsilon_c (\hat{a}^\dagger + \hat{a}) \cos(k_c x) \mathbf{e}_y, \quad (5-5)$$

where  $k_c = 2\pi/\lambda_c$  is the wave vector,  $\epsilon_c = \sqrt{\frac{\hbar\omega_c}{2\epsilon_0 V_c}}$  the single photon electric field for a cavity of mode volume  $V_c$ ,  $\hat{a}$  the time-dependent annihilation operator and  $\mathbf{e}_y$  the cavity field polarization.

The free EM modes are also modelled quantum mechanically, described by the operator

$$\hat{\mathbf{E}}_f(\mathbf{r}) = \sum_{\mathbf{k}, e} \epsilon_{\mathbf{k}} (\mathbf{e}_{\mathbf{k}} e^{i\mathbf{k} \cdot \mathbf{r}} \hat{c}_{\mathbf{k}, e} + \text{H.c.}) = \sum_l \epsilon_l (\mathbf{e}_l e^{i\mathbf{k} \cdot \mathbf{r}} \hat{c}_l + \text{H.c.}), \quad (5-6)$$

where  $\epsilon_l = \sqrt{\frac{\hbar\omega_l}{2\epsilon_0 V_f}}$ ,  $V_f$  stand for the quantization volume and  $\hat{c}_{\mathbf{k}, e}$  is the annihilation operator of a free EM mode with wave-vector  $\mathbf{k}$  and polarization  $\mathbf{e}_{\mathbf{k}}$ . To simplify the notation, the index  $l$  is used to denote the set  $\{\mathbf{k}, \mathbf{e}_{\mathbf{k}}\}$ . We will see that the effect of interaction with this field is negligible if the NPs are properly positioned within the cavity and sufficiently cooled down. We will therefore drop any term involving the free EM field in the dynamics of the system, however we add this term for completeness at this moment.

The free energy for the NPs and the the EM field [216] are, respectively, given by

$$\hat{H}_{\text{NP}} = \sum_{j=1}^N \frac{\hat{\mathbf{P}}_j^2}{2m_j}, \quad (5-7)$$

$$\hat{H}_{\text{field}} = \frac{\epsilon_0}{2} \int \hat{E}^2(\mathbf{r}) + c^2 \hat{B}^2(\mathbf{r}) d^3\mathbf{r} \simeq \hbar\omega_c \hat{a}^\dagger \hat{a} + \hbar \sum_l \omega_l \hat{c}_l^\dagger \hat{c}_l, \quad (5-8)$$

where  $\hat{\mathbf{P}}_j = (\hat{P}_{x,j}, \hat{P}_{y,j}, \hat{P}_{z,j})$  is the momentum operator vector for the  $j$ -th particle.

In the long wavelength approximation, given by  $R_j \ll \lambda_c, \lambda_{t,j}$ , the interaction Hamiltonian can be expressed as [54, 214, 216],

$$\begin{aligned} \hat{H}_{\text{int}} &= -\frac{1}{2} \int \bar{\mathbf{P}}(\mathbf{r}) \mathbf{E}(\mathbf{r}) d^3\mathbf{r} \simeq -\frac{1}{2} \sum_{j=1}^N \alpha_j |\hat{\mathbf{E}}(\hat{\mathbf{r}}_j)|^2 \\ &= -\frac{1}{2} \sum_{j=1}^N \alpha_j \left| \hat{\mathbf{E}}_c(\hat{\mathbf{r}}_j) + \hat{\mathbf{E}}_f(\mathbf{r}) + \mathbf{E}_{t,j}(\hat{\mathbf{r}}_j) \right|^2, \end{aligned} \quad (5-9)$$

where  $\bar{\mathbf{P}}_j(\mathbf{r}) = \bar{\alpha}_j \mathbf{E}(\mathbf{r})$  is the  $j$ -th NP polarization vector and  $\alpha = \bar{\alpha}V = 4\pi\epsilon_0 R^3 \frac{\epsilon_j - 1}{\epsilon_j + 2}$ . Here  $\hat{\mathbf{r}}_j = \mathbf{R}_{0,j} + \hat{\mathbf{R}}_j$  denotes the center-of-mass position operator of the  $j$ -th particle, with  $\mathbf{R}_{0,j} = (x_{0,j}, 0, 0)^T$  being the mean position of the

$j$ -th OT along the cavity axis and  $\hat{\mathbf{R}}_j = (\hat{X}_j, \hat{Y}_j, \hat{Z}_j)^T$  the fluctuations of the particle around  $\mathbf{R}_{0,j}$ . The interaction Hamiltonian is simplified by assuming that the *overlap* term proportional to  $\mathbf{E}_{t,j}(\hat{\mathbf{r}}_j)\mathbf{E}_{t,i}(\hat{\mathbf{r}}_j)$  is negligible for  $i \neq j$ , i.e.,  $\mathbf{E}_{t,i}(\hat{\mathbf{r}}_j) \approx \delta_{ij}\mathbf{E}_{t,i}(\hat{\mathbf{r}}_j)$ .

In order to evaluate the final form of the interaction energy, we use the definitions of each electric field given by Equations (5-3, 5-5, 5-6). The gaussian tweezers will effectively trap the NPs close to their focus, confining them in the vicinity of  $\mathbf{R}_{0,j}$ , in analogy to the discussion on Section 3.3. Thus we can approximate the interaction Hamiltonian through a series expansion around  $(\hat{X}_j, \hat{Y}_j, \hat{Z}_j) = \mathbf{0}$  in each term. Moreover, as the optical modes' frequencies ( $\omega_{t,j} \approx \omega_c$ ) are much higher than the coupling rates present in the system, we also take a rotating-wave approximation (RWA) at these frequencies in each interaction term. Finally, we disregard the constant energy shifts as they do not affect the dynamics of the system.

The tweezers-tweezers interaction give rise to 3D harmonic potentials on the NPs, effectively levitating them with trapping frequencies  $\omega_{i,j}$ ,  $i = x, y, z$ , given by

$$-\frac{\alpha}{2}|\hat{E}_{t,j}(\hat{\mathbf{R}})|^2 = \sum_{\substack{i=x,y,z}} \frac{m\Omega_{j,i}^2}{2} \hat{\mathbf{R}}_{j,i}^2, \quad \Omega_j = \begin{bmatrix} \omega_{j,x} \\ \omega_{j,y} \\ \omega_{j,z} \end{bmatrix} = \begin{bmatrix} \sqrt{\frac{4\alpha_j P_{t,j}}{m_j w_{0,j}^4 \pi \epsilon_0 c}} \\ \sqrt{\frac{4\alpha_j P_{t,j}}{m_j w_{0,j}^4 \pi \epsilon_0 c}} \\ \sqrt{\frac{2\alpha_j P_{t,j}}{m_j w_{0,j}^2 z_{R,j}^2 \pi \epsilon_0 c}} \end{bmatrix}. \quad (5-10)$$

The cavity-cavity interaction results in three terms:

$$-\frac{1}{2}\alpha_j|\mathbf{E}_c(\hat{\mathbf{r}}_j)|^2 \approx -\hbar\delta_j \cos^2(k_c x_{0,j}) \hat{a}^\dagger \hat{a} + \hbar k_c \delta_j \sin(2k_c x_{0,j}) \hat{X}_j \left[ \hat{a}^\dagger \hat{a} + \frac{1}{2} \right], \quad (5-11)$$

with  $\delta_j = \frac{\alpha_j \omega_c}{2\epsilon_0 V_c}$ . One term proportional only to the cavity's number operator, responsible for the cavity frequency shift due to the presence of the  $j$ -th particle, one proportional to the  $j$ -th NP position quadrature, acting as a constant drive in the NP's momentum, and an interacting term resulting in the radiation pressure effect on the  $j$ -th NP by the cavity field, as discussed in Section 4.1.2.

The cavity-tweezers interactions yield

$$-\alpha_j \text{Re} \left( \hat{\mathbf{E}}_c(\hat{\mathbf{r}}_j) \mathbf{E}_{t,j}^*(\hat{\mathbf{r}}_j) \right) \approx -\alpha_j \epsilon_t \epsilon_c \sin(\theta_j) (\hat{a}^\dagger + \hat{a}) \quad (5-12)$$

$$\times \left\{ \cos(\omega_t t) \left( \cos(k_c x_{0,j}) - k_c \hat{X}_j \sin(k_c x_{0,j}) \right) - \hat{Z}_j \frac{k_t z_{R_j} - 1}{z_{R_j}} \sin(\omega_t t) \cos(k_c x_{0,j}) \right\},$$

which gives rise to the coherent scattering (CS) interaction [54], effectively 2D

coupling the NPs with the cavity field and a drive in the cavity field. The nature of this interaction can be intuitively understood as due to the OT's photons being coherently scattered by the trapped NPs into the cavity mode, populating it [53, 54, 56].

The free field interaction yields

$$-\frac{1}{2}\alpha_j|\mathbf{E}_f(\hat{\mathbf{r}}_j)|^2 = -\frac{\alpha_j\hbar}{4\epsilon_0 V_f} \sum_l \sum_{l'} \sqrt{\omega_l \omega_{l'}} \mathbf{e}_l \cdot \mathbf{e}_{l'} (e^{i\mathbf{k} \cdot \hat{\mathbf{r}}_j} \hat{c}_l + \text{H.c.}) (e^{i\mathbf{k}' \cdot \hat{\mathbf{r}}_j} \hat{c}_{l'} + \text{H.c.}), \quad (5-13)$$

however, it has been shown that in the long-wavelength approximation this can be safely neglected [217] and, thus, it will be set aside from now on.

The cavity-free field interaction, with  $G_{cf}(l) = \alpha_j \epsilon_l \epsilon_c \mathbf{e}_l \cdot \mathbf{e}_y / \hbar$ , is given by

$$-\alpha_j \text{Re} \left( \hat{\mathbf{E}}_c(\hat{\mathbf{r}}_j) \hat{\mathbf{E}}_f^*(\hat{\mathbf{r}}_j) \right) \approx -\hbar \sum_l G_{cf}(l) (\hat{a}^\dagger + \hat{a}) (e^{i\mathbf{k} \cdot \mathbf{R}_{0,j}} \hat{c}_l + e^{-i\mathbf{k} \cdot \mathbf{R}_{0,j}} \hat{c}_l^\dagger) \cos(k_c x_{0,j}). \quad (5-14)$$

Lastly, the tweezers-free fields interactions are

$$\begin{aligned} -\alpha_j \text{Re} \left( \hat{\mathbf{E}}_f(\hat{\mathbf{r}}_j) \mathbf{E}_{t,j}^*(\hat{\mathbf{r}}_j) \right) \approx & \quad (5-15) \\ -\hbar \sum_l G_{tf}(l) \left[ (e^{i\mathbf{k} \cdot \mathbf{R}_{0,j}} \hat{c}_l + e^{-i\mathbf{k} \cdot \mathbf{R}_{0,j}} \hat{c}_l^\dagger) \left( \cos(\omega_t t) - \hat{z}_j \frac{k_t z_{R,j} - 1}{z_{R,j}} \sin(\omega_t t) \right) \right. \\ & \left. + i\mathbf{k} \cdot \hat{\mathbf{R}}_j (e^{i\mathbf{k} \cdot \mathbf{R}_{0,j}} \hat{c}_l - e^{-i\mathbf{k} \cdot \mathbf{R}_{0,j}} \hat{c}_l^\dagger) \cos(\omega_t t) \right], \end{aligned}$$

where  $G_{tf}(l) = \alpha_j \epsilon_l \epsilon_t \mathbf{e}_l \cdot \mathbf{e}_y / \hbar$ . This term is the source of recoil heating of the NP as they incoherently scatters light off the tweezers into free space [48].

Note that these terms that compose the interaction Hamiltonian have a time dependency, which we can get rid off by moving into a rotating reference frame at the frequency of the tweezers,  $\omega_t$ , according to

$$\hat{H} \rightarrow \hat{U} \hat{H} \hat{U}^\dagger - i\hbar \hat{U} \frac{\partial \hat{U}^\dagger}{\partial t} \quad , \quad \hat{U}(t) \equiv \exp \left( i\omega_t t \left[ \hat{a}^\dagger \hat{a} + \sum_l \hat{c}_l^\dagger \hat{c}_l \right] \right). \quad (5-16)$$

We begin with the term relative to the explicit time dependency of the unitary operator  $\hat{U}(t)$ , which simply introduces a frequency shift in the intracavity and free EM fields

$$-i\hbar \hat{U} \frac{\partial \hat{U}^\dagger}{\partial t} = -\hbar\omega_t \hat{a}^\dagger \hat{a} - \hbar\omega_t \sum_l \hat{c}_l^\dagger \hat{c}_l.$$

The interaction energy in Equation (5-10) has no dependency with the cavity or free field operators and, thus, is not altered. However, the annihilation operators for these modes transform according to

$$\begin{aligned}\hat{U}(t) \hat{a} \hat{U}^\dagger(t) &= e^{-i\omega_t t} \hat{a} & \hat{U}(t) \hat{a}^\dagger \hat{U}^\dagger(t) &= e^{+i\omega_t t} \hat{a}^\dagger \\ \hat{U}(t) \hat{c}_l \hat{U}^\dagger(t) &= e^{-i\omega_t t} \hat{c}_l & \hat{U}(t) \hat{c}_l^\dagger \hat{U}^\dagger(t) &= e^{+i\omega_t t} \hat{c}_l^\dagger\end{aligned}$$

An immediate consequence of the above equations is that number operators are not altered by this change of reference frame. Therefore, the free evolution energy terms and the cavity-cavity term, Equation (5-11), remain the same.

The tweezer-cavity and tweezer-free interactions, respectively Equations (5-12) and (5-15), transform analogously using the above identities and expanding the time dependent trigonometric functions as combinations of complex exponentials such that

$$\begin{aligned}\hat{U} (\hat{a}^\dagger + \hat{a}) \cos(\omega_t t) \hat{U}^\dagger &= +\frac{1}{2} [\hat{a}^\dagger (e^{i2\omega_t t} + 1) + \hat{a} (1 + e^{-i2\omega_t t})] \xrightarrow{\text{RWA}} \frac{1}{2} [\hat{a} + \hat{a}^\dagger], \\ \hat{U} (\hat{a}^\dagger + \hat{a}) \sin(\omega_t t) \hat{U}^\dagger &= -\frac{i}{2} [\hat{a}^\dagger (e^{i2\omega_t t} - 1) + \hat{a} (1 - e^{-i2\omega_t t})] \xrightarrow{\text{RWA}} \frac{i}{2} [\hat{a}^\dagger - \hat{a}],\end{aligned}$$

where we once again applied a RWA by neglecting all rapidly oscillating terms at frequency  $2\omega_t$ . The tweezer-free term transforms analogously.

The cavity-free term, Equation (5-14) transform according to

$$\begin{aligned}\hat{U}(t) (\hat{a}^\dagger + \hat{a}) (e^{i\mathbf{k}\cdot\mathbf{R}_{0,j}} \hat{c}_l + e^{-i\mathbf{k}\cdot\mathbf{R}_{0,j}} \hat{c}_l^\dagger) \hat{U}^\dagger(t) \\ = (\hat{a}^\dagger e^{+i\omega_t t} + \hat{a} e^{-i\omega_t t}) (e^{i\mathbf{k}\cdot\mathbf{R}_{0,j}} \hat{c}_l e^{-i\omega_t t} + e^{-i\mathbf{k}\cdot\mathbf{R}_{0,j}} \hat{c}_l^\dagger e^{+i\omega_t t}) \\ \xrightarrow{\text{RWA}} e^{i\mathbf{k}\cdot\mathbf{R}_{0,j}} \hat{a}^\dagger \hat{c}_l + e^{-i\mathbf{k}\cdot\mathbf{R}_{0,j}} \hat{a} \hat{c}_l^\dagger\end{aligned}$$

Finally, gathering all the terms above, we find the full Hamiltonian for the CS system with  $N$  particles

$$\begin{aligned}\hat{H} &= \hbar\Delta\hat{a}^\dagger\hat{a} + \hbar\sum_l\Delta_l\hat{c}_l^\dagger\hat{c}_l + \sum_{j=1}^N\left\{\frac{\hat{\mathbf{P}}_j^2}{2m_j} + \hat{\mathbf{R}}_j^T\Omega_j^2\hat{\mathbf{R}}_j\right. \\ &\quad - \hbar G_j \sin(\theta_j) \cos(k_c x_{0,j}) (\hat{a}^\dagger + \hat{a}) - \hbar \frac{g_{0,j}}{2} \sin(2k_c x_{0,j}) \hat{X}_j \\ &\quad - \hbar g_{0,j} \sin(2k_c x_{0,j}) \hat{a}^\dagger \hat{a} \hat{X}_j \\ &\quad + \hbar G_{x,j} \sin(k_c x_{0,j}) \sin(\theta_j) (\hat{a}^\dagger + \hat{a}) \hat{X}_j + i\hbar G_{z,j} \cos(k_c x_{0,j}) \sin(\theta_j) (\hat{a}^\dagger - \hat{a}) \hat{Z}_j \\ &\quad - \hbar \sum_l G_{\text{tf}}(l) \left[ \left( \hat{c}_l e^{i\mathbf{k}\cdot\mathbf{R}_{0,j}} + \hat{c}_l^\dagger e^{-i\mathbf{k}\cdot\mathbf{R}_{0,j}} \right) - i \left( \hat{c}_l^\dagger e^{-i\mathbf{k}\cdot\mathbf{R}_{0,j}} - \hat{c}_l e^{i\mathbf{k}\cdot\mathbf{R}_{0,j}} \right) \left( \mathbf{k} \cdot \hat{\mathbf{R}}_j + \hat{z}_j \frac{k_t z_{\text{R},j} - 1}{z_{\text{R},j}} \right) \right] \Big\} \\ &\quad - \hbar \sum_l G_{\text{cf}}(l) \left[ e^{+i\mathbf{k}\cdot\mathbf{R}_{0,j}} \hat{a}^\dagger \hat{c}_l + e^{-i\mathbf{k}\cdot\mathbf{R}_{0,j}} \hat{a} \hat{c}_l^\dagger \right] \cos(k_c x_{0,j}),\end{aligned}\tag{5-17}$$

where  $\Delta \equiv \omega_c - \omega_t - \sum_{j=1}^N \delta_j \cos^2(k_c x_{0,j})$  is the shifted cavity frequency,  $\Delta_l \equiv \omega_l - \omega_t$  is the shifted free field frequency,  $g_{0,j} = k_c \delta_j$  are the dispersive couplings with  $\delta_j = \frac{\alpha_j \omega_c}{2\epsilon_0 V_c}$ ,  $G_{x,j} = k_c G_j$  and  $G_{z,j} = \frac{k_t z_{R,j} - 1}{z_{R,j}} G_j$  are the bare CS couplings in the  $x$  and  $z$  directions for the  $j$ -th particle with  $G_j = \frac{\alpha_j \epsilon_t \epsilon_c}{2\hbar}$ .

Equation (5-17) is a rather convoluted Hamiltonian, let us break it apart. The first line dictates the free evolution of the cavity mode, the free EM field and the trapped NPs, all of which are described as quantum harmonic oscillators. The second line describes constant drives on the cavity field and NPs, in Section 5.2.1.1 we will study the effect of a driving term. The third line is the dispersive coupling we have already dealt with in Chapter 4; notice that if the tweezers' polarizations are aligned with the cavity ( $\theta_j = 0$ ), then there is only a dispersive coupling between the cavity and the NPs. The fourth line describes the CS interaction, between the particle motion along the cavity axis and in the perpendicular direction; notice that each direction couples with a different cavity quadrature. The fifth line dictates a driving term in the free field and a coupling with the NPs. At last, the sixth line creates a coupling between the cavity and the free field describing photons exchange.

### 5.1.1

#### Coherent Scattering Hamiltonian

In order to favour the CS couplings over the dispersive ones, we place the NPs' mean position at the cavity nodes ( $k_c x_{0,j} = (2n_j + 1)\pi/2$ ,  $n_j \in \mathbb{N}$ ) by properly positioning their respective OT. Consequently the total Hamiltonian simplifies to

$$\hat{H}/\hbar \approx \Delta \hat{a}^\dagger \hat{a} + \sum_{j=1}^N \omega_j \hat{b}_j^\dagger \hat{b}_j + \sum_{j=1}^N g_j (\hat{a}^\dagger + \hat{a})(\hat{b}_j^\dagger + \hat{b}_j), \quad (5-18)$$

where  $\hat{b}_j(\hat{b}_j^\dagger)$  is the annihilation (creation) operator for the  $j$ -th NP such that  $\hat{X}_j = x_{ZPF,j}(\hat{b}_j^\dagger + \hat{b}_j)$ , with  $x_{ZPF,j} = \sqrt{\hbar/(2m_j\omega_j)}$  the zero point fluctuation for the  $j$ -th NP. Note that the shifted cavity frequency simplifies to  $\Delta = \omega_c - \omega_t$  and  $g_j \equiv x_{ZPF,j} G_{x,j} \sin(\theta_j)$  are the CS coupling.

We also observe that for the case of a single NP, the Hamiltonian is symmetric between optical and mechanical modes. We note that it describes also the situation within the linearized dispersive optomechanical approximation [23].

Moreover, we have chosen to disregard the coupling between the NPs and the free field. For typical experimental values [15, 218], one usually have  $w_{0,j} \approx 0.7 \mu\text{m}$  such that  $\frac{k_t z_{R,j} - 1}{z_{R,j}} \approx k_t \simeq 5.9 \cdot 10^{-3} \text{ nm}^{-1}$ ,  $\omega_j \approx 2\pi \cdot 305 \text{ kHz}$ , and the mass of a single nanoparticle  $m_j \approx 2.83 \text{ fg}$  such that  $x_{ZPF,j} \approx 3.1 \text{ pm}$ . Therefore, for

a particle in the motional ground state, it is expected that its coupling to the free field contribution to the total Hamiltonian plays a negligible role compared to the first term in the Equation above, as  $k_t \cdot x_{\text{ZPF},j} \sim k \cdot x_{\text{ZPF},j} \ll 1$ .

If we consider a more energetic initial quantum state for the nanoparticles, say a thermal state at temperature  $T = 10$  K, through the equipartition theorem we could assert that initially  $\sqrt{\langle x_j^2 \rangle} = \sqrt{k_B T / (m_j \omega_j^2)} \simeq 5.85$  nm, such that we would still have  $k_t \cdot \sqrt{\langle x_j^2 \rangle} \sim k \cdot \sqrt{\langle x_j^2 \rangle} \ll 1$ . Therefore, we can safely ignore the nanoparticles' interaction with the free field for sufficiently cooled down particles, making the free field evolution uncoupled to the nanoparticles and, thus, ignored.

## 5.2

### Quantum Langevin equations

In Section 4.2, we studied the closed quantum dynamics of a system under the unitary time evolution of a dispersive Hamiltonian. This description captures the essential properties of the dynamics of the system, at the cost of relying in an idealized scenario. In this Section, we introduce a more general/realistic description of an optomechanical experiment by also considering its interaction with the environment, which we model through the standard treatment of a set of quantum Langevin equations (QLEs) for optomechanics [23, 33, 40, 219–221].

#### 5.2.1

##### Input-Output formalism

Our discussion starts with only the optical mode of a Fabry-Pérot cavity. In a realistic scenario, the end mirrors that form the optical cavity are not perfect and allow photon transfer between the resonant photons inside the cavity and the EM field outside it, as shown in Figure 5.2.

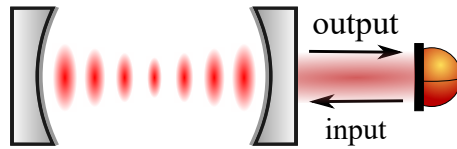


Figure 5.2: Fabry-Pérot cavity with an imperfect rightmost end mirror.

Consequently, we model the complete system of the optical cavity field and the external EM field through the Hamiltonian [219, 222]

$$\hat{H}_{\text{IO}} = \hbar \omega_c \hat{a}^\dagger \hat{a} + \hbar \int_{-\infty}^{+\infty} \omega \hat{b}^\dagger(\omega) \hat{b}(\omega) d\omega + i\hbar \int_{-\infty}^{+\infty} \kappa(\omega) [\hat{a}^\dagger \hat{b}(\omega) - \hat{a} \hat{b}^\dagger(\omega)] d\omega, \quad (5-19)$$

where  $\hat{a}$  ( $\hat{a}^\dagger$ ) stand for the annihilation (creation operator) operator for the cavity mode with frequency  $\omega_c$ ;  $\hat{b}$  ( $\hat{b}^\dagger$ ) stand for the annihilation (creation operator) operator for the external field modelled as a bosonic bath; and  $\kappa(\omega)$  describes the coupling of between the cavity field and the bosonic bath mode with frequency  $\omega$ . We assume that different bath modes do not interact and, thus, obey the commutation relations  $[\hat{b}(\omega), \hat{b}^\dagger(\omega')] = \delta(\omega - \omega')\mathbb{1}$ .

For simplicity, we have only considered one imperfect mirror for the cavity and a generalization for losses through both mirrors is straightforward. Moreover, we also made the integrals over the external EM field frequencies range inside  $(-\infty, \infty)$ . Negative frequencies might seem contradictory, however it is common in quantum optomechanics to work in a rotating reference frame, at frequency  $\Omega$ , such that the practical frequency range  $\omega \in (0, \infty)$  transforms into  $\omega \in (-\Omega, \infty)$ . As optical frequencies tend to be very large compared to the coupling rates and natural frequencies of the system, the frequency range considered above is a good approximation to the real physical situation.

Aiming at a set of quantum Langevin equations, we derive the Heisenberg's equation of motions for  $\hat{a}$  and  $\hat{b}$ :

$$\dot{\hat{b}}(\omega, t) = -i\omega\hat{b}(\omega, t) + \kappa(\omega)\hat{a}(t), \quad (5-20)$$

$$\dot{\hat{a}}(t) = -i\omega_c\hat{a}(t) + \int_{-\infty}^{+\infty} \kappa(\omega)\hat{b}(\omega, t)d\omega. \quad (5-21)$$

We now define  $\hat{b}_0(\omega) \equiv \hat{b}(\omega, t_0)$  as the bath's annihilation operator on the initial time  $t_0 < t$ , and obtain a general form for  $\hat{b}(\omega, t)$  from Equation (5-20)

$$\hat{b}(\omega, t) = e^{-i\omega(t-t_0)}\hat{b}_0(\omega) + \kappa(\omega) \int_{t_0}^t e^{-i\omega(t-t')} \hat{a}(t')dt'. \quad (5-22)$$

This is done in order for us to substitute it back into the equation of motion for the cavity annihilation operator and effectively eliminate the dependency with the external EM field dynamics, giving rise to

$$\dot{\hat{a}}(t) = -i\omega_c\hat{a}(t) + \int_{-\infty}^{+\infty} \kappa(\omega) e^{-i\omega(t-t_0)} \hat{b}_0(\omega)d\omega + \int_{t_0}^t \int_{-\infty}^{+\infty} \kappa^2(\omega) e^{-i\omega(t-t')} \hat{a}(t')dt'd\omega. \quad (5-23)$$

In order to make the resulting equation of motion to be in the form of a Langevin Equation we introduce the First Markov Approximation. The coupling  $\kappa(\omega)$  is considered to be independent of the bath mode frequency,  $\kappa(\omega) \equiv \sqrt{\kappa/2\pi}$ , where  $\kappa$  is the cavity linewidth as defined in Section 2.3. We also define the input field operator

$$\hat{b}_{\text{in}}(t) \equiv \frac{1}{\sqrt{2\pi}} \int_{-\infty}^{+\infty} e^{-i\omega(t-t_0)} \hat{b}_0(\omega)d\omega \quad (5-24)$$

which describes the optical input fluctuation acting on the cavity field. This can be promptly understood once we observe the resulting form of the equations of motions for the cavity field operators

$$\dot{\hat{a}}(t) = -i\omega_c \hat{a}(t) - \frac{\kappa}{2} \hat{a}(t) + \sqrt{\kappa} \hat{b}_{\text{in}}(t), \quad (5-25)$$

$$\dot{\hat{a}}^\dagger(t) = +i\omega_c \hat{a}^\dagger(t) - \frac{\kappa}{2} \hat{a}^\dagger(t) + \sqrt{\kappa} \hat{b}_{\text{in}}^\dagger(t). \quad (5-26)$$

We note that if the external EM field is considered to be in a vacuum state, a realistic assumption in most optomechanical experiments, then  $\hat{b}_{\text{in}}$  and  $\hat{b}_{\text{in}}^\dagger$  are zero-averaged and delta-correlated optical input noise terms, satisfying  $\langle \hat{b}_{\text{in}}(t) \hat{b}_{\text{in}}^\dagger(t') \rangle = \delta(t - t')$  [219]. Observe that the dynamics this QLEs entails is Markovian.

Moreover, had we considered  $t_1 > t$  as the “initial time”, we would arrive at a time-reversed Langevin equation [219] and, analogously to (5-22), define

$$\hat{b}_{\text{out}}(t) \equiv -\frac{1}{\sqrt{2\pi}} \int_{-\infty}^{+\infty} e^{-i\omega(t-t_1)} \hat{b}_1(\omega) d\omega. \quad (5-27)$$

This quantity is interpreted as the output field leaking from the optical cavity, which can be experimentally accessed and carries information about the internal degrees of freedom of the cavity, as can be seen from the input-output relation

$$\hat{b}_{\text{out}}(t) + \hat{b}_{\text{in}}(t) = \sqrt{\kappa} \hat{a}(t). \quad (5-28)$$

Finally, we move to a quadrature representation. For the cavity field,  $\hat{X}(t) \equiv \hat{a}^\dagger(t) + \hat{a}(t)$ ,  $\hat{P}(t) \equiv i[\hat{a}^\dagger(t) - \hat{a}(t)]$ ; for the input field:  $\hat{X}_{\text{in}}(t) \equiv \hat{b}_{\text{in}}^\dagger(t) + \hat{b}_{\text{in}}(t)$ ,  $\hat{P}_{\text{in}}(t) \equiv i[\hat{b}_{\text{in}}^\dagger(t) - \hat{b}_{\text{in}}(t)]$ . Thus, we obtain another set of quantum Langevin equations for the cavity field

$$\dot{\hat{X}}(t) = \omega_c \hat{P}(t) - \frac{\kappa}{2} \hat{X}(t) + \sqrt{\kappa} \hat{X}_{\text{in}}(t), \quad (5-29)$$

$$\dot{\hat{P}}(t) = -\omega_c \hat{X}(t) - \frac{\kappa}{2} \hat{P}(t) + \sqrt{\kappa} \hat{P}_{\text{in}}(t). \quad (5-30)$$

### 5.2.1.1

#### External laser driving

Consider the case where the optical cavity is not only interacting with a external field in a vacuum state but it is also actively driven by an external laser, as depicted in Figure 5.3.

Still working within the First Markov Approximation, a strong coherent



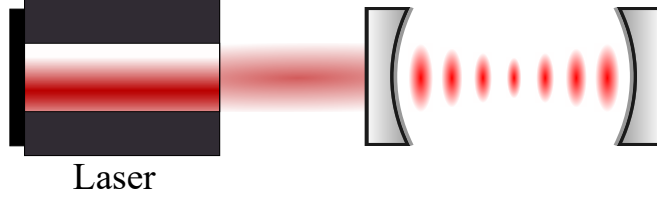


Figure 5.3: Schematics of an optical cavity being actively driven by an external laser.

drive into the cavity, at the laser frequency  $\omega_d$ , transforms the bosonic bath annihilation operator as  $\hat{b}(\omega_d) e^{-i\omega_d t} \rightarrow \sqrt{\frac{2\pi}{\kappa}} E_d e^{-i\omega_d t} + \hat{b}(\omega_d) e^{-i\omega_d t}$ , where  $E_d \in \mathbb{R}$  is the cavity drive in units of  $\sqrt{\# \text{ photons}/s}$  [222]. Making this substitution into the Hamiltonian in equation (5-19), we obtain the driving term

$$\hat{H}_{\text{IO}} \rightarrow \hat{H}_{\text{IO}} + i\hbar E_d (\hat{a}^\dagger e^{-i\omega_d t} - \hat{a} e^{+i\omega_d t}). \quad (5-31)$$

Let us forget for a moment the Input-Output interaction and take a look at the Heisenberg equations arising solely from the interaction with this driving term

$$\dot{\hat{a}} = -i\omega_c \hat{a} + E_d e^{-i\omega_d t}, \quad (5-32)$$

In the following, we will make the Ansatz that the equation above is solved by

$$\hat{a}(t) = \hat{a}(0) e^{-i\omega_c t} + F(t), \quad (5-33)$$

where  $F(t)$  is some scalar function with  $F(0) = 0$ . After plugging this Ansatz back into (5-32) and performing some simple algebraic manipulation, it is easy to see the Heisenberg equation is solved by our proposed solution if the following differential equation is satisfied

$$i\omega_c F(t) + \dot{F}(t) = E_d e^{-i\omega_d t}, \quad (5-34)$$

with initial condition  $F(0) = 0$ . Therefore,  $F(t)$  is given by

$$F(t) = 2 \frac{E_d}{\omega_c - \omega_d} \sin\left(\frac{\omega_c - \omega_d}{2} t\right) e^{-i\frac{\omega_c + \omega_d}{2} t}. \quad (5-35)$$

Let us discuss the physical meaning of the results above. First, Equation (5-31) tell us how the energy of the system is altered by the presence of a strong external laser. Secondly, Equation (5-33) indicates that the effect of this laser is to displace the annihilation operator by  $F(t)$  at time  $t$ .

Consider the case of an initially empty cavity starting in the vacuum state  $|\psi(0)\rangle = |0\rangle$ , at some latter time  $t$ , we can easily find the time evolution of this state employing Equation (5-33):

$$\hat{a}(t) |0\rangle = e^{-i\omega_c t} \hat{a} |0\rangle + F(t) |0\rangle = F(t) |0\rangle \quad (5-36)$$

Now,  $\hat{a}(t) = \hat{U}(t)^\dagger \hat{a} \hat{U}(t)$ , where  $\hat{U}(t)$  is the time evolution operator associated to  $\hat{H}_{\text{IO}}$ . Hence

$$|\Psi(t)\rangle = \hat{U}(t) |0\rangle \Rightarrow \hat{a} |\Psi(t)\rangle = F(t) |\Psi(t)\rangle \quad (5-37)$$

Consequently, we find that  $|\Psi(t)\rangle$  is a coherent state, with average photon number  $|F(t)|^2$ . The same analysis as above can be carried out starting with some coherent state  $|\alpha\rangle$ , instead of the vacuum. We then see that the driving term takes this state into another coherent state with amplitude  $\alpha e^{-i\omega_c t} + F(t)$ .

We end our discussion on this subject by analysing the resonance case  $\omega_d \rightarrow \omega_c$ , which reduces  $F(t)$  to:

$$F_R(t) = e^{-i\omega_c t} E_d t. \quad (5-38)$$

Notice that, in this case, if we drive the cavity for  $T$  seconds, starting from the vacuum, then the cavity will be prepared in a coherent state with  $E_d^2 T^2$  photons. We observe that the limit taken above rests on the assumption that  $|\omega_c - \omega_d|T \ll 1$ , which holds as long as the detuning  $|\omega_c - \omega_d|$  is much smaller than  $T^{-1}$ .

### 5.2.2

#### Quantum brownian motion

We now consider the environmental effect on the levitated NP. Current experimental implementations with levitated NP often place the system inside vacuum chambers in moderate to high vacuum (pressures ranging from  $10^{-6}$  mbar [218] to 1.4 mbar [48], for example) which results in excellent environmental isolation [1, 21] for such systems. However, there is always some residual gas inside these chambers that, at the same time, imprints random kicks in the NP's momentum and dampens its motion, as depicted in Figure 5.4. Following [220], we present a description of this quantum Brownian motion.

Let  $M$  be the mass of a particle with canonically conjugate position and momentum operators given by  $\hat{Q}$  and  $\hat{P}$  under a potential  $V(\hat{Q})$ .

The system is modelled to be in contact with a heat bath modeled as a set of  $N$  uncoupled harmonic oscillator of mass  $m_i$ , natural frequency  $\omega_i$ , position  $\hat{x}_i$  and momentum  $\hat{p}_i$ . The Hamiltonian for this whole system reads

$$\hat{H} = \frac{P^2}{2M} + V(Q) + \sum_{j=1}^N \frac{\hat{p}_j^2}{2m_j} + \frac{m_j \omega_j^2}{2} \hat{x}_j^2 + \hat{H}_{\text{int}}. \quad (5-39)$$

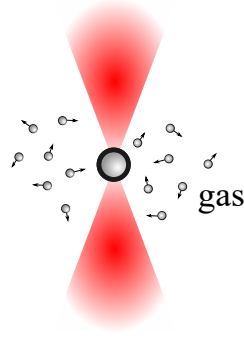


Figure 5.4: Levitated nanoparticle and the surrounding gas imprinting random kicks and damping on its motion.

where the interaction energy between the system and heat bath is given by a Caldeira-Leggett-like Hamiltonian [223]

$$\hat{H}_{SB} = -\hat{Q} \sum_{j=1}^N c_j \hat{x}_j + \hat{Q}^2 \sum_{j=1}^N \frac{c_j^2}{2m_j \omega_j^2} \quad (5-40)$$

where  $c_i$  is the coupling strength between  $i$ -th mode of the heat bath and the particle. Note that the first interaction term is a position-position coupling equivalent to the CS coupling derived in Section 5.1 and, if the system is subjected to an harmonic potential, the second interaction term only shifts the natural frequency of the system.

As a mean to obtain a better physical interpretation of this form of interaction, we make the transformation  $\hat{x}_j = \lambda_j \hat{x}'_j$ ,  $\lambda_j \equiv m_j \omega_j^2 / c_j$ , such that the total Hamiltonian for the system and heat bath can be recast as

$$\hat{H} = \frac{P^2}{2M} + V(Q) + \sum_{j=1}^N \frac{\hat{p}_j^2}{2m_j} + \frac{m_j \omega_j^2}{2} (\hat{Q} - \hat{x}'_j)^2, \quad (5-41)$$

and we observe that while the particles is subject to a potential  $V$ , each constituent of the heat bath is modelled as if attached to the particle by a spring. In the following, we forget this rescaling.

In order to arrive in a QLE, we will follow the same procedure as in the previous section. First, we derive the Heisenberg's equations of motion for the NP

$$\frac{d}{dt} \hat{Q} = \frac{1}{M} \hat{P}, \quad (5-42)$$

$$\frac{d}{dt} \hat{P} = \frac{i}{\hbar} [V(Q), \hat{P}] + \sum_{i=1}^N (c_i \hat{x}_i) - Q \sum_{i=1}^N \frac{c_i^2}{m_i \omega_i^2}, \quad (5-43)$$

and, analogously for the heat bath, we arrive at the following equation of motion

$$\ddot{\hat{x}}_i + \omega_i^2 \hat{x}_i = \frac{c_i}{m_i} \hat{Q}. \quad (5-44)$$

We proceed to eliminate the heat bath's information from the particle dynamics by finding a formal solution for the time evolution of heat bath's position

$$\begin{aligned} \hat{x}_i(t) = \hat{x}_i(t_0) \cos(\omega_i(t - t_0)) + \frac{\hat{p}_i(t_0)}{m_i \omega_i} \sin(\omega_i(t - t_0)) \\ + \int_{t_0}^t \frac{c_i}{m_i \omega_i} \sin(\omega_i(t - s)) \hat{Q}(s) ds \end{aligned} \quad (5-45)$$

where  $t_0$  is the initial time of the particle-heat bath coupling, and insert it back into the particle's equations of motion

$$\begin{aligned} \dot{\hat{P}} = \frac{i}{\hbar} [V(\hat{Q}), \hat{P}] - \hat{Q} \sum_{i=1}^N \frac{c_i^2}{m_i \omega_i^2} \\ + \sum_{i=1}^N c_i \left( \hat{x}_i(t_0) \cos(\omega_i(t - t_0)) + \frac{\hat{p}_i(t_0)}{m_i \omega_i} \sin(\omega_i(t - t_0)) \right) \\ + \sum_{i=1}^N \frac{c_i^2}{m_i \omega_i} \int_{t_0}^t \sin(\omega_i(t - s)) \hat{Q}(s) ds. \end{aligned} \quad (5-46)$$

We proceed to perform an integration by parts in the last term on the previous equation and simplify our notation. This way we arrive at a generalized Langevin equation where the information the bath is completely encompassed inside the memory kernel  $\gamma(t)$  and the external force term  $\hat{f}(t)$ :

$$\dot{\hat{P}}(t) = \frac{i}{\hbar} [V(\hat{Q}), \hat{P}(t)] - \int_{t_0}^t \gamma(t - s) \dot{\hat{Q}}(s) ds - \gamma(t - t_0) \hat{Q}(t_0) + \hat{f}'(t) \quad (5-47)$$

where

$$\gamma(t) \equiv \sum_{i=1}^N \frac{c_i^2}{m_i \omega_i^2} \cos(\omega_i t), \quad (5-48)$$

$$\hat{f}'(t) \equiv \sum_{i=1}^N c_i \left( \hat{x}_i(t_0) \cos(\omega_i(t - t_0)) + \frac{\hat{p}_i(t_0)}{m_i \omega_i} \sin(\omega_i(t - t_0)) \right). \quad (5-49)$$

The above equations tell us that by tracing out the bath degrees of freedom we end up with a form of quantum Langevin equation. The dissipation is mediated through the memory kernel  $\gamma(t)$ , introducing a non-Markovianity in the particle's dynamics. Moreover, the particle is driven by a force proportional

to the particle's initial position, and by an external force  $\hat{f}(t)$  that only depends on the heat bath initial quadratures, whose unknown initial conditions gives rise to the stochasticity of this term in the classical regime [224].

In the following, we will use the continuous limit of  $N \rightarrow \infty$  as to obtain the irreversible properties of the heat bath, following the prescription outlined in [220]

$$\sum_{j=1}^N \frac{c_j^2}{m_j \omega_j^2}(\dots) \rightarrow \int_0^{\bar{\omega}} \frac{c(\omega)^2}{m(\omega) \omega^2}(\dots) \frac{dn}{d\omega} d\omega = \frac{2M\gamma}{\pi} \int_0^{\bar{\omega}} (\dots) d\omega \quad (5-50)$$

where  $dn/d\omega$  is the oscillator density,  $\bar{\omega}$  is the frequency cutoff of the reservoir oscillator spectrum and  $\gamma$  is the damping amplitude. Thus, in this limit, the memory kernel reduces to

$$\gamma(t) = \frac{2M\gamma}{\pi} \int_0^{\bar{\omega}} \cos(\omega t) d\omega. \quad (5-51)$$

Formally, we can get rid of the non-Markovianity by assuming an infinite cutoff frequency for the heat bath and using the following property

$$\delta(t - t') = \frac{1}{\pi} \int_0^{\infty} \cos(\omega(t - t')) d\omega, \quad (5-52)$$

such that the memory kernel becomes delta-correlated

$$\gamma(t) \rightarrow 2M\gamma\delta(t). \quad (5-53)$$

where  $\gamma \in \mathbb{R}$  is a free constant in this model, which we will better define in Section 5.3.

By further setting  $t_0 \rightarrow -\infty$ , in such a way that the term proportional to  $\hat{Q}(t_0)$  dies out, the QLEs for the particle transform into:

$$\begin{aligned} \dot{\hat{Q}}(t) &= \frac{1}{M} \hat{P}(t) \\ \dot{\hat{P}}(t) &= \frac{i}{\hbar} [V(\hat{Q}), \hat{P}(t)] - M\gamma\dot{\hat{Q}}(t) + \hat{f}'(t) \end{aligned}$$

Finally, as we are interested in applications to levitated NPs, we set  $V$  to be an harmonic potential,  $V(\hat{Q}) \equiv \frac{M\Omega^2}{2} \hat{Q}^2$ . For simplicity, we also move to dimensionless quadratures  $\hat{q} = \sqrt{\frac{2M\Omega}{\hbar}} \hat{Q}$  and  $\hat{p} = \sqrt{\frac{2}{\hbar M\Omega}} \hat{P}$  such that the QLEs simplify to

$$\dot{\hat{q}}(t) = +\Omega\hat{p}(t) \quad (5-54)$$

$$\dot{\hat{p}}(t) = -\Omega\hat{q}(t) - \gamma\hat{p}(t) + \hat{f}(t) \quad (5-55)$$

where we rescaled the external force:  $\hat{f}(t) = \sqrt{\frac{2}{\hbar M \Omega}} \hat{f}'(t)$ .

Let us now take some time to study the nature of the external force  $\hat{f}(t)$  when each mode of the heat bath is in a thermal state at temperature  $T_{\text{th}}$  with occupation number  $\bar{n}_{\text{th},j} = 1 / [\exp(\frac{\hbar \omega_j}{k_B T_{\text{th}}}) - 1]$ ,  $k_B$  is the Boltzmann constant.

It is straightforward to verify that the external force has zero mean value,  $\langle \hat{f}(t) \rangle = 0$ . Moreover, in the continuous limit, its correlation function becomes

$$\langle \hat{f}(t) \hat{f}(t') \rangle = \frac{2\gamma}{\pi \Omega} \int_0^{\bar{\omega}} \omega \cos(\omega(t - t')) \coth\left(\frac{\hbar \omega}{2k_B T_{\text{th}}}\right) - i\omega \sin(\omega(t - t')) d\omega,$$

which can be recast in a more compact form as [34, 41]

$$\langle \hat{f}(t) \hat{f}(t') \rangle = \frac{2\gamma}{\pi \Omega} \int_0^{\bar{\omega}} e^{-i\omega(t-t')} S_{\text{th}}(\omega) d\omega, \quad (5-56)$$

where  $S_{\text{th}}(\omega) \equiv \omega [\coth(\frac{\hbar \omega}{2k_B T_{\text{th}}}) + 1]$  is the thermal noise spectrum [41]. We observe that from the form of this correlator, the stochastic noise automatically satisfies the fluctuation-dissipation relation [39, 221].

This force can be easily reduced to the a standard white gaussian noise if we consider an infinite cutoff frequency,  $\bar{\omega} \rightarrow \infty$ , and move to the high-temperature limit,  $k_B T_{\text{th}} \gg \hbar \Omega$ . This is a realistic limit as current experimental implementations with levitated NP usually have mechanical frequencies in the order of hundreds of kilohertz [15, 48, 55] which translates into minuscule lower bounds for the heat bath's temperature; for example with  $\Omega = 100 \text{ kHz}$ , we would need the environmental temperature to obey  $T_{\text{th}} \gg 4.8 \mu\text{K}$ , which is safely guaranteed. Therefore, in this regime, the correlation function simplifies to

$$\langle \hat{f}(t) \hat{f}(t') \rangle = 2\gamma(2\bar{n}_{\text{th}} + 1)\delta(t - t').$$

where  $\bar{n}_{\text{th}} = [1 - \exp(\hbar \Omega / (k_B T_{\text{th}}))]^{-1}$  is the average thermal occupation number of each mode of the heat bath and  $2\bar{n}_{\text{th}} + 1 \approx 2k_B T_{\text{th}} / (\hbar \Omega)$  in the high-temperature limit.

As a final remark, we note that the commutator at different times for the external stochastic force is

$$[\hat{f}(t), \hat{f}(t')] = -2i \frac{2\gamma}{\pi \Omega} \int_0^{\bar{\omega}} \omega \sin(\omega(t - t')) d\omega = 2i \text{Im} \left( \langle \hat{f}(t) \hat{f}(t') \rangle \right). \quad (5-57)$$

### 5.3

#### Decoherence mechanisms

In this Chapter, we consider two major forms of decoherence/heating for the nanoparticles: thermal decoherence from the collisions with the environmental gas surrounding each NP and recoil heating as each NP incoherently scatters light from its tweezer into free space.

For pressures below 10 mbar, the regime which current experiments with CS interactions operate, the residual environmental gas damping on an optically levitated NP is linear in the gas pressure  $p_{\text{gas}}$ , following [22, 48]

$$\gamma \approx 15.8 \frac{R^2 p_{\text{gas}}}{m v_{\text{gas}}} \quad (5-58)$$

where  $v_{\text{gas}} = \sqrt{3k_B T_{\text{gas}}/m_{\text{gas}}}$  is the root-mean-square velocity of a gas molecule with mass  $m_{\text{gas}}$  at temperature  $T_{\text{gas}}$ ;  $m$  and  $R$  are the NP's mass and radius, respectively. The associated thermal decoherence rate from the collisions with the residual gas then becomes [22]

$$\Gamma_{\text{gas}} = \gamma \bar{n}_{\text{th}}.$$

The recoil heating rate arising from the photon recoil as a NP incoherently scatters photons from the trapping tweezer into free space reads [22]

$$\Gamma_{\text{recoil}} = \frac{1}{5} \frac{P_{\text{scatt}}}{mc^2} \frac{\omega_t}{\omega} \quad (5-59)$$

where  $c$  is the speed of light and  $P_{\text{scatt}} = I_0 \sigma_{\text{scatt}}$  is the scattered power of a NP from its tweezer;  $I_0 = 2P_t/(\pi w_0^2)$  is the tweezer's intensity at its NP's mean position and  $\sigma_{\text{scatt}} = |\alpha|^2 k_t^4 / (6\pi \epsilon_0^2)$  the scattering cross section of the NP.

### 5.4

#### Coherent Scattering-mediated correlations between levitated nanospheres

In this Section we present the results of our work [52], where we investigate how the coherent scattering interaction between a single cavity mode and an arbitrary number of levitated nanoparticles can give rise to quantum correlations among the various partitions of the system even at room temperature. For high-vacuum environments ( $p < 10^{-9}$  mbar), it has been shown that CS mediated mechanical entanglement can resist photon scattering decoherence [50] and in moderate vacuum ( $p \sim 10^{-6}$  mbar) steady state entanglement is only possible at low environment temperatures around  $T_{\text{env},j} \approx 15$  K [51]. In the latter regime, the crucial question of whether mechanical entanglement could exist for realistic environmental temperatures before the system achieves its steady state remained open.

The system under study here is the same examined in Section 5.1, depicted in Figure 5.1; we follow the same notation of that Section.

### 5.4.1

#### Quantum dynamics

Following our discussion on Section 5.1.1, we consider that the OTs position the NPs on the cavity nodes such that the Hamiltonian that dictates the closed unitary dynamics of the system is

$$\hat{H}/\hbar \approx \Delta \hat{a}^\dagger \hat{a} + \sum_{j=1}^N \omega_j \hat{b}_j^\dagger \hat{b}_j + \sum_{j=1}^N g_j (\hat{a}^\dagger + \hat{a})(\hat{b}_j^\dagger + \hat{b}_j). \quad (5-60)$$

Furthermore, we follow the formalism presented in Section 5.2 to model the open quantum dynamics of this system through a set of quantum Langevin equations [33, 39, 40, 150, 221]. We consider that one of the cavity mirrors is not perfect, resulting in a finite cavity linewidth  $\kappa$  and allowing photon exchange between the cavity field and the external free field [219], see Section 5.2.1. Moreover, each NP is considered to be in contact with its own thermal bath, at temperature  $T_{\text{env},j}$ , see Section 5.2.2. As a consequence of the spaced apart tweezers and moderate vacuum, we model the heat baths to be independent of one another.

We use the following notation henceforth: the dimensionless position and momentum quadratures for each particle  $\hat{x}_j = \hat{b}_j^\dagger + \hat{b}_j$ ,  $\hat{p}_j = i(\hat{b}_j^\dagger - \hat{b}_j)$ , and for the cavity field  $\hat{Q} = \hat{a}^\dagger + \hat{a}$ ,  $\hat{P} = i(\hat{a}^\dagger - \hat{a})$ , such that the quantum Langevin equations read

$$\dot{\hat{Q}} = +\Delta \hat{P} - \frac{\kappa}{2} \hat{Q} + \sqrt{\kappa} \hat{x}_{\text{in}}, \quad (5-61)$$

$$\dot{\hat{P}} = -\Delta \hat{Q} - \frac{\kappa}{2} \hat{P} + \sqrt{\kappa} \hat{p}_{\text{in}} - \sum_{j=1}^N 2g_j \hat{x}_j, \quad (5-62)$$

$$\dot{\hat{x}}_j = +\omega_j \hat{p}_j, \quad (5-63)$$

$$\dot{\hat{p}}_j = -\omega_j \hat{x}_j - \gamma_j \hat{p}_j + \hat{f}_j - 2g_j \hat{Q}, \quad (5-64)$$

where  $\hat{x}_{\text{in}} = \hat{a}_{\text{in}}^\dagger + \hat{a}_{\text{in}}$ ,  $\hat{p}_{\text{in}} = i(\hat{a}_{\text{in}}^\dagger - \hat{a}_{\text{in}})$  are the zero-averaged delta-correlated optical input noise terms satisfying  $\langle \hat{a}_{\text{in}}(t) \hat{a}_{\text{in}}^\dagger(t') \rangle = \delta(t - t')$  [219].  $\gamma_j$  is the damping rate for the  $j$ -th NP, which is under the influence of zero-averaged stochastic thermal noise  $\hat{f}_j$  [220] with correlation functions given by

$$\langle \hat{f}_j(t) \hat{f}_k(t') \rangle = \frac{2\gamma_j}{\omega_j} \int_0^{\bar{\omega}_j} e^{-i\omega(t-t')} \omega \left[ \coth \left( \frac{\hbar\omega}{2k_B T_{\text{env},j}} \right) + 1 \right] \frac{d\omega}{\pi} \delta_{j,k}$$



Here, the reservoir cut-off frequency is  $\bar{\omega}_j$ , and  $k_B$  denotes the Boltzmann constant. Following our discussion in Section 5.2.2 for the high-temperature regime,  $k_B T_{\text{env},j} \gg \hbar\omega_j$ , this thermal noise becomes delta-correlated  $\langle \hat{f}_j(t) \hat{f}_k(t') \rangle \approx 2\gamma_j(2\bar{n}_{\text{th},j} + 1) \delta(t - t') \delta_{j,k}$  [39, 220, 221], where  $\bar{n}_{\text{th},j} \approx k_B T_{\text{env},j} / (\hbar\omega_j)$  is the average thermal occupation number of each mode of the  $j$ -th heat bath.

We are interested in the case where the  $j$ -th NP is initially in a thermal state at temperature  $T_j$  with occupation number  $\bar{n}_{0,j}$  and the cavity field starts in the vacuum state. The linear nature of the Langevin equations preserves the Gaussianity of the initial states, allowing the use of the Gaussian quantum information toolbox [194]. In particular, since Gaussian quantum states are completely characterized by their first and second moments, we can focus directly on the dynamics of the covariance matrix. See Appendix B for an introduction to the structure of Gaussian states and definitions of useful quantities used in remaining of this Chapter such as the logarithmic negativity, von Neumann entropy and mutual information.

Note that first moments can be easily calculated once we recast the Langevin equations in a more compact form,

$$\dot{\hat{\mathbf{X}}}(t) = A\hat{\mathbf{X}}(t) + \hat{\mathbf{N}}(t), \quad (5-65)$$

where  $\hat{\mathbf{X}} = (\hat{Q}, \hat{P}, \hat{x}_1, \hat{p}_1, \dots)^T$  is the quadrature vector,  $\hat{\mathbf{N}} = (\sqrt{\kappa}\hat{x}_{\text{in}}, \sqrt{\kappa}\hat{p}_{\text{in}}, 0, \hat{f}_1, \dots)^T$  is the input noise vector and  $A$  is the *drift* matrix.

Consider the formal expression for the quadratures

$$\hat{\mathbf{X}}(t) = e^{A(t-t_0)} \hat{\mathbf{X}}(t_0) + \int_{t_0}^t e^{A(t-s)} \hat{\mathbf{N}}(s) ds. \quad (5-66)$$

Equipped with the fact that the initial states and input noise have zero average, direct calculation shows that  $\langle \hat{\mathbf{X}}(t) \rangle = \mathbf{0}$  for all times.

The second moments of the system can be represented by the covariance matrix (CM), with components defined as  $V_{i,j} = \frac{1}{2} \langle \hat{X}_i \hat{X}_j + \hat{X}_j \hat{X}_i \rangle$ . Using Equation (5-66), we see that the CM satisfies the Lyapunov equation

$$\dot{V} = AV + VA^T + D, \quad (5-67)$$

where  $D_{l,k} \delta(t - t') \equiv \frac{1}{2} \langle \hat{N}_l(t) \hat{N}_k(t') + \hat{N}_k(t') \hat{N}_l(t) \rangle$ , such that  $D = \text{diag}(\kappa, \kappa, 0, 2\gamma_1(2\bar{n}_{\text{th},1} + 1), 0, 2\gamma_2(2\bar{n}_{\text{th},2} + 1), \dots)$  is the *diffusion* matrix. We can use the above dynamical equations to study entanglement within our system both in the closed and open regimes.

### 5.4.2

#### Unitary Entanglement Dynamics

It is expected that the unitary dynamics generated by (5-60) exhibits entanglement between the various mechanical and optical modes in the system. To gain some analytical insight into this entanglement generation consider the formal limit  $\omega_j \ll \Delta$ . For  $N = 2$  NPs the Hamiltonian reduces to,

$$\hat{H}_0/\hbar \approx \Delta \hat{a}^\dagger \hat{a} + g(\hat{a}^\dagger + \hat{a})(\hat{x}_1 + \hat{x}_2), \quad (5-68)$$

where we assume for simplicity that both NPs couple equally to the optical mode,  $g_1 = g_2 \equiv g$ . This simplified Hamiltonian can be exponentiated exactly using the same techniques employed in calculating the unitary evolution operator for a dispersive optomechanical system [157] as discussed in Sections 4.2 4.3. The unitary time evolution operator for this case is  $U_0(t) = \exp(-i\hat{H}_0 t/\hbar)$ , which reads

$$\hat{U}_0(t) = e^{-i\hat{a}^\dagger \hat{a} \Delta t} e^{(\hat{a}\eta(t) - \hat{a}^\dagger \eta(t)^*)(g/\Delta)(\hat{x}_1 + \hat{x}_2)} e^{-i(g/\Delta)^2(\hat{x}_1 + \hat{x}_2)^2 \sin(\Delta t)} e^{ig^2(\hat{x}_1 - \hat{x}_2)^2 \Delta t}, \quad (5-69)$$

where  $\eta(t) = 1 - e^{-i\Delta t}$ . Note that the last two exponential terms contain effective interactions among the NPs, given by products of the  $\hat{x}_1, \hat{x}_2$  terms. The presence of these optically mediated interactions lead to generation of entanglement between the NPs within this simplified approximation. Moreover, the the fact that the unitary operator is written in terms of periodic functions hints at entanglement death and revivals.

In order to verify the entanglement generation in this regime, we numerically solve the Lyapunov equation in the absence of noise and losses. Figure 5.5 shows numerical plots of the Logarithmic negativity (LN) and von Neumann entropies for the various partitions of a system comprised of 2 NPs and one optical mode, all initially in the ground state. The parameters used for this simulations are shown in Table 5.2, except for  $\Delta = 10 \times \omega_j$ ,  $\kappa = 0$  and  $\gamma_j = 0 \forall j$ . From now on, unless explicitly stated otherwise, all NPs are taken to be identical and Table 5.2 dictates all the parameters considered in the simulations throughout the rest of this Chapter; see Section 5.4.4.

We observe that in the unitary CS scenario cyclic entanglement birth and death are present, analogous to the dispersive optomechanical case [157]. Moreover, while the entropy of each bipartition is synchronized, the LN in the mechanical bipartition only achieves local maxima when the optomechanical LN are at their local minima. This points towards the idea that under certain circumstances entanglement can flow through different partitions of the system,

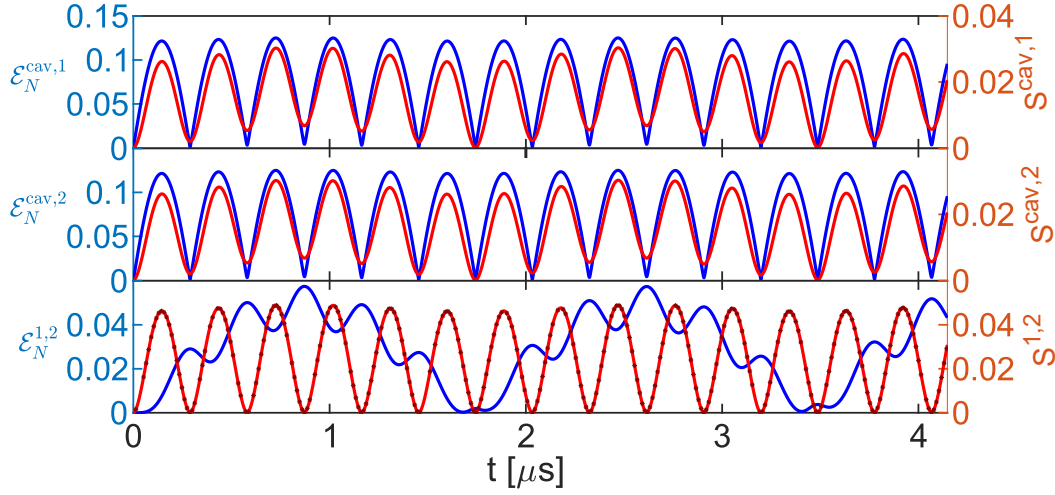


Figure 5.5: Simulation with  $N = 2$  identical levitated NPs initially in the vacuum state following a closed unitary dynamics. Time evolution of logarithmic negativity (blue) and von Neumann entropy (red) for each bipartition of the system. In this simulation, we considered  $\Delta = 10 \times \omega_j$ , ensuring the formal limit  $\omega_j \ll \Delta$  while  $\kappa = 0$  and  $\gamma_j = 0 \forall j$ , making the system closed. Due to instabilities in the numerical simulation of the von Neumann entropy in the mechanical bipartition, we show both the calculated values (dark red points) and smoothed trace (light red line).

in this case back and forth between the optical and mechanical modes. It is also instructive to consider the optical field as an environment for the two NPs. Under this point of view, we can understand entanglement and entropy oscillations as a consequence of the non-Markovian nature of the subsystems' evolution.

### 5.4.3

#### Entanglement in a noisy environment

In any realistic experimental scenario the system under study is always interacting with its environment. For this reason it is important to study how the unitary entanglement dynamics is modified when the optomechanical system is placed in contact with uncontrolled external degrees of freedom.

For a start, consider the experimentally challenging scenario where each NP begins in the ground state and in contact with a cryogenic environment at temperature 130 K [15]. This setting allows for entanglement of a large number of NPs. Figure 5.6 shows the time evolving LN as a function of the number of identical NPs in the cavity. We note that in this case the LN is symmetric over all possible mechanical bipartitions provided the particle parameters are identical, e.g. mass, coupling strength, bath temperature. As the number of NPs in the cavity is increased we observe the maximum LN decreases: the additional NPs act as an environment for the bipartite subsystem. This can

also be understood as a consequence of monogamy of entanglement.

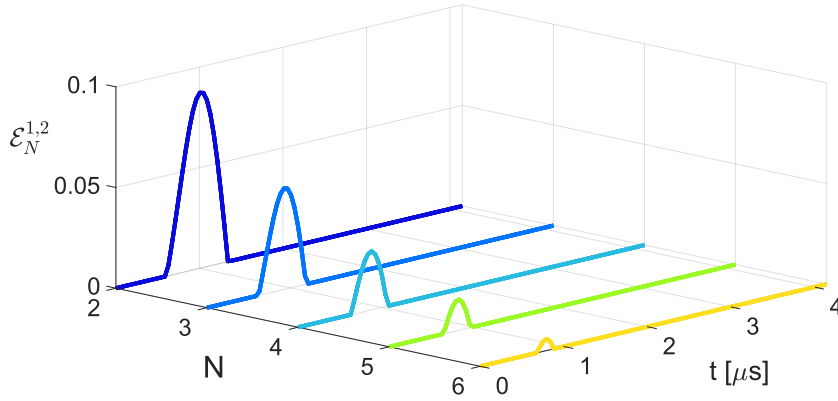


Figure 5.6: Time evolving LN between a pair of particles for an increasing number of particles sharing the same cavity. Every NP is considered to be in the ground state and in contact with a cryogenic environment at temperature  $T_{\text{env},j} = 130$  K, resulting in  $\gamma_j = 0.957$  mHz.

In contrast to the result of Section 5.4.2, we observe that quantum correlations between mechanical modes are only non-zero for a brief interval of time, while their oscillating nature is washed out by interactions with the environment. Since the environment is traced out and treated effectively as damping and stochastic forces in a Markovian approximation, quantum correlations between the system's degrees of freedom are never recovered [225]. Moreover, as we consider a higher number of interacting NPs, both the maximum of the LN trace and the time interval during which it is non-zero decreases, i.e., the entanglement *dilutes* over the system due to monogamy constraints.

In the following we restrict our attention to a system comprised of  $N = 2$  identical levitated NPs. This allows to study the system in a setting where entanglement generation is maximized. The particles are considered to be cooled to a thermal state at temperature  $4.6 \mu\text{K}$ , close to temperatures achieved in current optomechanical experiments [15]. We consider the thermal environment to be cryogenic, at 130 K. In Figure 5.7(a), we illustrate traces of the LN and entropy evolving in time for each possible bipartition. Once again, we observe loss of entanglement oscillations for the mechanical modes due to interactions with the external environment. Note, however, that the optomechanical entanglement persists over some oscillations before dying out in the steady state at long times (not shown). Note also that the non-Markovian features of the evolution such as oscillations of entropy, albeit present, are strongly attenuated due to the Markovian nature of environmental interactions.

We can speak more broadly about the correlations within the system employing the mutual information, a measure of the total classical and quan-

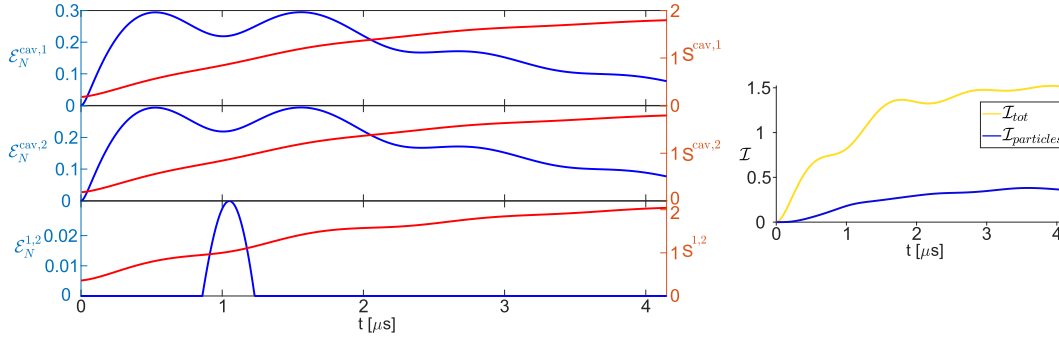


Figure 5.7: Simulation with  $N = 2$  identical levitated NPs with initial temperature  $T_j = 4.6 \mu\text{K}$  in contact with a cryogenic environment at  $T_{\text{env},j} = 130 \text{ K}$ ,  $\gamma_j = 0.957 \text{ mHz}$ . (a) Time evolution of logarithmic negativity (blue) and von Neumann entropy (red) for each bipartition of the system. (b) Mutual information for the total system (yellow) and subsystem with only the levitated NPs (blue) evolving in time.

tum correlations [226]. See Appendix B for details on the definition. In Figure 5.7(b), we plot the time evolving mutual information for the total system,  $\mathcal{I}_{\text{tot}}$ , and the reduced system composed solely of the NPs,  $\mathcal{I}_{\text{particles}}$ . The parties are initially uncorrelated as expected from the form of the separable states at  $t = 0$ . It later becomes correlated during the system's coherence time, as defined in Section 5.4.4. In the reduced mechanical bipartition, CS-mediated correlations are generated before quantum entanglement comes into play and persists after entanglement death. As a final remark, we have solved the Lyapunov equation for the steady state, given by  $AV + VA^T + D = 0$ , and find that  $\mathcal{E}_N^{j,k} = 0 \forall j, k$ . This is consistent with previous results in the literature [51]. The steady state, however, displays non-zero total mutual information  $\mathcal{I}_{\text{tot}} \simeq 15.314$  and  $\mathcal{I}_{\text{particles}} \simeq 14.223$  meaning that although the LN cannot detect steady state entanglement, general correlations among subsystems due to the CS interaction are present.

So far, our focus has been centered on how coherent scattering-mediated entanglement appears and evolves in time. We now shift our attention to the LN's dependency on experimentally controlled parameters in the search for a configuration allowing room temperature mechanical entanglement. An in depth discussion of the experimental feasibility of the parameters used in the simulations is presented in Section 5.4.4.

Figure 5.8 shows the maximum of the LN between the two NPs within the coherence time of the system,  $\tau \simeq 4.15 \mu\text{s}$  as quantified in Section 5.4.4, for different values of initial temperature and occupation number in the presence of an environment at room temperature (300 K). We can immediately see that in a realistic scenario mechanical entanglement would only occur for

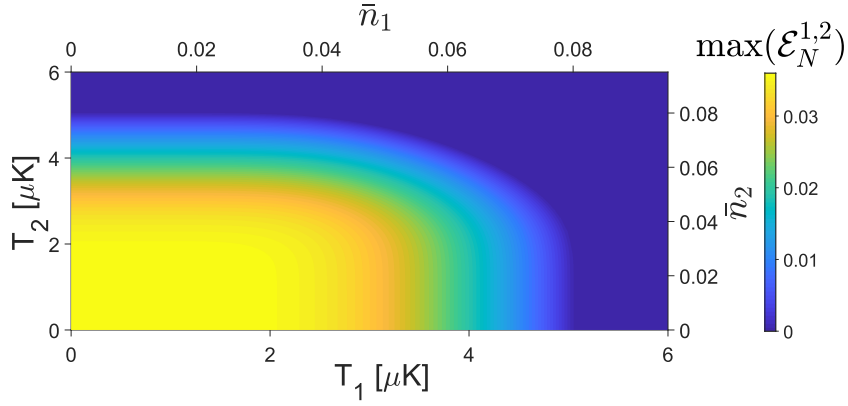


Figure 5.8: Maximum of the logarithmic negativity within the system's coherence time for two particles as a function of their initial temperatures. Notice that we need highly cooled particles to generate mechanical entanglement.

extremely cool particles. For  $T_j > 5 \mu\text{K}$  we see the LN vanishes, and we note that such temperature corresponds to one tenth of the occupation number achieved by [15], implying that experimental verification of coherent scattering generated entanglement at room temperature is a challenging achievement.

This difficulty could be partially circumvented by increasing the CS coupling. In Figure 5.9, we show the time-dependent LN as a function of the optomechanical coupling strength for an initial NP temperature of  $T_j \sim 4.6 \mu\text{K}$  (occupation number  $\bar{n}_{0,j} = 0.0430$ ). We readily see that entanglement generation depends significantly on the optomechanical coupling strength. Current state-of-the-art CS implementations achieve  $g_j/\omega_j \sim 0.2$  [15], below the region in which entanglement and its revivals are present. We note that couplings as high as  $2\pi \times 110 \text{ kHz}$  could be achieved by increasing the NP radius and using higher power tweezers; in such regime, where  $g_j/\omega_j \sim 0.36$ , entanglement starts to appear in the system. For higher values of optomechanical coupling, we enter the strong coupling regime  $g_j \geq \omega_j$  where birth, death and revivals of entanglement occur.

As a concluding remark, we note that another interesting feature of the CS interaction is the generation of mechanical squeezing during the system's time evolution. Generation of squeezing using the CS Hamiltonian for a single particle has been shown in [49]. We are able to show that squeezing is also generated if more than one particle is present in the cavity. As an example, consider the case of two NPs in the cavity initially in a thermal state. Figure 5.10 displays the Wigner function for a NP at different instants of time. As we consider identical NPs, their Wigner functions are also identical and only a single one is shown. We observe the generation of squeezing through the appearance of elliptical shapes of the Wigner distribution and the calculated lower than one squeezing degree  $\eta$ , defined as the ratio of the squeezed and

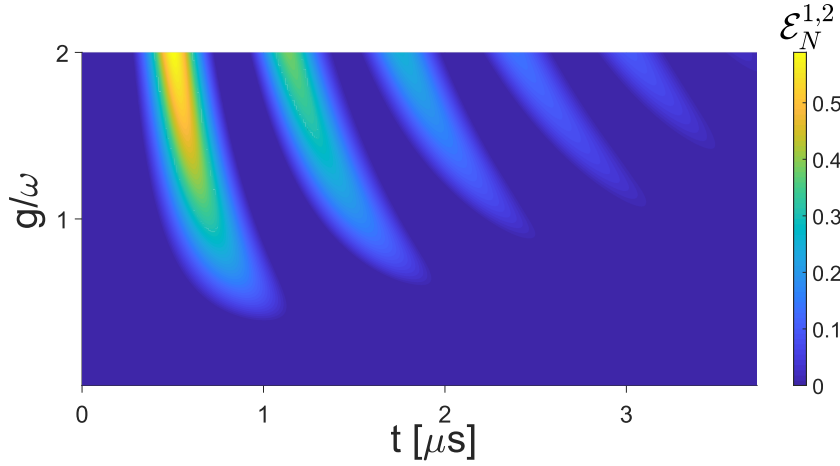


Figure 5.9: Time evolving logarithmic negativity for different coupling strengths,  $g_j = g$  for all  $j$ . Here we considered every NP starting in a thermal state at  $T_j \sim 4.6 \mu\text{K}$  (occupation number  $\bar{n}_{0,j} = 0.0430$ ). Observe that in the high coupling regime,  $g \sim \omega$ , entanglement birth, death and revivals are present.

the antisqueezed quadratures, see Appendix B. The squeezed Wigner function also rotates as a result of time evolution. The emergence of squeezing in multi-particle CS could find interesting applications in quantum metrology of feeble forces [10].

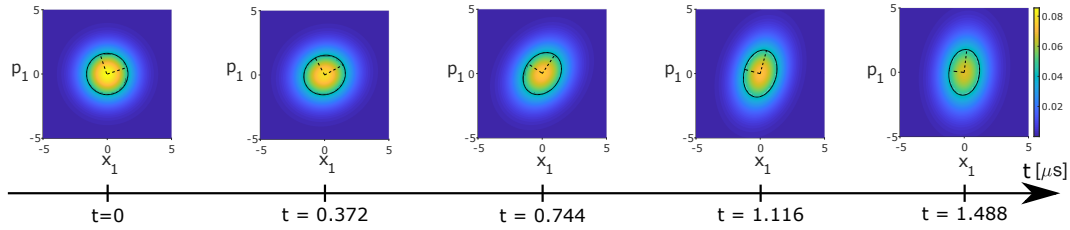


Figure 5.10: Time evolution of Wigner function for  $N = 2$  identical levitated NPs. As the particles are identical, they possess identical functions. Black dashed lines indicate the Wigner function semi-axes. Solid black lines denote contours at half of its maximum initial value. As the particles are initially in a thermal state the squeezing degree starts at  $\eta(0) = 1$  and becomes increasingly smaller as time progresses. The squeezing degree for each time stamp is respectively  $\eta = (1, 0.840, 0.609, 0.454, 0.440)$ ; see Appendix B.

#### 5.4.4

##### Experimental parameters

The parameters used in our simulations were adapted from Ref. [15]. There, a silica nanosphere (density of  $\text{SiO}_2$ :  $2200 \text{ kg/m}^3$  [54]) was trapped by an OT within a high-finesse Fabry-Pérot cavity mounted in a vacuum chamber and cavity cooling through CS was performed to cool the CM of the NP into its

motional ground state. The parameters values of this experimental realization are presented in Table 5.1.

Table 5.1: Experimental parameters reported in Ref. [15]

Parameter	Unit	Value
Tweezer power $P_t$	mW	400
Tweezer wavelength $\lambda_t$	nm	1064
Tweezer waist (x axis)	$\mu\text{m}$	0.67
Tweezer waist (y axis)	$\mu\text{m}$	0.77
Trapping frequency $\omega_x$	kHz	$2\pi \times 305$
Cavity finesse $\mathcal{F}$	—	73,000
Cavity linewidth $\kappa$	kHz	$2\pi \times 193$
Cavity length $L$	mm	10.7
Cavity waist $w_0$	$\mu\text{m}$	41.1
Cavity-tweezer detuning $\Delta$	kHz	$2\pi \times 315$
Particle mass $m$	fg	2.83
Particle radius $R$	nm	71.5
Particle zero point fluctuation $x_{\text{ZPF}}$	pm	3.1
Vacuum chamber pressure $p_{\text{gas}}$	mbar	$10^{-6}$
Environmental temperature $T_{\text{gas}}$	K	300

In order to achieve a higher coupling between the NPs and the cavity field than previously reported in [56], we propose slight adaptations of the experimental parameters. First, we increase the radius of each NP to 100 nm; second we raise the power of each trapping tweezer to 1 W and consider a Gaussian beam waist of  $w_{0,j} = 0.852 \mu\text{m}$ , such that the trapping frequency remains approximately the same  $\omega_j \approx 2\pi \times 305 \text{ kHz}$ . Table 5.2 shows the resulting proposed parameters. Unless explicitly stated otherwise, these are the values considered in the simulations throughout this Section with all NPs identical to each other.

Table 5.2: Parameter values used in this Chapter

Parameter	Unit	Value
Mechanical natural frequency $\omega$	kHz	$2\pi \times 305.4$
Cavity-tweezer detuning $\Delta$	kHz	$2\pi \times 315.0$
CS coupling strength $g$	kHz	$2\pi \times 109.2$
Cavity linewidth $\kappa$	kHz	$2\pi \times 193.0$
Damping coefficient $\gamma$	mHz	$2\pi \times 0.630$
Particle initial temperature $T_0$	$\mu\text{K}$	12.2
Environmental gas temperature $T_{\text{gas}}$	K	300

These deviations from the parameters from [15] do not greatly affect the coherence time of the system, before a NP becomes populated by a single



phonon. This can be easily noticed by calculating the decoherence rates for the particles, as shown in Section 5.3.

In regards to the recoil heating, we will only consider contributions arising from the scattering of photons from the trapping tweezer of each particle. The reasoning for this simplification is twofold. First, as the cavity is not actively driven, its field intensity is much smaller than each tweezer intensity [218], diminishing its contribution. Secondly, as we are considering non-overlapping tweezers, the intensity of the  $j$ -th OT on the  $n$ -th NP,  $n \neq j$ , should be negligible and, thus, disregarded. For simplicity, we may consider identical environments surrounding each NP as the residual gas and temperature should a priori be the same everywhere inside the vacuum chamber, resulting in a common thermal decoherence rate  $\Gamma_{\text{gas}} \forall j$ . Furthermore, for the sake of brevity, we can make the recoil heating rate  $\Gamma_{\text{recoil}}$  approximately equal for all particles if they are of the same material and size, and the tweezers have approximately the same intensity at their focus.

Ref. [15] observed  $\Gamma_{\text{gas}} = 2\pi \times 16.1 \text{ kHz}$  and  $\Gamma_{\text{recoil}} = 2\pi \times 6 \text{ kHz}$  resulting in a coherence time corresponding to approximately 15 oscillations. Considering particles of radii  $R = 100 \text{ nm}$  results in a greater scattering cross section for the tweezer's photons and a inversion of the dominant decoherence mechanism as now recoil heating  $\Gamma_{\text{recoil}} = 2\pi \times 29.9 \text{ kHz}$  is greater the thermal heating  $\Gamma_{\text{gas}} = 2\pi \times 8.49 \text{ kHz}$ . One should note, though, that a bigger recoil heating rate still does not signify we must take into account interaction with the free field as the total expected coherence time  $\tau = 1/(\Gamma_{\text{recoil}} + \Gamma_{\text{gas}}) \simeq 4.15 \mu\text{s}$  now corresponds to 8 oscillations before a NP gains a single phonon [15].

## 5.5 Conclusion

When an optically levitated nanoparticle is placed inside an optical cavity, it only dispersively interacts with the cavity field if the tweezer's frequency is far detuned from the cavity's. However, if the these frequencies are close to each other, the particle can scatter the trapping beam's photons into the optical cavity, populating the latter and creating another form of optomechanical interaction between them, called coherent scattering. In this Chapter, we have studied the Coherent Scattering Hamiltonian of an arbitrary number of particles, describing  $N$  mechanical oscillators interacting with a single cavity mode.

The resulting unitary dynamics has been shown to generate quantum correlations in every bipartition of the system following cycles of entanglement birth and death. Moreover, within each revival, the Hamiltonian appears to

steam a flow of quantum correlations between the bipartitions, with mechanical entanglement maximized exactly when opto-mechanical entanglement is minimized.

In realistic experimental conditions, one has to consider the environmental effects on the system. Following [150, 219], we have demonstrated the quantum Langevin equations describing a mechanical system contact with an environmental heat bath and an optical cavity field interaction with the surrounding free electromagnetic field. Accordingly, we have show how to calculate the decoherence rates present in a Coherent Scattering system: thermal decoherence rate resulting the collisions with the environmental gas and recoil heating rate resulting from the incoherently scattering light into free space from a trapping tweezer.

For an open quantum dynamics, we have show that entanglement generation can still persist even in room temperature environments for some time within experimentally reasonable parameters. Although entanglement die out in the steady state [51], we have shown that general correlations are still present in the system. It would be interesting to study if more general quantum correlations, i.e. quantum discord, exist in the steady state and also quantify its dynamics alongside entanglement.

We also studied the dependence of mechanical entanglement on experimentally controlled parameters. We discovered that increasing the number of NPs interacting with the optical field *dilutes* the entanglement over the complete system and is detrimental to the creation of bipartite quantum correlations. Such correlations are expected to only appear when the particles are extremely cool, below the minimum occupancy achieved with current state-of-the-art technology [15]. The CS coupling strength also plays a significant role in entanglement generation, and revivals of entanglement only come into play in the high-coupling regime, where  $g_j > \omega_j$ . Squeezing is also generated by the many-particle CS Hamiltonian. In summary, the coherent scattering interaction propels optomechanics to the domain of complex quantum systems within realistic scenarios. It will be interesting to see what new experiments are enabled by this many-body mesoscopic quantum toolbox.

## 6 Outlook

We conclude this work by presenting a brief overview on the main topics discussed and an outlook on possible future research directions.

### Interferometry

In Chapter 2, we have shown describe the circulating electromagnetic field within any homodyne linear interferometer by finding an associated directed weighed graph. By weighting and counting every possible optical path, we also show how to extract the response factors for the interferometer's outputs and present examples of applications to cavity optomechanical setups with multiple dispersive elements.

In order to explore the full potential of the diagrammatic method developed in [58], it would be interesting to explore its connections with graph theory and make use of its theoretical tools to optimize the application of the so-called simplification rules, possibly extending it to more general heterodyne and/or nonlinear interferometers [227–229]. Moreover, it could be interesting to implement a software to transform some given optical configuration into an equivalent weighted directed graph and apply the simplification rules. This could allow us to solve complex interferometric devices, where even the application of the simplification rules can become cumbersome.

### Optical Tweezers

In Chapter 3, we studied the optical forces that arise on a dielectric particle when it is placed in contact with optical beams, both in the dipole regime and in the intermediary regime. Optical traps with two types of optical beams were analyzed: gaussian and bottle. The gaussian beam was shown to generate an effective 3D trapping potential close to its bright focus for particles with larger refractive index than its medium. An optical bottle beam was also defined, studied and shown to effectively trap particles with lower refractive index than its medium close to its dark focus. This form of optical beam

was also predicted to be capable of optically trapping living organisms whilst reducing laser damage, when compared to gaussian tweezer.

Furthermore, in the decoupling approximation, the optical bottle trap induces quartic and quadratic potential in the radial and axial directions, respectively, on the trapped particle. Recently, characterization of nonlinear forces in optical tweezers through the power spectral density of trapped particle has been analyzed in a perturbative scheme [230]. It would be interesting to envision an experimental procedure that could be able to identify non-harmonic forces and measure its strength.

Structured light beam could also open the doors to go beyond the gaussian optomechanics studied in Chapter 5. As in Chapter 4, where gaussianity was lost due to the form of the dispersive interaction with the cavity field, non-harmonic forces from the optical tweezer alone could prepare an trapped particle in a non-gaussian. More so, one could envision an optical beam to be in a non-gaussian quantum state and transfer it to the trapped particle's motional state [231].

## Quantum Optomechanics

Finally, in Chapters 4 and 5, we examined how the different light-matter interactions arise in various quantum cavity optomechanical experiments. The entanglement generation and subsequent dynamics was studied for these systems following both closed and open dynamics.

In Chapter 4, when considering the dispersive interaction, we have seen how entanglement emerges between optical modes that never directly interact in a closed dynamics. The appearance of such entanglement evidences the nonclassicality of the mechanical oscillator that mediates the indirect optical-optical interaction. We have also seen that a realistic implementation with ultracold atomic ensemble serving as the mediator could be possible with current technology.

Optomechanical setups can also be used to probe the possible nonclassical nature of the gravitational field. Recently, the passing of a gravitational wave through an optical cavity has been theoretically shown to give rise to a dispersive-like coupling between the optical and gravitational modes analogous to the one studied in Chapter 4 [232, 233]. In this setup the cavity mirrors are allowed to move when a gravitational wave passes by. Another interesting configuration inspired by the actual design of gravitational wave detectors is shown in Figure 6.1(a), where the end mirrors of a Michelson interferometer are allowed to move due to the passing of a + polarized gravitational wave

propagating orthogonally to the cavities' axes. This configuration follows the same Hamiltonian as discussed in Section 4.3 with the gravitational wave mode playing the role of the mediator of the indirect interaction responsible for generating entanglement between the optical modes. We have already seen that this is indeed an entangling Hamiltonian, however in this case the effect would be attenuated as the gravitational Kerr-like term will be approximately given by [232]

$$\exp\left[-i\frac{\hbar\omega_0}{E_{\text{pl}}}t\left(\hat{a}^\dagger\hat{a}-\hat{b}^\dagger\hat{b}\right)^2\right] \quad (6-1)$$

where  $\hat{a}$  and  $\hat{b}$  are the annihilation operators for the cavities labeled  $A$  and  $B$ , respectively, both with equal natural frequency  $\omega_0$ ; and  $E_{\text{pl}} = \sqrt{\hbar c^5/G}$  is the Planck energy with  $G$  the gravitational constant.

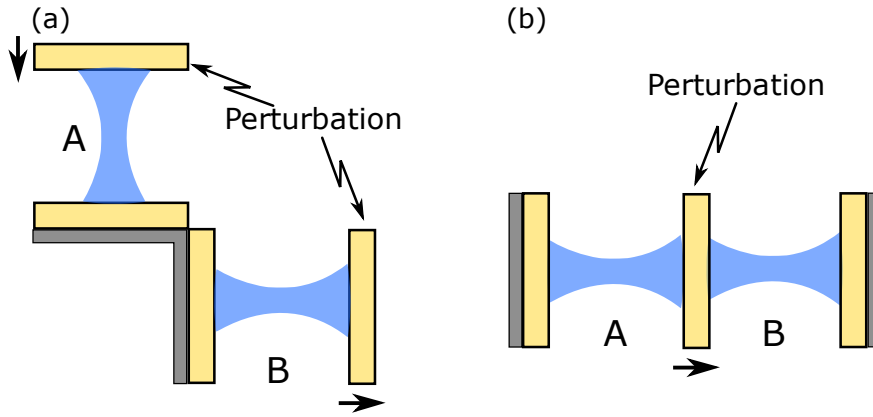


Figure 6.1: (a) Two optical cavities are placed orthogonal to each other, each possessing one fixed and one movable end-mirror. The fixed ones are connected in such way that they do not move in respect to one another. In this configuration, when a gravitational wave passes through this setup, one cavity would contract whilst the other one expands, generating an interaction between the gravitational field and the cavities' field [232,233] analogous to the one studied in Section 4.3. Image courtesy of Prof. Thiago Guerreiro, private communication.

Nevertheless, other optomechanical proposals which also rely on detecting quantum entanglement [208, 234], or on modifications of the Heisenberg uncertainty relation [235] have been put forward to observe the nonclassical nature of gravitational field in situations where the probed effect could in principle be observable. Applications to quantum sensing of gravitational waves [85] and gravitational accelerations [236, 237] have also been studied. We see that quantum optomechanics offers interesting possibilities regarding the intersection of gravity and quantum mechanics which could provide a compelling research direction.

In Chapter 5, we investigated the coherent scattering optomechanical interaction to nanospheres and how it gives rise to mechanical entanglement under a realistic experimental scenario. In order to do so, we modelled the open quantum dynamics of the system through a set of quantum Langevin equations and associated decoherence mechanisms. We also presented the results of [52], showing that generation of mechanical entanglement in a room temperature environment is possible within experimentally reasonable parameters.

Recently, the CS mechanism has been extended to nanorotors and shown to be able to perform simultaneous cooling of rotational and translational motion [18]. It could be interesting to research other geometries for the trapped mechanical object, e.g., an experimental setup where a tightly tensioned membrane could be optically trapped and its many vibrational modes could interact via CS with an optical cavity field.

It is also interesting to study coherent scattering setups under a thermodynamical point of view. For example, consider the case of two optically trapped particles initially in thermal states with different temperatures. We may set the tweezer trapping the more energetic particle red detuned and the colder particle's tweezer blue detuned relative to the cavity. This could be done such that the CS interaction will take energy away from the hot particle and give energy to the cold one. Thus, in this setup, the optical cavity mode effectively acts as a heat mediator.

## Bibliography

- [1] MILLEN, J.; STICKLER, B. A.. **Quantum experiments with microscale particles.** Contemporary Physics, p. 1–14, Dec. 2020.
- [2] FEYNMAN, R. P.. **Quantum mechanical computers.** Optics News, 11(2):11, Feb. 1985.
- [3] DEUTSCH, D.. **Quantum theory, the church–turing principle and the universal quantum computer.** Proceedings of the Royal Society of London. A. Mathematical and Physical Sciences, 400(1818):97–117, July 1985.
- [4] ARUTE, F.; ARYA, K.; BABBUSH, R. ; ET AL. **Quantum supremacy using a programmable superconducting processor.** Nature, 574(7779):505–510, Oct. 2019.
- [5] DEGEN, C. L.; REINHARD, F. ; CAPPELLARO, P.. **Quantum sensing.** Rev. Mod. Phys., 89:035002, Jul 2017.
- [6] TSE, M.; YU, H.; KIJBUNCHOO, N. ; ET AL. **Quantum-enhanced advanced ligo detectors in the era of gravitational-wave astronomy.** Phys. Rev. Lett., 123:231107, Dec 2019.
- [7] AASI, J.; ABADIE, J.; ABBOTT, B. P. ; ET AL. **Enhanced sensitivity of the LIGO gravitational wave detector by using squeezed states of light.** Nature Photonics, 7(8):613–619, July 2013.
- [8] CAVES, C. M.. **Quantum-mechanical noise in an interferometer.** Phys. Rev. D, 23:1693–1708, Apr 1981.
- [9] LEIBFRIED, D.. **Toward heisenberg-limited spectroscopy with multiparticle entangled states.** Science, 304(5676):1476–1478, June 2004.
- [10] WEISS, T.; RODA-LLORDES, M.; TORRONTGUI, E.; ASPELMEYER, M. ; ROMERO-ISART, O.. **Large quantum delocalization of a levitated nanoparticle using optimal control: Applications for force sensing and entangling via weak forces,** 2020.

- [11] GISIN, N.; RIBORDY, G.; TITTEL, W. ; ZBINDEN, H.. **Quantum cryptography**. Rev. Mod. Phys., 74:145–195, Mar 2002.
- [12] WEHNER, S.; ELKOUSS, D. ; HANSON, R.. **Quantum internet: A vision for the road ahead**. Science, 362(6412):eaam9288, Oct. 2018.
- [13] ASHKIN, A.; DZIEDZIC, J. M.; BJORKHOLM, J. E. ; CHU, S.. **Observation of a single-beam gradient force optical trap for dielectric particles**. Opt. Lett., 11(5):288, may 1986.
- [14] CHANG, D. E.; REGAL, C. A.; PAPP, S. B.; WILSON, D. J.; YE, J.; PAINTER, O.; KIMBLE, H. J. ; ZOLLER, P.. **Cavity opto-mechanics using an optically levitated nanosphere**. Proc. Natl. Acad. Sci. U.S.A., 107(3):1005–1010, dec 2009.
- [15] DELIĆ, U.; REISENBAUER, M.; DARE, K.; GRASS, D.; VULETIĆ, V.; KIESEL, N. ; ASPELMEYER, M.. **Cooling of a levitated nanoparticle to the motional quantum ground state**. Science, 367(6480):892–895, 2020.
- [16] MAGRINI, L.; ROSENZWEIG, P.; BACH, C.; DEUTSCHMANN-OLEK, A.; HOFER, S. G.; HONG, S.; KIESEL, N.; KUGI, A. ; ASPELMEYER, M.. **Optimal quantum control of mechanical motion at room temperature: ground-state cooling**, 2020.
- [17] KUHN, S.; KOSLOFF, A.; STICKLER, B. A.; PATOLSKY, F.; HORNBERGER, K.; ARNDT, M. ; MILLEN, J.. **Full rotational control of levitated silicon nanorods**. Optica, 4(3):356, Mar. 2017.
- [18] SCHÄFER, J.; RUDOLPH, H.; HORNBERGER, K. ; STICKLER, B. A.. **Cooling nanorotors by elliptic coherent scattering**, 2020.
- [19] STICKLER, B. A.; HORNBERGER, K. ; KIM, M. S.. **Quantum rotations of nanoparticles**, 2021.
- [20] GIESELER, J.; DEUTSCH, B.; QUIDANT, R. ; NOVOTNY, L.. **Subkelvin parametric feedback cooling of a laser-trapped nanoparticle**. Phys. Rev. Lett., 109:103603, Sep 2012.
- [21] MILLEN, J.; MONTEIRO, T. S.; PETTIT, R. ; VAMIVAKAS, A. N.. **Optomechanics with levitated particles**. Reports on Progress in Physics, 83(2):026401, Jan. 2020.



- [22] JAIN, V.; GIESELER, J.; MORITZ, C.; DELLAGO, C.; QUIDANT, R. ; NOVOTNY, L.. **Direct measurement of photon recoil from a levitated nanoparticle.** *Phys. Rev. Lett.*, 116:243601, Jun 2016.
- [23] ASPELMEYER, M.; KIPPENBERG, T. J. ; MARQUARDT, F.. **Cavity optomechanics.** *Reviews of Modern Physics*, 86(4):1391–1452, Dec. 2014.
- [24] BROOKS, D. W. C.; BOTTER, T.; SCHREPPLER, S.; PURDY, T. P.; BRAHMS, N. ; STAMPER-KURN, D. M.. **Non-classical light generated by quantum-noise-driven cavity optomechanics.** *Nature*, 488(7412):476–480, aug 2012.
- [25] PURDY, T. P.; YU, P.-L.; PETERSON, R. W.; KAMPEL, N. S. ; REGAL, C. A.. **Strong optomechanical squeezing of light.** *Phys. Rev. X*, 3:031012, Sep 2013.
- [26] AGGARWAL, N.; CULLEN, T. J.; CRIPE, J.; COLE, G. D.; LANZA, R.; LIBSON, A.; FOLLMAN, D.; HEU, P.; CORBITT, T. ; MAVALVALA, N.. **Room-temperature optomechanical squeezing.** *Nature Physics*, 16(7):784–788, July 2020.
- [27] JÄHNE, K.; GENES, C.; HAMMERER, K.; WALLQUIST, M.; POLZIK, E. S. ; ZOLLER, P.. **Cavity-assisted squeezing of a mechanical oscillator.** *Phys. Rev. A*, 79:063819, Jun 2009.
- [28] XIONG, B.; LI, X.; CHAO, S.-L.; YANG, Z.; ZHANG, W.-Z.; ZHANG, W. ; ZHOU, L.. **Strong mechanical squeezing in an optomechanical system based on lyapunov control.** *Photonics Research*, 8(2):151, Jan. 2020.
- [29] LÜ, X.-Y.; LIAO, J.-Q.; TIAN, L. ; NORI, F.. **Steady-state mechanical squeezing in an optomechanical system via duffing nonlinearity.** *Phys. Rev. A*, 91:013834, Jan 2015.
- [30] CHEN, J.; ROSSI, M.; MASON, D. ; SCHLIESSER, A.. **Entanglement of propagating optical modes via a mechanical interface.** *Nat. Commun.*, 11(1):943, feb 2020.
- [31] RIEDINGER, R.; WALLUCKS, A.; MARINKOVIĆ, I.; LÖSCHNAUER, C.; ASPELMEYER, M.; HONG, S. ; GRÖBLACHER, S.. **Remote quantum entanglement between two micromechanical oscillators.** *Nature*, 556(7702):473–477, Apr 2018.

- [32] GUT, C.; WINKLER, K.; HOELSCHER-OBERMAIER, J.; HOFER, S. G.; NIA, R. M.; WALK, N.; STEFFENS, A.; EISERT, J.; WIECZOREK, W.; SLATER, J. A.; ASPELMEYER, M. ; HAMMERER, K.. **Stationary optomechanical entanglement between a mechanical oscillator and its measurement apparatus.** Phys. Rev. Research, 2:033244, Aug 2020.
- [33] VITALI, D.; GIGAN, S.; FERREIRA, A.; BÖHM, H. R.; TOMBESI, P.; GUERREIRO, A.; VEDRAL, V.; ZEILINGER, A. ; ASPELMEYER, M.. **Optomechanical entanglement between a movable mirror and a cavity field.** Phys. Rev. Lett., 98:030405, Jan 2007.
- [34] PATERNOSTRO, M.; VITALI, D.; GIGAN, S.; KIM, M. S.; BRUKNER, C.; EISERT, J. ; ASPELMEYER, M.. **Creating and probing multipartite macroscopic entanglement with light.** Phys. Rev. Lett., 99:250401, Dec 2007.
- [35] PALOMAKI, T. A.; TEUFEL, J. D.; SIMMONDS, R. W. ; LEHNERT, K. W.. **Entangling mechanical motion with microwave fields.** Science, 342(6159):710–713, Oct. 2013.
- [36] OCKELOEN-KORPPI, C. F.; DAMSKÄGG, E.; PIRKKALAINEN, J.-M.; ASJAD, M.; CLERK, A. A.; MASSEL, F.; WOOLLEY, M. J. ; SILLANPÄÄ, M. A.. **Stabilized entanglement of massive mechanical oscillators.** Nature, 556(7702):478–482, Apr 2018.
- [37] RIEDINGER, R.; HONG, S.; NORTE, R. A.; SLATER, J. A.; SHANG, J.; KRAUSE, A. G.; ANANT, V.; ASPELMEYER, M. ; GRÖBLACHER, S.. **Non-classical correlations between single photons and phonons from a mechanical oscillator.** Nature, 530(7590):313–316, Jan. 2016.
- [38] MANCINI, S.; VITALI, D. ; TOMBESI, P.. **Optomechanical cooling of a macroscopic oscillator by homodyne feedback.** Phys. Rev. Lett., 80:688–691, Jan 1998.
- [39] GENES, C.; VITALI, D.; TOMBESI, P.; GIGAN, S. ; ASPELMEYER, M.. **Ground-state cooling of a micromechanical oscillator: Comparing cold damping and cavity-assisted cooling schemes.** Phys. Rev. A, 77:033804, Mar 2008.
- [40] SOMMER, C.; GENES, C.. **Partial optomechanical refrigeration via multimode cold-damping feedback.** Physical Review Letters, 123(20), Nov. 2019.

- [41] SOMMER, C.; GHOSH, A. ; GENES, C.. **Multimode cold-damping optomechanics with delayed feedback.** Phys. Rev. Research, 2:033299, Aug 2020.
- [42] COHADON, P. F.; HEIDMANN, A. ; PINARD, M.. **Cooling of a mirror by radiation pressure.** Phys. Rev. Lett., 83:3174–3177, Oct 1999.
- [43] GIGAN, S.; BÖHM, H. R.; PATERNOSTRO, M.; BLASER, F.; LANGER, G.; HERTZBERG, J. B.; SCHWAB, K. C.; BÄUERLE, D.; ASPELMEYER, M. ; ZEILINGER, A.. **Self-cooling of a micromirror by radiation pressure.** Nature, 444(7115):67–70, Nov. 2006.
- [44] JAYICH, A. M.; SANKEY, J. C.; ZWICKL, B. M.; YANG, C.; THOMPSON, J. D.; GIRVIN, S. M.; CLERK, A. A.; MARQUARDT, F. ; HARRIS, J. G. E.. **Dispersive optomechanics: a membrane inside a cavity.** New Journal of Physics, 10(9):095008, sep 2008.
- [45] DE CUMIS, M. S.; FARSI, A.; MARINO, F.; D'ARRIGO, G.; MARIN, F.; CATALIOTTI, F. S. ; RIMINI, E.. **Radiation pressure excitation and cooling of a cryogenic micro-mechanical systems cavity.** Journal of Applied Physics, 106(1):013108, July 2009.
- [46] KIESEL, N.; BLASER, F.; DELIC, U.; GRASS, D.; KALTENBAEK, R. ; ASPELMEYER, M.. **Cavity cooling of an optically levitated submicron particle.** Proceedings of the National Academy of Sciences, 110(35):14180–14185, Aug. 2013.
- [47] CHAN, J.; ALEGRE, T. P. M.; SAFAVI-NAEINI, A. H.; HILL, J. T.; KRAUSE, A.; GRÖBLACHER, S.; ASPELMEYER, M. ; PAINTER, O.. **Laser cooling of a nanomechanical oscillator into its quantum ground state.** Nature, 478(7367):89–92, Oct. 2011.
- [48] DE LOS RÍOS SOMMER, A.; MEYER, N. ; QUIDANT, R.. **Strong optomechanical coupling at room temperature by coherent scattering.** Nature Communications, 12(1), Jan. 2021.
- [49] ČERNOTÍK, O. C. V.; FILIP, R.. **Strong mechanical squeezing for a levitated particle by coherent scattering.** Phys. Rev. Research, 2:013052, Jan 2020.
- [50] MARTINETZ, L.; HORNBERGER, K.; MILLEN, J.; KIM, M. S. ; STICKLER, B. A.. **Quantum electromechanics with levitated nanoparticles.** npj Quantum Information, 6(1), Dec. 2020.

- [51] CHAUHAN, A. K.; ČERNOTÍK, O. ; FILIP, R.. **Stationary gaussian entanglement between levitated nanoparticles.** New Journal of Physics, 22(12):123021, Dec. 2020.
- [52] BRANDÃO, I.; TANDEITNIK, D. ; GUERREIRO, T.. **Coherent scattering-mediated correlations between levitated nanospheres,** 2021.
- [53] VULETIĆ, V.; CHAN, H. W. ; BLACK, A. T.. **Three-dimensional cavity doppler cooling and cavity sideband cooling by coherent scattering.** Phys. Rev. A, 64:033405, Aug 2001.
- [54] GONZALEZ-BALLESTERO, C.; MAURER, P.; WINDEY, D.; NOVOTNY, L.; REIMANN, R. ; ROMERO-ISART, O.. **Theory for cavity cooling of levitated nanoparticles via coherent scattering: Master equation approach.** Physical Review A, 100(1), jul 2019.
- [55] WINDEY, D.; GONZALEZ-BALLESTERO, C.; MAURER, P.; NOVOTNY, L.; ROMERO-ISART, O. ; REIMANN, R.. **Cavity-based 3d cooling of a levitated nanoparticle via coherent scattering.** Phys. Rev. Lett., 122:123601, Mar 2019.
- [56] DELIĆ, U.; REISENBAUER, M.; GRASS, D.; KIESEL, N.; VULETIĆ, V. ; ASPELMEYER, M.. **Cavity cooling of a levitated nanosphere by coherent scattering.** Phys. Rev. Lett., 122:123602, Mar 2019.
- [57] TOROŠ, M.; DELIĆ, U.; HALES, F. ; MONTEIRO, T. S.. **Coherent scattering 2d cooling in levitated cavity optomechanics,** 2020.
- [58] MELO, B.; BRANDÃO, I.; TOMEI, C. ; GUERREIRO, T.. **Directed graphs and interferometry.** Journal of the Optical Society of America B, 37(7):2199, July 2020.
- [59] ATAMAN, S.. **Field operator transformations in quantum optics using a novel graphical method with applications to beam splitters and interferometers.** The European Physical Journal D, 68(10):288, 2014.
- [60] NEWSOM, D. C.; LUNA, F.; FEDOSEEV, V.; LÖFFLER, W. ; BOUWMEESTER, D.. **Optimal optomechanical coupling strength in multimembrane systems.** Phys. Rev. A, 101:033829, Mar 2020.
- [61] BHATTACHARYA, M.; MEYSTRE, P.. **Multiple membrane cavity optomechanics.** Phys. Rev. A, 78:041801, Oct. 2008.

- [62] PIERGENTILI, P.; CATALINI, L.; BAWAJ, M.; ZIPPILLI, S.; MALOSSI, N.; NATALI, R.; VITALI, D. ; GIUSEPPE, G. D.. **Two-membrane cavity optomechanics**. *New Journal of Physics*, 20(8):083024, 2018.
- [63] WEBB, M. S.; MOULTON, P. F.; KASINSKI, J. J.; BURNHAM, R. L.; LOIACONO, G. ; STOLZENBERGER, R.. **High-average-power KTiOAsO<sub>4</sub> optical parametric oscillator**. *Optics Letters*, 23(15):1161, Aug. 1998.
- [64] SATO, S.; OHASHI, M.; FUJIMOTO, M.; FUKUSHIMA, M.; WASEDA, K.; MIYOKI, S.; MAVALVALA, N. ; YAMAMOTO, H.. **High-gain power recycling of a fabry–perot michelson interferometer for a gravitational-wave antenna**. *Applied Optics*, 39(25):4616, Sep. 2000.
- [65] WEI, X.; SHENG, J.; WU, Y.; LIU, W. ; WU, H.. **Twin-beam-enhanced displacement measurement of a membrane in a cavity**. *Applied Physics Letters*, 115(25):251105, Dec. 2019.
- [66] MAGRINI, L.; NORTE, R. A.; RIEDINGER, R.; MARINKOVIĆ, I.; GRASS, D.; DELIĆ, U.; GRÖBLACHER, S.; HONG, S. ; ASPELMEYER, M.. **Near-field coupling of a levitated nanoparticle to a photonic crystal cavity**. *Optica*, 5(12):1597, Dec. 2018.
- [67] VITALI, D.; MANCINI, S.; RIBICHINI, L. ; TOMBESI, P.. **Mirror quiescence and high-sensitivity position measurements with feedback**. *Phys. Rev. A*, 65:063803, May 2002.
- [68] RAKHUBOVSKY, A. A.; MOORE, D. W.; DELIĆ, U. C. V.; KIESEL, N.; ASPELMEYER, M. ; FILIP, R.. **Detecting nonclassical correlations in levitated cavity optomechanics**. *Phys. Rev. Applied*, 14:054052, Nov 2020.
- [69] MELO, B.. **Cavities and tweezers: Developing tools for an optomechanics laboratory**. Master's thesis, Pontifícia Universidade Católica do Rio de Janeiro, 2019.
- [70] GRYNBERG, G.; ASPECT, A.; FABRE, C. ; COHEN-TANNOUDJI, C.. **Introduction to Quantum Optics: From the Semi-classical Approach to Quantized Light**. Cambridge University Press, 2010.
- [71] ISMAIL, N.; KORES, C. C.; GESKUS, D. ; POLLNAU, M.. **Fabry-pérot resonator: spectral line shapes, generic and related airy distributions, linewidths, finesses, and performance at low or**

- frequency-dependent reflectivity. *Optics Express*, 24(15):16366, Jul. 2016.
- [72] THOMPSON, J. D.; ZWICKL, B. M.; JAYICH, A. M.; MARQUARDT, F.; GIRVIN, S. M. ; HARRIS, J. G. E.. **Strong dispersive coupling of a high-finesse cavity to a micromechanical membrane.** *Nature*, 452(7183):72–75, Mar. 2008.
- [73] XU, X.-W.; ZHAO, Y.-J. ; LIU, Y.-X.. **Entangled-state engineering of vibrational modes in a multimembrane optomechanical system.** *Phys. Rev. A*, 88:022325, Aug. 2013.
- [74] RECK, M.; ZEILINGER, A.; BERNSTEIN, H. J. ; BERTANI, P.. **Experimental realization of any discrete unitary operator.** *Physical Review Letters*, 73(1):58–61, jul 1994.
- [75] CLEMENTS, W. R.; HUMPHREYS, P. C.; METCALF, B. J.; KOLTHAMMER, W. S. ; WALSMLEY, I. A.. **Optimal design for universal multiport interferometers.** *Optica*, 3(12):1460, dec 2016.
- [76] SCULLY, M. O.; ZUBAIRY, M. S.. **Quantum Optics.** Cambridge University Press, 1997.
- [77] YU, S.; PIAO, X.; HONG, J. ; PARK, N.. **Interdimensional optical isospectrality inspired by graph networks.** *Optica*, 3(8):836, jul 2016.
- [78] MACZEWSKY, L. J.; WANG, K.; DOVGİY, A. A.; MIROSHNICHENKO, A. E.; MOROZ, A.; EHRHARDT, M.; HEINRICH, M.; CHRISTODOULIDES, D. N.; SZAMEIT, A. ; SUKHORUKOV, A. A.. **Synthesizing multi-dimensional excitation dynamics and localization transition in one-dimensional lattices.** *Nature Photonics*, 14(2):76–81, dec 2019.
- [79] FAZAL, F. M.; BLOCK, S. M.. **Optical tweezers study life under tension.** *Nature Photonics*, 5(6):318–321, may 2011.
- [80] NUSSENZVEIG, H. M.. **Cell membrane biophysics with optical tweezers.** *Eur. Biophys. J.*, 47(5):499–514, nov 2017.
- [81] DE S. ARAÚJO, G. R.; VIANA, N. B.; GÓMEZ, F.; PONTES, B. ; FRASES, S.. **The mechanical properties of microbial surfaces and biofilms.** *The Cell Surface*, 5:100028, dec 2019.

- [82] PONTES, B.; AYALA, Y.; FONSECA, A. C. C.; ROMÃO, L. F.; AMARAL, R. F.; SALGADO, L. T.; LIMA, F. R.; FARINA, M.; VIANA, N. B.; MOURA-NETO, V. ; NUSSENZVEIG, H. M.. **Membrane elastic properties and cell function**. PLoS ONE, 8(7):e67708, jul 2013.
- [83] MONTEIRO, F.; LI, W.; AFEK, G.; LI, C.-L.; MOSSMAN, M. ; MOORE, D. C.. **Force and acceleration sensing with optically levitated nanogram masses at microkelvin temperatures**. Phys. Rev. A, 101:053835, May 2020.
- [84] ETHER, D. S.; PIRES, L. B.; UMRATH, S.; MARTINEZ, D.; AYALA, Y.; PONTES, B.; DE S. ARAÚJO, G. R.; FRASES, S.; INGOLD, G.-L.; ROSA, F. S. S.; VIANA, N. B.; NUSSENZVEIG, H. M. ; NETO, P. A. M.. **Probing the casimir force with optical tweezers**. EPL, 112(4):44001, nov 2015.
- [85] ARVANITAKI, A.; GERACI, A. A.. **Detecting high-frequency gravitational waves with optically levitated sensors**. Phys. Rev. Lett., 110:071105, Feb 2013.
- [86] GERACI, A. A.; PAPP, S. B. ; KITCHING, J.. **Short-range force detection using optically cooled levitated microspheres**. Phys. Rev. Lett., 105:101101, Aug 2010.
- [87] MOORE, D. C.; RIDER, A. D. ; GRATTA, G.. **Search for millicharged particles using optically levitated microspheres**. Phys. Rev. Lett., 113:251801, Dec 2014.
- [88] ASHKIN, A.. **Acceleration and trapping of particles by radiation pressure**. Phys. Rev. Lett., 24(4):156–159, jan 1970.
- [89] AHLUWALIA, B. P. S.; YUAN, X.-C.; TAO, S. H.; CHEONG, W. C.; ZHANG, L. S. ; WANG, H.. **Micromanipulation of high and low indices microparticles using a microfabricated double axicon**. J. Appl. Phys., 99(11):113104, jun 2006.
- [90] LI, G.; ZHANG, S.; ISENHOWER, L.; MALLER, K. ; SAFFMAN, M.. **Crossed vortex bottle beam trap for single-atom qubits**. Opt. Lett., 37(5):851, feb 2012.
- [91] ALDOSSARY, O.. **Bottle atom trapping configuration by optical dipole forces**. J. King Saud Univ. Sci., 26(1):29–35, jan 2014.

- [92] BARREDO, D.; LIENHARD, V.; SCHOLL, P.; DE LÉSÉLEUC, S.; BOULIER, T.; BROWAEYS, A. ; LAHAYE, T.. **Three-dimensional trapping of individual rydberg atoms in ponderomotive bottle beam traps.** Phys. Rev. Lett., 124:023201, Jan 2020.
- [93] XU, P.; HE, X.; WANG, J. ; ZHAN, M.. **Trapping a single atom in a blue detuned optical bottle beam trap.** Opt. Lett., 35(13):2164, jun 2010.
- [94] MELO, B.; BRANDÃO, I.; PINHEIRO DA, B. S.; RODRIGUES, R.; KHOURY, A. ; GUERREIRO, T.. **Optical trapping in a dark focus.** Phys. Rev. Applied, 14:034069, Sep 2020.
- [95] MANDEL, L.; WOLF, E.. **Optical Coherence and Quantum Optics.** Cambridge University Press, Sept. 1995.
- [96] ARLT, J.; PADGETT, M. J.. **Generation of a beam with a dark focus surrounded by regions of higher intensity: the optical bottle beam.** Opt. Lett., 25(4):191, feb 2000.
- [97] ARLT, J.; DHOLAKIA, K.; SONESON, J. ; WRIGHT, E. M.. **Optical dipole traps and atomic waveguides based on besel light beams.** Phys. Rev. A, 63:063602, May 2001.
- [98] SUAREZ, R. A. B.; AMBROSIO, L. A.; NEVES, A. A. R.; ZAMBONI-RACHED, M. ; GESUALDI, M. R. R.. **Experimental optical trapping with frozen waves.** Opt. Lett., 45(9):2514, apr 2020.
- [99] LU, W.; SUN, X.; CHEN, H.; LIU, S. ; LIN, Z.. **Abruptly autofocusing property and optical manipulation of circular airy beams.** Phys. Rev. A, 99:013817, Jan 2019.
- [100] CHENG, H.; ZANG, W.; ZHOU, W. ; TIAN, J.. **Analysis of optical trapping and propulsion of rayleigh particles using airy beam.** Opt. Express, 18(19):20384, sep 2010.
- [101] JIANG, Y.; HUANG, K. ; LU, X.. **Radiation force of abruptly autofocusing airy beams on a rayleigh particle.** Opt. Express, 21(20):24413, oct 2013.
- [102] SHU, J.; CHEN, Z. ; PU, J.. **Radiation forces on a rayleigh particle by highly focused partially coherent and radially polarized vortex beams.** J. Opt. Soc. Am. A, 30(5):916, apr 2013.



- [103] YAN, S.; YAO, B.. Radiation forces of a highly focused radially polarized beam on spherical particles. *Phys. Rev. A*, 76:053836, Nov 2007.
- [104] ZHAO, C.; CAI, Y. ; KOROTKOVA, O.. Radiation force of scalar and electromagnetic twisted gaussian schell-model beams. *Opt. Express*, 17(24):21472, nov 2009.
- [105] ZHANG, D.; YANG, Y.. Radiation forces on rayleigh particles using a focused anomalous vortex beam under paraxial approximation. *Opt. Commun.*, 336:202–206, feb 2015.
- [106] ZHAO, C.-L.; WANG, L.-G. ; LU, X.-H.. Radiation forces on a dielectric sphere produced by highly focused hollow gaussian beams. *Phys. Lett. A*, 363(5-6):502–506, apr 2007.
- [107] ZHAO, C.; CAI, Y.. Trapping two types of particles using a focused partially coherent elegant laguerre–gaussian beam. *Opt. Lett.*, 36(12):2251, jun 2011.
- [108] ZHAN, Q.. Radiation forces on a dielectric sphere produced by highly focused cylindrical vector beams. *J. Opt. A: Pure Appl. Opt.*, 5(3):229–232, mar 2003.
- [109] ZHAO, C.; CAI, Y.; LU, X. ; EYYUBOĞLU, H. T.. Radiation force of coherent and partially coherent flat-topped beams on a rayleigh particle. *Opt. Express*, 17(3):1753, jan 2009.
- [110] WEI, M.-D.; SHIAO, W.-L. ; LIN, Y.-T.. Adjustable generation of bottle and hollow beams using an axicon. *Opt. Commun.*, 248(1-3):7–14, apr 2005.
- [111] LIN, J.-H.; WEI, M.-D.; LIANG, H.-H.; LIN, K.-H. ; HSIEH, W.-F.. Generation of supercontinuum bottle beam using an axicon. *Opt. Express*, 15(6):2940, 2007.
- [112] DU, T.; WANG, T. ; WU, F.. Generation of three-dimensional optical bottle beams via focused non-diffracting bessel beam using an axicon. *Opt. Commun.*, 317:24–28, apr 2014.
- [113] ISENHOWER, L.; WILLIAMS, W.; DALLY, A. ; SAFFMAN, M.. Atom trapping in an interferometrically generated bottle beam trap. *Opt. Lett.*, 34(8):1159, apr 2009.

- [114] DA SILVA, B. P.; PINILLOS, V. A.; TASCA, D. S.; OXMAN, L. E. ; KHOURY, A. Z.. **Pattern revivals from fractional gouy phases in structured light.** *Phys. Rev. Lett.*, 124:033902, Jan 2020.
- [115] AHLUWALIA, B.; YUAN, X.-C. ; TAO, S.. **Generation of self-imaged optical bottle beams.** *Opt. Commun.*, 238(1-3):177–184, aug 2004.
- [116] ZHANG, P.; ZHANG, Z.; PRAKASH, J.; HUANG, S.; HERNANDEZ, D.; SALAZAR, M.; CHRISTODOULIDES, D. N. ; CHEN, Z.. **Trapping and transporting aerosols with a single optical bottle beam generated by moiré techniques.** *Opt. Lett.*, 36(8):1491, apr 2011.
- [117] JONES, P. H.; MARAGO, O. M. ; VOLPE, G.. **Optical Tweezers.** Cambridge University Press, 2015.
- [118] LENTON, I. C. D.; STILGOE, A. B.; RUBINSZTEIN-DUNLOP, H. ; NIEMINEN, T. A.. **Visual guide to optical tweezers.** *European Journal of Physics*, 38(3):034009, Mar. 2017.
- [119] LI, T.. **Fundamental Tests of Physics with Optically Trapped Microspheres.** Springer New York, 2013.
- [120] ALBALADEJO, S.; MARQUÉS, M. I.; LAROCHE, M. ; SÁENZ, J. J.. **Scattering forces from the curl of the spin angular momentum of a light field.** *Phys. Rev. Lett.*, 102:113602, Mar 2009.
- [121] ZHONG, M.-C.; WEI, X.-B.; ZHOU, J.-H.; WANG, Z.-Q. ; LI, Y.-M.. **Trapping red blood cells in living animals using optical tweezers.** *Nat. Commun.*, 4(1), apr 2013.
- [122] LIANG, Y.; LIANG, G.; XIANG, Y.; LAMSTEIN, J.; GAUTAM, R.; BEZRYADINA, A. ; CHEN, Z.. **Manipulation and assessment of human red blood cells with tunable “tug-of-war” optical tweezers.** *Phys. Rev. Applied*, 12:064060, Dec 2019.
- [123] NIEMINEN, T. A.; LOKE, V. L. Y.; STILGOE, A. B.; KNÖNER, G.; BRAŃCZYK, A. M.; HECKENBERG, N. R. ; RUBINSZTEIN-DUNLOP, H.. **Optical tweezers computational toolbox.** *J. Opt. A: Pure Appl. Opt.*, 9(8):S196–S203, jul 2007.
- [124] MATSUMOTO, N.; ANDO, T.; INOUE, T.; OHTAKE, Y.; FUKUCHI, N. ; HARA, T.. **Generation of high-quality higher-order laguerre-gaussian beams using liquid-crystal-on-silicon spatial light modulators.** *J. Opt. Soc. Am. A*, 25(7):1642, jun 2008.

- [125] OHTAKE, Y.; ANDO, T.; FUKUCHI, N.; MATSUMOTO, N.; ITO, H. ; HARA, T.. **Universal generation of higher-order multiringed laguerre-gaussian beams by using a spatial light modulator.** *Opt. Lett.*, 32(11):1411, apr 2007.
- [126] RHODES, D. P.; GHERARDI, D. M.; LIVESEY, J.; MCGLOIN, D.; MELVILLE, H.; FREEGARDE, T. ; DHOLAKIA, K.. **Atom guiding along high order laguerre-gaussian light beams formed by spatial light modulation.** *J. Mod. Opt.*, 53(4):547–556, mar 2006.
- [127] ANDO, T.; OHTAKE, Y.; MATSUMOTO, N.; INOUE, T. ; FUKUCHI, N.. **Mode purities of laguerre-gaussian beams generated via complex-amplitude modulation using phase-only spatial light modulators.** *Opt. Lett.*, 34(1):34, dec 2008.
- [128] HANSEN, P. M.; BHATIA, V. K.; HARRIT, N. ; ODDERSHEDE, L.. **Expanding the optical trapping range of gold nanoparticles.** *Nano Lett.*, 5(10):1937–1942, oct 2005.
- [129] ALINEZHAD, H. G.; REIHANI, S. N. S.. **Optimal condition for optical trapping of large particles: tuning the laser power and numerical aperture of the objective.** *J. Opt. Soc. Am. B*, 36(11):3053, oct 2019.
- [130] LIU, Y.; CHENG, D.; SONEK, G.; BERNS, M.; CHAPMAN, C. ; TROMBERG, B.. **Evidence for localized cell heating induced by infrared optical tweezers.** *Biophys. J.*, 68(5):2137–2144, may 1995.
- [131] PETERMAN, E. J.; GITTES, F. ; SCHMIDT, C. F.. **Laser-induced heating in optical traps.** *Biophys. J.*, 84(2):1308–1316, feb 2003.
- [132] BLÁZQUEZ-CASTRO, A.. **Optical tweezers: Phototoxicity and thermal stress in cells and biomolecules.** *Micromachines*, 10(8):507, jul 2019.
- [133] NIEMINEN, T. A.; HECKENBERG, N. R. ; RUBINSZTEIN-DUNLOP, H.. **Forces in optical tweezers with radially and azimuthally polarized trapping beams.** *Opt. Lett.*, 33(2):122, jan 2008.
- [134] GIBSON, G. M.; LEACH, J.; KEEN, S.; WRIGHT, A. J. ; PADGETT, M. J.. **Measuring the accuracy of particle position and force in optical tweezers using high-speed video microscopy.** *Opt. Express*, 16(19):14561, sep 2008.

- [135] PRALLE, A.; PRUMMER, M.; FLORIN, E.-L.; STELZER, E. ; HÖRBER, J.. **Three-dimensional high-resolution particle tracking for optical tweezers by forward scattered light.** *Microsc. Res. Tech.*, 44(5):378–386, mar 1999.
- [136] ALVES, P. S.; ROCHA, M. S.. **Videomicroscopy calibration of optical tweezers by position autocorrelation function analysis.** *Appl. Phys. B*, 107(2):375–378, mar 2012.
- [137] BERG-SØRENSEN, K.; FLYVBJERG, H.. **Power spectrum analysis for optical tweezers.** *Rev. Sci. Instrum.*, 75(3):594–612, mar 2004.
- [138] MELO, B.; ALMEIDA, F.; TEMPORÃO, G. ; GUERREIRO, T.. **Relaxing constraints on data acquisition and position detection for trap stiffness calibration in optical tweezers.** *Opt. Express*, 28(11):16256, may 2020.
- [139] SIMMONS, R.; FINER, J.; CHU, S. ; SPUDICH, J.. **Quantitative measurements of force and displacement using an optical trap.** *Biophys. J.*, 70(4):1813–1822, apr 1996.
- [140] BROUHARD, G.; SCHEK, H. ; HUNT, A.. **Advanced optical tweezers for the study of cellular and molecular biomechanics.** *IEEE. Trans. Biomed. Eng.*, 50(1):121–125, jan 2003.
- [141] LENTON, I. C. D.; NIEMINEN, T. A.; LOKE, V. L. Y.; STILGOE, A. B.; HU, Y.; KNÖNER, G.; BRAŃCZYK, A. M.; HECKENBERG, N. R. ; RUBINSZTEIN-DUNLOP, H.. **Optical tweezers toolbox.** <https://github.com/ilent2/ott>, 2020.
- [142] GAHAGAN, K. T.; SWARTZLANDER, G. A.. **Optical vortex trapping of particles.** *Opt. Lett.*, 21(11):827, jun 1996.
- [143] ZHANG, H.; LIU, K.-K.. **Optical tweezers for single cells.** *J. R. Soc. Interface*, 5(24):671–690, apr 2008.
- [144] BOOTHE, T.; HILBERT, L.; HEIDE, M.; BERNINGER, L.; HUTTNER, W. B.; ZABURDAEV, V.; VASTENHOUW, N. L.; MYERS, E. W.; DRECHSEL, D. N. ; RINK, J. C.. **A tunable refractive index matching medium for live imaging cells, tissues and model organisms.** *eLife*, 6, jul 2017.
- [145] LIU, P. Y.; CHIN, L. K.; SER, W.; CHEN, H. F.; HSIEH, C.-M.; LEE, C.-H.; SUNG, K.-B.; AYI, T. C.; YAP, P. H.; LIEBERG, B.; WANG, K.;

- BOUROUINA, T. ; LEPRINCE-WANG, Y.. Cell refractive index for cell biology and disease diagnosis: past, present and future. *Lab. Chip*, 16(4):634–644, 2016.
- [146] RAPPAZ, B.; MARQUET, P.; CUCHE, E.; EMERY, Y.; DEPEURSINGE, . ; MAGISTRETTI, P. J.. Measurement of the integral refractive index and dynamic cell morphometry of living cells with digital holographic microscopy. *Opt. Express*, 13(23):9361, nov 2005.
- [147] MOROWITZ, H. J.. The completeness of molecular biology. *Isr. J. Med. Sci.*, 20(9):750—753, September 1984.
- [148] KRAUSE, D. C.; BALISH, M. F.. Structure, function, and assembly of the terminal organelle of *Mycoplasma pneumoniae*. *FEMS Microbiol. Lett.*, 198(1):1–7, apr 2001.
- [149] MANCINI, S.; MAN'KO, V. I. ; TOMBESI, P.. Ponderomotive control of quantum macroscopic coherence. *Phys. Rev. A*, 55:3042–3050, Apr 1997.
- [150] GIOVANNETTI, V.; MANCINI, S. ; TOMBESI, P.. Radiation pressure induced einstein-podolsky-rosen paradox. *EPL*, 54(5):559–565, jun 2001.
- [151] BOSE, S.; JACOBS, K. ; KNIGHT, P. L.. Preparation of nonclassical states in cavities with a moving mirror. *Phys. Rev. A*, 56:4175–4186, Nov 1997.
- [152] MANCINI, S.; GIOVANNETTI, V.; VITALI, D. ; TOMBESI, P.. Entangling macroscopic oscillators exploiting radiation pressure. *Phys. Rev. Lett.*, 88:120401, Mar 2002.
- [153] ZHANG, J.; PENG, K. ; BRAUNSTEIN, S. L.. Quantum-state transfer from light to macroscopic oscillators. *Phys. Rev. A*, 68:013808, Jul 2003.
- [154] PIRANDOLA, S.; VITALI, D.; TOMBESI, P. ; LLOYD, S.. Macroscopic entanglement by entanglement swapping. *Phys. Rev. Lett.*, 97:150403, Oct 2006.
- [155] HOFER, S. G.; HAMMERER, K.. Entanglement-enhanced time-continuous quantum control in optomechanics. *Phys. Rev. A*, 91:033822, Mar 2015.

- [156] FRITSCHER, P.; BORK, R.; GONZÁLEZ, G.; MAVALVALA, N.; OUIMETTE, D.; RONG, H.; SIGG, D. ; ZUCKER, M.. **Readout and control of a power-recycled interferometric gravitational-wave antenna.** *Appl. Opt.*, 40(28):4988–4998, 2001.
- [157] BRANDÃO, I.; SUASSUNA, B.; MELO, B. ; GUERREIRO, T.. **Entanglement dynamics in dispersive optomechanics: Nonclassicality and revival.** *Phys. Rev. Research*, 2:043421, Dec 2020.
- [158] SALA, K.; TUFARELLI, T.. **Exploring corrections to the optomechanical hamiltonian.** *Scientific Reports*, 8(1), June 2018.
- [159] LAW, C. K.. **Effective hamiltonian for the radiation in a cavity with a moving mirror and a time-varying dielectric medium.** *Phys. Rev. A*, 49:433–437, Jan 1994.
- [160] TAVIS, M.; CUMMINGS, F. W.. **Exact solution for an  $n$ -molecule—radiation-field hamiltonian.** *Phys. Rev.*, 170:379–384, Jun 1968.
- [161] MURCH, K. W.. **Cavity Quantum Optomechanics with Ultracold Atoms.** PhD thesis, University of California, Berkeley, 2007.
- [162] MURCH, K. W.; MOORE, K. L.; GUPTA, S. ; STAMPER-KURN, D. M.. **Observation of quantum-measurement backaction with an ultracold atomic gas.** *Nat. Phys.*, 4(7):561–564, may 2008.
- [163] MARLETTO, C.; VEDRAL, V.. **Gravitationally induced entanglement between two massive particles is sufficient evidence of quantum effects in gravity.** *Phys. Rev. Lett.*, 119:240402, Dec 2017.
- [164] SCHRODINGER, E.. **Die gegenwärtige situation in der quantenmechanik.** *Sci. Nat.*, 23(48):807–812, nov 1935.
- [165] VEDRAL, V.. **Quantifying entanglement in macroscopic systems.** *Nature*, 453(7198):1004–1007, jun 2008.
- [166] PRESKILL, J.. **Quantum Computing in the NISQ era and beyond.** *Quantum*, 2:79, Aug. 2018.
- [167] FEYNMAN, R. P.; MORINIGO, F.; WAGNER, W. ; HATFIELD, B.. **Feynman lectures on gravitation.** Reading, Mass.: Addison-Wesley, 12 1996.
- [168] DIÓSI, L.. **A universal master equation for the gravitational violation of quantum mechanics.** *Phys. Lett. A*, 120(8):377–381, mar 1987.

- [169] PENROSE, R.. **On gravity's role in quantum state reduction.** Gen. Relativ. Gravit., 28(5):581–600, may 1996.
- [170] BOSE, S.; MAZUMDAR, A.; MORLEY, G. W.; ULBRICHT, H.; TOROŠ, M.; PATERNOSTRO, M.; GERACI, A. A.; BARKER, P. F.; KIM, M. S. ; MILBURN, G.. **Spin entanglement witness for quantum gravity.** Phys. Rev. Lett., 119:240401, Dec 2017.
- [171] BLENCOWE, M. P.. **Effective field theory approach to gravitationally induced decoherence.** Phys. Rev. Lett., 111:021302, Jul 2013.
- [172] PIKOVSKI, I.; ZYCH, M.; COSTA, F. ; BRUKNER, Č.. **Universal decoherence due to gravitational time dilation.** Nat. Phys., 11(8):668–672, jun 2015.
- [173] BELENCHIA, A.; WALD, R. M.; GIACOMINI, F.; CASTRO-RUIZ, E.; BRUKNER, Č. ; ASPELMEYER, M.. **Information content of the gravitational field of a quantum superposition.** Int. J. Mod. Phys. D, 28(14):1943001, oct 2019.
- [174] CARNEY, D.; STAMP, P. C. E. ; TAYLOR, J. M.. **Tabletop experiments for quantum gravity: a user's manual.** Class. Quantum Gravity, 36(3):034001, jan 2019.
- [175] CORBITT, T.; CHEN, Y.; KHALILI, F.; OTTAWAY, D.; VYATCHANIN, S.; WHITCOMB, S. ; MAVALVALA, N.. **Squeezed-state source using radiation-pressure-induced rigidity.** Phys. Rev. A, 73:023801, Feb 2006.
- [176] WIPF, C.; CORBITT, T.; CHEN, Y. ; MAVALVALA, N.. **Route to ponderomotive entanglement of light via optically trapped mirrors.** New J. Phys., 10(9):095017, sep 2008.
- [177] SAFAVI-NAEINI, A. H.; GRÖBLACHER, S.; HILL, J. T.; CHAN, J.; ASPELMEYER, M. ; PAINTER, O.. **Squeezed light from a silicon micromechanical resonator.** Nature, 500(7461):185–189, aug 2013.
- [178] TIAN, L.. **Robust photon entanglement via quantum interference in optomechanical interfaces.** Phys. Rev. Lett., 110:233602, Jun 2013.
- [179] BARZANJEH, S.; REDCHENKO, E. S.; PERUZZO, M.; WULF, M.; LEWIS, D. P.; ARNOLD, G. ; FINK, J. M.. **Stationary entangled radiation from micromechanical motion.** Nature, 570(7762):480–483, June 2019.

- [180] WANG, Y.-D.; CLERK, A. A.. **Reservoir-engineered entanglement in optomechanical systems.** Phys. Rev. Lett., 110:253601, Jun 2013.
- [181] KRISNANDA, T.; ZUPPARDO, M.; PATERNOSTRO, M. ; PATEREK, T.. **Revealing nonclassicality of inaccessible objects.** Phys. Rev. Lett., 119:120402, Sep 2017.
- [182] MA, Y.; ARMATA, F.; KHOSLA, K. E. ; KIM, M. S.. **Optical squeezing for an optomechanical system without quantizing the mechanical motion.** Phys. Rev. Research, 2:023208, May 2020.
- [183] DUAN, L.-M.; GIEDKE, G.; CIRAC, J. I. ; ZOLLER, P.. **Inseparability criterion for continuous variable systems.** Phys. Rev. Lett., 84:2722–2725, Mar 2000.
- [184] ROMERO-ISART, O.; JUAN, M. L.; QUIDANT, R. ; CIRAC, J. I.. **Toward quantum superposition of living organisms.** New J. Phys., 12(3):033015, mar 2010.
- [185] NEUMEIER, L.; NORTHUP, T. E. ; CHANG, D. E.. **Reaching the optomechanical strong-coupling regime with a single atom in a cavity.** Phys. Rev. A, 97:063857, Jun 2018.
- [186] BRENNECKE, F.; RITTER, S.; DONNER, T. ; ESSLINGER, T.. **Cavity optomechanics with a bose-einstein condensate.** Science, 322(5899):235–238, oct 2008.
- [187] TAKATSUJI, M.. **Quantum theory of the optical kerr effect.** Phys. Rev., 155:980–986, Mar 1967.
- [188] LOMBARDI, E.; SCIARRINO, F.; POPESCU, S. ; DE MARTINI, F.. **Teleportation of a vacuum–one-photon qubit.** Phys. Rev. Lett., 88:070402, Jan 2002.
- [189] GUERREIRO, T.; MONTEIRO, F.; MARTIN, A.; BRASK, J. B.; VÉRTESI, T.; KORZH, B.; CALOZ, M.; BUSSIÈRES, F.; VERMA, V. B.; LITA, A. E.; MIRIN, R. P.; NAM, S. W.; MARSILLI, F.; SHAW, M. D.; GISIN, N.; BRUNNER, N.; ZBINDEN, H. ; THEW, R. T.. **Demonstration of einstein-podolsky-rosen steering using single-photon path entanglement and displacement-based detection.** Phys. Rev. Lett., 117:070404, Aug 2016.



- [190] PEYRONEL, T.; FIRSTENBERG, O.; LIANG, Q.-Y.; HOFFERBERTH, S.; GORSHKOV, A. V.; POHL, T.; LUKIN, M. D. ; VULETIĆ, V.. **Quantum nonlinear optics with single photons enabled by strongly interacting atoms**. *Nature*, 488(7409):57–60, jul 2012.
- [191] HOFHEINZ, M.; WANG, H.; ANSMANN, M.; BIALCZAK, R. C.; LUCERO, E.; NEELEY, M.; O'CONNELL, A. D.; SANK, D.; WENNER, J.; MARTINIS, J. M. ; CLELAND, A. N.. **Synthesizing arbitrary quantum states in a superconducting resonator**. *Nature*, 459(7246):546–549, may 2009.
- [192] KRANTZ, P.; KJAERGAARD, M.; YAN, F.; ORLANDO, T. P.; GUSTAVSSON, S. ; OLIVER, W. D.. **A quantum engineer's guide to superconducting qubits**. *Appl. Phys. Rev.*, 6(2):021318, June 2019.
- [193] BREUER, H.-P.; PETRUCCIONE, F.. **The Theory of Open Quantum Systems**. Oxford University Press, 2007.
- [194] WEEDBROOK, C.; PIRANDOLA, S.; GARCÍA-PATRÓN, R.; CERF, N. J.; RALPH, T. C.; SHAPIRO, J. H. ; LLOYD, S.. **Gaussian quantum information**. *Rev. Mod. Phys.*, 84:621–669, May 2012.
- [195] DAVIDOVICH, L.. **Sub-poissonian processes in quantum optics**. *Rev. Mod. Phys.*, 68:127–173, Jan 1996.
- [196] LLOYD, S.; BRAUNSTEIN, S. L.. **Quantum computation over continuous variables**. *Phys. Rev. Lett.*, 82:1784–1787, Feb 1999.
- [197] KIPPENBERG, T. J.; SPILLANE, S. M. ; VAHALA, K. J.. **Kerr-nonlinearity optical parametric oscillation in an ultrahigh- $q$  toroid microcavity**. *Phys. Rev. Lett.*, 93:083904, Aug 2004.
- [198] RABL, P.. **Photon blockade effect in optomechanical systems**. *Phys. Rev. Lett.*, 107:063601, Aug 2011.
- [199] MEYER, N.; SOMMER, A. D. L. R.; MESTRES, P.; GIESELER, J.; JAIN, V.; NOVOTNY, L. ; QUIDANT, R.. **Resolved-sideband cooling of a levitated nanoparticle in the presence of laser phase noise**. *Phys. Rev. Lett.*, 123:153601, Oct 2019.
- [200] OPATRNY, T.; WELSCH, D.-G. ; VOGEL, W.. **Homodyne detection for measuring internal quantum correlations of optical pulses**. *Phys. Rev. A*, 55:1416–1422, Feb 1997.

- [201] RUDOLPH, H.; HORNBERGER, K. ; STICKLER, B. A.. **Entangling levitated nanoparticles by coherent scattering.** Phys. Rev. A, 101:011804, Jan 2020.
- [202] BOHNET, J. G.; SAWYER, B. C.; BRITTON, J. W.; WALL, M. L.; REY, A. M.; FOSS-FEIG, M. ; BOLLINGER, J. J.. **Quantum spin dynamics and entanglement generation with hundreds of trapped ions.** Science, 352(6291):1297–1301, June 2016.
- [203] XU, V.; JAFFE, M.; PANDA, C. D.; KRISTENSEN, S. L.; CLARK, L. W. ; MÜLLER, H.. **Probing gravity by holding atoms for 20 seconds.** Science, 366(6466):745–749, Nov. 2019.
- [204] BERRADA, T.; VAN FRANK, S.; BÜCKER, R.; SCHUMM, T.; SCHAFF, J.-F. ; SCHMIEDMAYER, J.. **Integrated mach–zehnder interferometer for bose–einstein condensates.** Nature Communications, 4(1), June 2013.
- [205] O'CONNELL, A. D.; HOFHEINZ, M.; ANSMANN, M.; BIALCZAK, R. C.; LENANDER, M.; LUCERO, E.; NEELEY, M.; SANK, D.; WANG, H.; WEIDES, M.; WENNER, J.; MARTINIS, J. M. ; CLELAND, A. N.. **Quantum ground state and single-phonon control of a mechanical resonator.** Nature, 464(7289):697–703, Mar. 2010.
- [206] ROMERO-ISART, O.; PFLANZER, A. C.; BLASER, F.; KALTENBAEK, R.; KIESEL, N.; ASPELMEYER, M. ; CIRAC, J. I.. **Large quantum superpositions and interference of massive nanometer-sized objects.** Phys. Rev. Lett., 107:020405, Jul 2011.
- [207] CARLESSO, M.; PATERNOSTRO, M.. **Opto-mechanical test of collapse models.** In: FUNDAMENTAL THEORIES OF PHYSICS, p. 205–215. Springer International Publishing, Oct. 2020.
- [208] KRISNANDA, T.; THAM, G. Y.; PATERNOSTRO, M. ; PATEREK, T.. **Observable quantum entanglement due to gravity.** npj Quantum Information, 6(1), Jan. 2020.
- [209] AGGARWAL, N.; WINSTONE, G. P.; TEO, M.; BARYAKHTAR, M.; LARSON, S. L.; KALOGERA, V. ; GERACI, A. A.. **Searching for new physics with a levitated-sensor-based gravitational-wave detector,** 2020.

- [210] CHENG, J.; ZHANG, W.-Z.; ZHOU, L. ; ZHANG, W.. **Preservation macroscopic entanglement of optomechanical systems in non-markovian environment.** Scientific Reports, 6(1), Apr. 2016.
- [211] CHEN, Z. X.; LIN, Q.; HE, B. ; LIN, Z. Y.. **Entanglement dynamics in double-cavity optomechanical systems.** Optics Express, 25(15):17237, July 2017.
- [212] LI, G.; NIE, W.; LI, X. ; CHEN, A.. **Dynamics of ground-state cooling and quantum entanglement in a modulated optomechanical system.** Phys. Rev. A, 100:063805, Dec 2019.
- [213] FAROUGHI, Z.; AHANJ, A.; JAVIDAN, K. ; NAZIFKAR, S.. **Dynamics of entanglement in optomechanical cavity arrays: Localization-delocalization transition.** International Journal of Theoretical Physics, 60(1):155–163, Jan. 2021.
- [214] ROMERO-ISART, O.; PFLANZER, A. C.; JUAN, M. L.; QUIDANT, R.; KIESEL, N.; ASPELMEYER, M. ; CIRAC, J. I.. **Optically levitating dielectrics in the quantum regime: Theory and protocols.** Physical Review A, 83(1), jan 2011.
- [215] BRANDÃO, I.. **Numerical linear optomechanics,** 2020. <https://github.com/IgorBrandao42/Gaussian-Quantum-Information-Toolbox-for-Linear-Optomechanics>.
- [216] JACKSON, J.. **Classical Electrodynamics.** New York: John Wiley& Sons. Inc, 1998.
- [217] PFLANZER, A. C.; ROMERO-ISART, O. ; CIRAC, J. I.. **Master-equation approach to optomechanics with arbitrary dielectrics.** Phys. Rev. A, 86:013802, Jul 2012.
- [218] DELIĆ, U.; GRASS, D.; REISENBAUER, M.; DAMM, T.; WEITZ, M.; KIESEL, N. ; ASPELMEYER, M.. **Levitated cavity optomechanics in high vacuum.** Quantum Science and Technology, 5(2):025006, Mar. 2020.
- [219] GARDINER, C. W.; COLLETT, M. J.. **Input and output in damped quantum systems: Quantum stochastic differential equations and the master equation.** Physical Review A, 31(6):3761–3774, jun 1985.

- [220] GIOVANNETTI, V.; VITALI, D.. Phase-noise measurement in a cavity with a movable mirror undergoing quantum brownian motion. *Phys. Rev. A*, 63:023812, Jan 2001.
- [221] GENES, C.; VITALI, D.; TOMBESI, P.; GIGAN, S. ; ASPELMEYER, M.. Ground-state cooling of a micromechanical oscillator: Comparing cold damping and cavity-assisted cooling schemes. *Physical Review A*, 77(3), Mar. 2008.
- [222] DELIĆ, U.. Cavity cooling by coherent scattering of a levitated nanosphere in vacuum. PhD thesis, Universität Wien, 2019.
- [223] CALDEIRA, A.; LEGGETT, A.. Quantum tunnelling in a dissipative system. *Annals of Physics*, 149(2):374–456, Sept. 1983.
- [224] TSEKOV, R.; RUCKENSTEIN, E.. Stochastic dynamics of a subsystem interacting with a solid body with application to diffusive processes in solids. *The Journal of Chemical Physics*, 100(2):1450–1455, Jan. 1994.
- [225] SANTOS, J. P.; CÉLERI, L. C.; LANDI, G. T. ; PATERNOSTRO, M.. The role of quantum coherence in non-equilibrium entropy production. *npj Quantum Information*, 5(1), Mar. 2019.
- [226] GROISMAN, B.; POPESCU, S. ; WINTER, A.. Quantum, classical, and total amount of correlations in a quantum state. *Phys. Rev. A*, 72:032317, Sep 2005.
- [227] ATAMAN, S.. A graphical method in quantum optics. *Journal of Physics Communications*, 2(3):035032, mar 2018.
- [228] ATAMAN, S.. The quantum optical description of three experiments involving non-linear optics using a graphical method. *The European Physical Journal D*, 69(2):44, 2015.
- [229] GU, X.; ERHARD, M.; ZEILINGER, A. ; KRENN, M.. Quantum experiments and graphs ii: Quantum interference, computation, and state generation. *Proceedings of the National Academy of Sciences*, 116(10):4147–4155, 2019.
- [230] SUASSUNA, B.; MELO, B. ; GUERREIRO, T.. Path integrals and nonlinear optical tweezers. *Phys. Rev. A*, 103:013110, Jan 2021.

- [231] KHALILI, F.; DANILISHIN, S.; MIAO, H.; MÜLLER-EBHARDT, H.; YANG, H. ; CHEN, Y.. **Preparing a mechanical oscillator in non-gaussian quantum states.** Phys. Rev. Lett., 105:070403, Aug 2010.
- [232] GUERREIRO, T.. **Quantum effects in gravity waves.** Classical and Quantum Gravity, 37(15):155001, July 2020.
- [233] PARIKH, M.; WILCZEK, F. ; ZAHARIADE, G.. **Quantum mechanics of gravitational waves,** 2020.
- [234] CARLESSO, M.; BASSI, A.; PATERNOSTRO, M. ; ULBRICHT, H.. **Testing the gravitational field generated by a quantum superposition.** New Journal of Physics, 21(9):093052, Sept. 2019.
- [235] PIKOVSKI, I.; VANNER, M. R.; ASPELMEYER, M.; KIM, M. S. ; BRUKNER, Č.. **Probing planck-scale physics with quantum optics.** Nature Physics, 8(5):393–397, Mar. 2012.
- [236] ARMATA, F.; LATMIRAL, L.; PLATO, A. D. K. ; KIM, M. S.. **Quantum limits to gravity estimation with optomechanics.** Phys. Rev. A, 96:043824, Oct 2017.
- [237] QVARFORT, S.; SERAFINI, A.; BARKER, P. F. ; BOSE, S.. **Gravimetry through non-linear optomechanics.** Nature Communications, 9(1), Sept. 2018.
- [238] WINKLER, K.. **An analytical and computational approach to steady-state optomechanical systems by quantum langevin equations.** Master's thesis, Universität Wien, 2018.
- [239] ADESSO, G.; RAGY, S. ; LEE, A. R.. **Continuous variable quantum information: Gaussian states and beyond.** Open Systems & Information Dynamics, 21(01n02):1440001, Mar. 2014.
- [240] KENFACK, A.; YCZKOWSKI, K.. **Negativity of the wigner function as an indicator of non-classicality.** Journal of Optics B: Quantum and Semiclassical Optics, 6(10):396–404, Aug. 2004.
- [241] SOHR, P.; LINK, V.; LUOMA, K. ; STRUNZ, W. T.. **Typical gaussian quantum information.** Journal of Physics A: Mathematical and Theoretical, 52(3):035301, Dec. 2018.
- [242] WILLIAMSON, J.. **On the algebraic problem concerning the normal forms of linear dynamical systems.** American Journal of Mathematics, 58(1):141, Jan. 1936.

- [243] SERAFINI, A.. **Quantum continuous variables : a primer of theoretical methods**. CRC Press, Taylor & Francis Group, Boca Raton, FL, 2017.
- [244] HERBUT, F.. **On mutual information in multipartite quantum states and equality in strong subadditivity of entropy**. *Journal of Physics A: Mathematical and General*, 37(10):3535–3542, Feb. 2004.
- [245] BANCHI, L.; BRAUNSTEIN, S. L. ; PIRANDOLA, S.. **Quantum fidelity for arbitrary gaussian states**. *Phys. Rev. Lett.*, 115:260501, Dec 2015.
- [246] PLENIO, M. B.. **Logarithmic negativity: A full entanglement monotone that is not convex**. *Phys. Rev. Lett.*, 95:090503, Aug 2005.
- [247] ADESSO, G.; ILLUMINATI, F.. **Entanglement in continuous-variable systems: recent advances and current perspectives**. *Journal of Physics A: Mathematical and Theoretical*, 40(28):7821–7880, June 2007.

## A

### List of publications

1. B. MELO; I. BRANDÃO; C. TOMEI; T. GUERREIRO. **Directed graphs and interferometry**. J. Opt. Soc. Am. B 37 (7): 2199-2208, jul 2020.
2. B. MELO; I. BRANDÃO; B. PINHEIRO DA SILVA; R. B. RODRIGUES; A. Z. Khoury; T. GUERREIRO. **Optical Trapping in a Dark Focus**. Phys. Rev. Applied 14:034069, sep 2020.
3. I. BRANDÃO; B. SUASSUNA; B. MELO; T. GUERREIRO. **Entanglement dynamics in dispersive optomechanics: Nonclassicality and revival**. Phys. Rev. Research 2:043421, dez 2020.
4. I. BRANDÃO; D. TANDEITNIK; T. GUERREIRO. **Coherent Scattering-mediated correlations between levitated nanospheres**. arxiv:2102.08969, jan 2020.

## B

### Overview on continuous variable systems

In this Appendix, we present a succinct description of continuous variable systems, gaussian states and the entanglement criterias used throughout this work.

#### B.1

##### Continuous Variable systems

A quantum system whose Hilbert space is infinite-dimensional and described by observables with continuous spectra is called a *continuous variable systems* [194]. In general we have  $M$  bosonic modes, each with their corresponding annihilation ( $\hat{a}_j$ ) and creation ( $\hat{a}_j^\dagger$ ) operators, obeying bosonic commutation relations. These can be conventionally arranged in a  $2M$ -dimensional vectorial operator  $\hat{\mathbf{b}} = (\hat{a}_1, \hat{a}_1^\dagger, \hat{a}_2, \hat{a}_2^\dagger, \dots)^T$  whose commutation relations can be expressed as  $[\hat{b}_j, \hat{b}_k] = \Omega_{jk}$  where  $j, k = 1, \dots, 2M$  and  $\Omega$  is the  $2M \times 2M$  symplectic form matrix given by

$$\Omega = \bigoplus_{k=1}^M \Omega_k \quad , \quad \Omega_k = \begin{bmatrix} 0 & 1 \\ -1 & 0 \end{bmatrix} . \quad (\text{B-1})$$

From these bosonic operators, we can define the corresponding quadrature operators  $\hat{x}_j = \hat{a}_j^\dagger + \hat{a}_j$  and  $\hat{p}_j = i(\hat{a}_j^\dagger - \hat{a}_j)$  and once again suitably arrange them into a  $2M$ -dimensional vectorial operator  $\hat{\mathbf{X}} = (\hat{x}_1, \hat{p}_1, \hat{x}_2, \hat{p}_2, \dots)^T$ . It immediately follows from the bosonic commutation relations above that the quadratures must satisfy the canonical commutation relations  $[\hat{X}_j, \hat{X}_k] = 2i \Omega_{jk}$ .

In general, a quantum state of a CV system is described by an infinite-dimensional density matrix  $\rho$  containing all the information about the state. Working with infinite matrices can easily become cumbersome and it is desirable to find a more attractive alternative. Fortunately, it is possible to find a mapping from the density matrix  $\rho$  onto the  $2M$ -dimensional phase-space by means of the Wigner function, a quasiprobability distribution [194, 238]. In order to formally introduce the Wigner function, we first define the Weyl displacement operator  $\hat{D}(\boldsymbol{\xi}) \equiv \exp(i\hat{\mathbf{X}}^T \Omega \boldsymbol{\xi})$ , such that any density matrix  $\rho$  is equivalent to a Wigner characteristic function  $\chi(\boldsymbol{\xi}) \equiv \text{tr}(\rho \hat{D}(\boldsymbol{\xi}))$  and, via a



Fourier Transform, to a Wigner function [194]

$$W(\mathbf{x}) = \int \exp(-i\mathbf{x}^T \Omega \boldsymbol{\xi}) \chi(\boldsymbol{\xi}) \frac{d^{2M} \boldsymbol{\xi}}{(2\pi)^{2M}}, \quad (\text{B-2})$$

where  $\mathbf{x} \in \mathbb{R}^{2M}$  are the eigenvalues of  $\hat{\mathbf{X}}$  spanning the  $2M$ -dimensional phase space. We should note that the Wigner function is normalized to one, and it can become negative [194, 239], which can be used as a measure of non-classicality [240].

## B.2

### Gaussian states

A special class of quantum states, both for its simplicity in their theoretical description and experimental implementation, are *gaussian states*, defined as any quantum state whose Wigner function is gaussian [194, 239]. Our interest in these states are threefold.

First, from their definition, they are completely characterized by their first moment,  $\bar{\mathbf{X}} \equiv \langle \hat{\mathbf{X}} \rangle = \text{tr}(\rho \hat{\mathbf{X}})$ , and second moments represented by the *covariance matrix* (CM), whose entries are given by

$$V_{j,k} = \frac{1}{2} \langle \hat{X}_j \hat{X}_k + \hat{X}_k \hat{X}_j \rangle - \langle \hat{X}_j \rangle \langle \hat{X}_k \rangle. \quad (\text{B-3})$$

This greatly simplifies our treatment of these system, as instead of dealing with high-dimensional density matrices/phase spaces, we need only to worry about  $2M$ -dimensional vectors and  $2M \times 2M$  matrices. Observe that a direct consequence of the commutations relation of the quadrature operators is that the CM is a positive definite real matrix satisfying

$$V + i\Omega > 0,$$

which reduces to the Heisenberg uncertainty principles as its diagonal entries are the variances of the quadratures operators.

Secondly, the dynamics dictated by Hamiltonians that are at most second-order polynomials in the bosonic operators preserve the gaussianity of these states [194].

Finally, they are easily accessible in the laboratory as they describe the EM field of lasers, particles in thermal equilibrium, the vacuum of EM fields, among other relevant physical states. In the following we present some common examples of single mode gaussian states.

### Vacuum state

The vacuum state, also called ground state, is the Fock state with  $n = 0$  photons/phonons for an optical/mechanical mode, i.e.,  $|0\rangle$ . Its mean quadratures are  $\bar{\mathbf{X}} = \mathbf{0}$  with CM  $V = \mathbb{1}$ , where  $\mathbb{1}$  denotes the  $2 \times 2$  identity matrix. It thus follows that the ground state minimizes Heisenberg's uncertainty principle with minimum variance symmetrically in position and momentum.

### Coherent states

Coherent states are displaced vacuum states  $|\alpha\rangle = \hat{D}(\alpha)|0\rangle$ , where  $\hat{D}(\alpha) \equiv \exp(\alpha\hat{a}^\dagger - \alpha^*\hat{a})$ ,  $\alpha \in \mathbb{C}$ , denotes a displacement operator that effectively displaces the mean quadrature vector of the vacuum state to  $\bar{\mathbf{X}} = (\text{Re}(\alpha), \text{Im}(\alpha))$  while leaving its CM unchanged,  $V = \mathbb{1}$ . In other words, the variances of the quadratures for these states do not depend on their amplitude  $\alpha$ , while their mean directly scale with it. Thus, for highly populated coherent states with  $\alpha \gg 1$ , their uncertainty becomes negligible when compared to their variances.

Coherent states make up a good approximation to classical states. This can be seen from the following facts: given an harmonic potential, the movement of the mean quadratures of these states in phase space mimics the motion of a classical harmonic oscillator; the radiation emitted from a classical current distribution is in a coherent state [76]; these states minimize Heisenberg uncertainty relation.

Coherent states are eigenstates of the annihilation operator  $\hat{a}|\alpha\rangle = \alpha|\alpha\rangle$  whose expansion in the Fock basis is given by

$$|\alpha\rangle = e^{-\frac{|\alpha|^2}{2}} \sum_{n=0}^{\infty} \frac{\alpha^n}{\sqrt{n!}} |n\rangle. \quad (\text{B-4})$$

Moreover, coherent states form an overcomplete basis for their Hilbert space since they span the whole space

$$\frac{1}{\pi} \int |\alpha\rangle \langle\alpha| d^2\alpha = \mathbb{1}, \quad (\text{B-5})$$

although two coherent states with different amplitudes are non-orthogonal:

$$|\langle\beta|\alpha\rangle|^2 = e^{-|\beta-\alpha|^2}. \quad (\text{B-6})$$

### Squeezed states

Analogously, squeezed states are squeezed vacuum states  $|r\rangle = \hat{S}(r)|0\rangle$ , where  $\hat{S}(r) \equiv \exp\left(r[\hat{a}^2 - \hat{a}^{\dagger 2}]/2\right)$ ,  $r \in \mathbb{R}$ , denotes a squeezing operator that leaves the mean quadrature of the vacuum state unchanged,  $\bar{\mathbf{X}} = \mathbf{0}$ , while squeezing one of its variance and expanding the other one,  $V = \text{diag}(e^{-2r}, e^{+2r})$ . Although the quadratures' variance are no longer symmetrical, they still minimize Heisenberg uncertainty principle. This property of squeezed states is fundamental to quantum metrology as it allows for enhanced sensitivity in one quadrature than it is possible for the previous states, e.g., the enhanced sensitivity in gravitational wave detection reported by LIGO [7].

As a final remark, in the Fock basis, the squeezed state takes the following form [194]

$$|r\rangle = \frac{1}{\sqrt{\cosh(r)}} \sum_{n=0}^{\infty} \frac{\sqrt{(2n)!}}{2^n n!} \tanh(r^n) |n\rangle. \quad (\text{B-7})$$

### Thermal states

Thermal states follow the Boltzmann distribution  $p(E) \propto e^{-\beta E}$  of finding the system at temperature  $T$  with energy  $E$ , where  $\beta \equiv \frac{1}{k_B T}$  is the inverse temperature and  $k_B$  is the Boltzmann constant. If we associate the energy variable with the Hamiltonian operator for a single bosonic mode of frequency  $\omega$ , we find

$$\rho(T) \equiv \frac{1}{Z} e^{-\beta \hat{H}} = \frac{1}{Z} \sum_{n=0}^{\infty} e^{-n \frac{\hbar \omega}{k_B T}} |n\rangle \langle n| \quad (\text{B-8})$$

with  $Z = \text{tr}(e^{-\beta \hat{H}})$  the partition function. The mean occupation number  $\bar{n} = [e^{\beta \hbar \omega} - 1]^{-1}$  allows for a more useful representation in the Fock basis

$$\rho(\bar{n}) = \sum_{n=0}^{\infty} \frac{\bar{n}^n}{(\bar{n} + 1)^{\bar{n}+1}} |n\rangle \langle n|. \quad (\text{B-9})$$

Finally, the thermal state has zero mean quadratures,  $\bar{\mathbf{X}} = \mathbf{0}$ , and an also diagonal CM given by  $V = (2\bar{n} + 1) \mathbb{1}$ .

## B.3

### Symplectic geometry and informational measures for gaussian states

We define the group of real symplectic matrices as the matrices that preserves the bosonic commutations relations presented in the beginning of the chapter, i.e., [194, 239]

$$\text{Sp}(2M, \mathbb{R}) = \{S : S\Omega S^T = \Omega\}. \quad (\text{B-10})$$

By definition, these matrices must be  $2M \times 2M$  with determinant  $\det(S) = 1$  and, thus invertible. Following the Williamson's theorem, for a given quantum gaussian state  $\rho$ , there exists a symplectic matrix  $S$  that diagonalizes its covariance matrix  $V$  such that [242]

$$V = S\tilde{V}S^T, \quad \tilde{V} = \bigoplus_{k=1}^M \nu_k \mathbb{1} \quad (\text{B-11})$$

where  $\nu_k, k = 1 \dots M$ , are called the symplectic eigenvalues of  $V$ . They can be computed from modulus of the  $2M$  eigenvalues of  $i\Omega V$  [194].

In the following, we briefly present some useful analytical expressions for gaussian states in terms of their mean quadratures, CM and/or symplectic eigenvalues.

### Partial trace

Consider a density matrix  $\rho_{AB}$  describing a multipartite gaussian state, which we choose to subdivide into the subsystems  $A$  and  $B$ , respectively, with  $m$  and  $n$  modes. Let  $\mathbf{r} = (\mathbf{r}_A, \mathbf{r}_B)$  be its first moments and

$$V = \begin{bmatrix} V_A & V_{AB} \\ V_{AB}^T & V_B \end{bmatrix} \quad (\text{B-12})$$

be its  $2(m+n) \times 2(m+n)$  covariance matrix. Then, the reduced density matrix  $\rho_A = \text{tr}_B(\rho_{AB})$  describing solely the subsystem  $A$  is also a gaussian state with first moments  $\mathbf{r}_A$  and covariance matrix  $V_A$  [243].

### Wigner function

The Wigner function for a  $M$ -mode gaussian state with mean quadrature vector  $\bar{\mathbf{x}}$  and covariance matrix  $V$  at some point  $\mathbf{X} \in \mathbb{R}^{2M}$  in phase space has the following form [194]

$$W(\mathbf{x}) = \frac{1}{(2\pi)^M \sqrt{\det(V)}} e^{-\frac{1}{2}(\mathbf{x}-\bar{\mathbf{x}})^T V^{-1}(\mathbf{x}-\bar{\mathbf{x}})}. \quad (\text{B-13})$$

### von Neumann entropy

The von Neumann entropy  $S$  for a gaussian state with associated covariance matrix  $V$  is a function of its symplectic eigenvalues  $\nu_k$ :

$$S = \sum_{k=1}^M g(\nu_k). \quad (\text{B-14})$$

where  $g(x) = \frac{x+1}{2} \log\left(\frac{x+1}{2}\right) - \frac{x-1}{2} \log\left(\frac{x-1}{2}\right)$ .

### Mutual Information

We define the mutual information of a multipartite  $M$ -mode system as [244]

$$I_{\text{tot}} = \sum_{j=1}^M S_j - S_{\text{tot}} \quad (\text{B-15})$$

where  $S_{\text{tot}}$  denote the von Neumann entropy of the total system, calculated through the formula above using the total covariance matrix  $V$  of the gaussian state; and  $S_j$  is the von Neumann entropy for the  $j$ -th single mode calculated from  $V_j$ , the  $2 \times 2$  block diagonal matrix from  $V$  relative only to the  $j$ -th mode, see the partial trace for gaussian states.

### Purity

The purity of a Gaussian quantum state with density matrix  $\rho$  and associated covariance matrix  $V$  is the measure of how pure the state and it is given by [239, 241]

$$\mu_\rho = \text{tr}(\rho^2) = \frac{1}{\sqrt{\det(V)}}, \quad (\text{B-16})$$

where pure states have  $\mu_\rho = 1$ .

### Quantum fidelity

Given two  $M$ -mode gaussian states  $\rho_1$ , with mean quadratures  $\bar{\mathbf{x}}_1$  and CM  $V_1$ , and  $\rho_2$ , with mean quadratures  $\bar{\mathbf{x}}_2$  and CM  $V_2$ , the quantum fidelity between them is given by [245]

$$F(\rho_1, \rho_2) \equiv \text{tr}\left(\sqrt{\sqrt{\rho_1}\rho_2\sqrt{\rho_1}}\right) = F_0(V_1, V_2) e^{-\frac{1}{4}(\bar{\mathbf{x}}_2 - \bar{\mathbf{x}}_1)^T (V_1 + V_2)^{-1} (\bar{\mathbf{x}}_2 - \bar{\mathbf{x}}_1)}, \quad (\text{B-17})$$

$$F_0^4(V_1, V_2) = 2^{2M} \frac{\det\left[2\left(\sqrt{\mathbb{1} + \frac{(V_{\text{aux}}\Omega)^{-2}}{4}} + \mathbb{1}\right)V_{\text{aux}}\right]}{\det(V_1 + V_2)}, \quad (\text{B-18})$$

where  $V_{\text{aux}} \equiv \frac{1}{2}\Omega^T(V_1 + V_2)^{-1}\left(\Omega + V_2\Omega V_1\right)$  and here  $\mathbb{1}$  stands for the  $2M \times 2M$  identity matrix.

## Squeezing degree

In order to quantify the squeezing in a single mode of a multipartite gaussian state, we follow the procedure outlined in [49]. First we perform a partial trace over the full system in order to arrive at the  $2 \times 2$  covariance matrix  $V_j$  describing solely the  $j$ -th mode; secondly, we quantify the amount of squeezing by finding the variances of the squeezed and antisqueezed quadratures, respectively  $V_{\text{sq}}$  and  $V_{\text{asq}}$ :

$$V_{\text{sq}} = \min(\text{eig}(V_j)) \quad V_{\text{asq}} = \max(\text{eig}(V_j)), \quad (\text{B-19})$$

where  $\text{eig}(V_j)$  denotes the eigenvalues of  $V_j$ . The squeezing degree is, then,  $\eta \equiv V_{\text{sq}}/V_{\text{asq}} \leq 1$ .

## B.4

### Entanglement Criterias

#### B.4.1

##### Duan Criteria

A sufficient criterion for inseparability of any two-mode CV state has been proposed in terms of Einstein-Podolski-Rosen (EPR)-like variances [183]. For a given CV system, consider the EPR-like operators

$$\hat{u} = |a|\hat{x}_1 + \frac{1}{a}\hat{x}_2, \quad (\text{B-20})$$

$$\hat{v} = |a|\hat{p}_1 - \frac{1}{a}\hat{p}_2, \quad (\text{B-21})$$

where  $a \in \mathbb{R}^*$  and the operators  $\hat{x}_j, \hat{p}_j$  follow the commutation relations:  $[\hat{x}_j, \hat{p}_k] = i\delta_{jk}$ ,  $j, k = 1, 2$ . We stress that here we are considering “normalized” operator, which accounts for the lack of a factor of two in these commutations relations. It has been shown that any separable bipartite CV state must satisfy

$$(\Delta\hat{u})^2 + (\Delta\hat{v})^2 \geq \left[a^2 + \frac{1}{a^2}\right], \quad (\text{B-22})$$

with  $(\Delta\hat{o})^2 \equiv \langle\hat{o}^2\rangle - \langle\hat{o}\rangle^2$  denoting the variance of an observable  $\hat{o}$ .

Therefore, if a violation of the above inequality is observed, the state is necessarily entangled. We stress that if the criteria is satisfied, then we can retrieve no information as this inequality does not imply that the state is separable.

If instead of a general bipartite CV state, we consider the special case of a bipartite gaussian state, it has been shown that, using the “standard form” of the CM for this state (here we refer the reader to [183] for more details), the Duan Criteria becomes much stronger as a necessary and sufficient condition for inseparability.

### B.4.2

#### Logarithmic Negativity

The logarithmic negativity (LN) is an entanglement monotone that quantifies the degree of violation of the positive partial transpose (PPT) criterion [241, 246]. Although it is not technically an entanglement measure (e.g., a quantum state with null LN does not impose its separability), it is of special interest to us as it is easily computable for gaussian states and it increases monotonically with entanglement in the system.

For a bipartite gaussian state  $\rho$  with associated covariance matrix  $V$  of the form

$$V = \begin{bmatrix} A & C \\ C^T & B \end{bmatrix}, \quad (\text{B-23})$$

where  $A$ ,  $B$ ,  $C$  are  $2 \times 2$  matrices, the LN becomes a function of the smallest of the symplectic eigenvalues  $\tilde{\nu}_-$  of the partially transposed CM  $\tilde{V} = (\mathbb{1} \otimes \sigma_z)V(\mathbb{1} \otimes \sigma_z)$  given by [247]

$$\tilde{\nu}_- = \sqrt{\sigma/2 - \sqrt{\sigma^2 - 4\det(V)}/2}, \quad (\text{B-24})$$

where  $\sigma = \det(A) + \det(B) - 2\det(C)$ ,  $\mathbb{1}$  is the  $2 \times 2$  identity matrix and  $\sigma_z = \text{diag}(1, -1)$  is a Pauli matrix. Finally, the LN is given by:

$$\mathcal{E}_N = \max[0, -\log(\tilde{\nu}_-)] . \quad (\text{B-25})$$

For the case of a  $M$ -mode gaussian state, we can easily quantify the entanglement between the  $j$ -th and  $k$ -th modes, denoted here as  $\mathcal{E}_N^{j,k}$ , following the prescription of [34]. First, we extract the  $4 \times 4$  matrix  $V^{jk}$  from the total system CM by taking its block diagonal matrix relative only to the modes  $j$ -th and  $k$ -th, associated with the reduced density matrix for this bipartition [34]. Afterwards, we can immediately follow the procedure above to calculate the LN for such bipartition.

## C

### Numerical Toolbox

An ongoing side project of this Masters has been developing an comprehensive numerical toolbox to simulate quantum optomechanical systems. The need for such tools came once we started working on Ref. [157], simulating the closed dynamics of the “mirror-in-the-middle” setup. The code back then relied on the user to have previously made almost all calculations and needed a lot of coding to work. When we started studying Quantum Langevin Equations for [52], it was clear that we needed a much more robust code.

Thus, the whole package was rewritten and the version 1.0 of the Quantum Open Dynamics and Gaussian Information Toolbox was born. This version is much more comprehensive, covering both open and quantum dynamics of optomechanical systems, and calculating a series of Gaussian Quantum Information tools whilst relying solely on the user providing a few parameters.

#### Installation

Clone the GitHub repository or download this Toolbox from File Exchange and add its main folder to the MATLAB path:

```
1 addpath(' <download-path>/<name-folder>');
```

#### Simulating the Quantum Open Dynamics

The Toolbox simulates the system discussed in Chapter 5, comprised of  $N$  mechanical modes, initially in a thermal state, interacting with a single optical mode, initially in the vacuum state, through a linear Hamiltonian. As these initial states have zero mean, we only simulate their covariance matrices' time evolution through a Lyapunov Equation. A semi-classical simulation of the mean quadratures can optionally be carried out through a Monte-Carlo simulation of the Langevin equations for the expectation values of the quadratures [40].

The program only inputs are the time interval for the calculation and the following parameters values:



1. Array with mechanical frequencies for each particle;
2. Array with coupling strength between each particle and cavity field;
3. Array with damping amplitude for each particle;
4. Array with initial temperature for each particle;
5. Array with environmental temperature for each particle;
6. Cavity-tweezer detuning;
7. Cavity linewidth.

An example of these inputs parameters is shown below:

```

1 omega = 2*pi*[305.4; 305.4; 305.4]*1e+3;% Particle's freqs.      [Hz]
2
3 g      = 2*pi*[64.0; 93.2; 109.2]*1e+3;  % Coupling strengths    [Hz]
4
5 gamma = 2*pi*[9.57; 9.57; 9.57]*1e-4;   % Damping amplitudes      [Hz]
6
7 T      = [4.6; 4.6; 4.6]*1e-6;           % Initial temperatures    [K]
8
9 T_env  = [300; 300; 300];                % Environment temperatures [K]
10
11 Delta = 2*pi*315e+3;                    % Tweezer-cavity detuning [Hz]
12 kappa = 2*pi*193e+3;                    % Cavity linewidth        [Hz]
13
14 t = linspace(0, 4.2e-6, 1e+3);          % Simulation's timestamps [s]

```

The user now needs to create an instance of a simulation by calling the “simulation” class constructor. The program infers the number of particles from the lengths of the input arrays, for this example: 3 particles.

```

1 example = simulation(omega, g, gamma, T, T_env, Delta, kappa);

```

Finally, the user runs every calculation available:

```

1 example.run(t);      % Run every calculation available

```

The user can also choose to calculate only what suits them, by passing extra optional parameters to the method ‘run’:

Optional parameter	Corresponding calculation
"langevin"	Solves semiclassical Langevin equations for the expectation value of the quadratures
"lyapunov"	Solve Lyapunov equation for the covariance matrix
"steady_state"	Finds steady state covariance matrix
"occupation_number"	Finds the occupation number for each mode
"entanglement"	Calculates the logarithmic negativity for each bipartition
"entropy"	Calculates the von Neumann entropy for each mode, bipartition and the whole system bipartition
"mutual_information"	Calculates the mutual information for the whole system
"fidelity_test"	Approximates each mode's state by a thermal state through Quantum Fidelity, finding the best matching temperature

As an example, let's imagine the user only wants to calculate the time evolution of the occupation number and entropy of each mode

```
1 example.run(t, "occupation_number", "entropy");
```

The simulation results can be plotted using its internal plotting methods:

```
1 example.plot(); % Plot the results
```

Or directly retrieved from the "simulation", as it is a handle class:

```
1 total_entropy = example.Entropy_system;
```

The closed quantum dynamics can be readily simulated by setting the cavity linewidth and damping amplitudes to zero.

## Gaussian Quantum Information Tools

Alternatively, the user may already have pre-calculated a given gaussian state's mean values and covariance matrix and only want to calculate some property of their state. Thus, we move to the second portion of the Toolbox, which calculates: symplectic eigenvalues, wigner functions, quantum fidelity, mutual information, von Neumann entropy, logarithmic negativity and partial trace over given gaussian states.

Given a multimode gaussian state's covariance matrix, the user can calculate: its symplectic eigenvalues, von Neumann Entropy and mutual information. These are respectively calculated through the following scripts

1. `symplectic_eigenvalues.m` – Calculates the symplectic eigenvalues of a covariance matrix
2. `von_Neumann_Entropy.m` – Calculates the von Neumann entropy of a multipartite gaussian state from its covariance matrix
3. `mutual_information.m` – Calculates the mutual information of a multipartite gaussian state from its covariance matrix

Moreover, the user can also perform a partial trace over a multimode gaussian state's CM in order to find a single mode's or bipartition's CM through

1. `single_mode_CM.m` – Finds the covariance submatrix for a single mode from the full covariance matrix. The user needs to pass a second argument, the index of the mode to be studied.
2. `bipartite_CM.m` – Finds the covariance submatrix for a bipartition from the full covariance matrix. The user needs to pass two more argument, the indexes of the modes of the bipartition.

For a bipartite gaussian state, the user can calculate the logarithmic negativity from its covariance matrix through the script '`logarithmic_negativity2.m`'.

Given a gaussian state's mean value, CM and point on the phase-space, the script '`wigner.m`' calculates its wigner function.

Finally, the script '`fidelity.m`' calculates the fidelity between the two arbitrary gaussian states from the mean value of their quadratures and covariance matrices.